Structural and mechanical properties of dried colloidal silica layers

Arnaud Lesaine

▶ **To cite this version:**

Arnaud Lesaine. Structural and mechanical properties of dried colloidal silica layers. Mechanics of materials [physics.class-ph]. Université Paris-Saclay, 2018. English. NNT : . tel-02095393v1

HAL Id: tel-02095393

https://hal.science/tel-02095393v1

Submitted on 10 Apr 2019 (v1), last revised 8 Nov 2019 (v2)

HAL is a multi-disciplinary open access archive for the deposit and dissemination of scientific research documents, whether they are published or not. The documents may come from teaching and research institutions in France or abroad, or from public or private research centers.

L'archive ouverte pluridisciplinaire **HAL**, est destinée au dépôt et à la diffusion de documents scientifiques de niveau recherche, publiés ou non, émanant des établissements d'enseignement et de recherche français ou étrangers, des laboratoires publics ou privés.

NNT : 2018SACL5597

Thèse de doctorat

Structural and mechanical properties of dried colloidal silica layers

Thèse de doctorat de l'Université Paris-Saclay
préparée à l'Université Paris-Sud

Ecole doctorale n°579 Sciences Mécaniques et Énergétiques, Matériaux et Géosiences (SMEMaG)
Spécialité de doctorat : Mécanique des matériaux

Thèse présentée et soutenue à Orsay, le 12 décembre 2018, par

M. ARNAUD LESAINE HOANG

Composition du Jury :

M. Djimédo KONDO Professeur, Université Pierre et Marie Curie	Rapporteur, Président
M. Alexander ROUTH Professeur, Université de Cambridge	Rapporteur
M. Fabrice CÉLARIÉ Maitre de conférences, Université de Rennes	Examinateur
Mme Véronique LAZARUS Professeur, ENSTA ParisTech	Directrice de thèse
Mme Cindy ROUNTREE Chargée de recherches, CEA Saclay	Co-directrice de thèse

UNIVERSITÉ PARIS-SACLAY

DOCTORAL THESIS

Structural and mechanical properties of dried colloidal silica layers

---

Author:
Arnaud Lesaine Hoang

Advisors:
Véronique Lazarus
Cindy L. Rountree
Daniel Bonamy
Georges Gauthier

Laboratoire FAST, Université Paris-Sud
Laboratoire SPHYNX, SPEC, CEA

Résumé

Le séchage d'une suspension colloïdale produit une couche solide plus ou moins poreuse. Ce processus intervient dans de nombreuses applications, telles que le procédé sol-gel ou la fabrication de laques et de peintures. Durant le séchage, l'évaporation du solvant entraîne la rétraction du matériau ; des contraintes importantes peuvent alors apparaître dans les couches colloïdales, les rendant susceptibles de se fracturer. Il est ainsi crucial de comprendre l'influence de paramètres de contrôle tels que la vitesse de séchage, l'épaisseur de la couche ou la taille de particule sur les propriétés mécaniques et de structure du matériau final. Dans cette thèse, nous avons utilisé des suspensions de Ludox (silice colloïdale) comme système modèle afin d'étudier l'effet de la vitesse de séchage sur les propriétés du matériau solide obtenu.

Dans une première partie, nous avons mis en œuvre des mesures de porosité, ainsi que de microscopie à force atomique et de diffraction de rayons X, afin de caractériser l'effet de la vitesse de séchage sur les propriétés de structure des couches sèches. Nous avons mis en évidence l'importance de la polydispersité des suspensions initiales, ainsi que des phénomènes d'agrégation de particules, sur la structure et la compacité du matériau obtenu.

Dans une deuxième partie, des mesures de constantes élastiques par propagation d'ultrasons nous ont permis de déterminer l'élasticité tensorielle (i.e. le module de compressibilité et celui de cisaillement) des couches colloïdales. Ces modules élastiques dépendent de la porosité du matériau ainsi que de la taille des particules de silice. Les données expérimentales ont été comparées aux prédictions de deux schémas d'homogénéisation (Mori-Tanaka et auto-cohérent), ainsi qu'au modèle de Kendall pour le module d'Young, qui prend en considération une énergie d'adhésion entre les particules.

Enfin, nous avons déterminé la résistance à la fracture des couches colloïdales à l'aide de tests d'indentation Vickers. Cette résistance à la fracture, mesurée à la fin du séchage, est mise en relation avec la vitesse d'évaporation, la porosité du matériau, ainsi que la densité de fractures observées pendant le processus d'évaporation du solvant.

Remerciements

Mes remerciements s'adressent tout d'abord à ma directrice de thèse, Véronique, pour son soutien et sa supervision tout au long de ces trois années de thèse. Elle m'a guidé et conseillé tout en me laissant beaucoup d'autonomie et de liberté dans la réalisation de ce projet. Je souhaite aussi remercier mes trois co-encadrants : Cindy, pour son encadrement quotidien, son aide dans la préparation de mes présentations orales, sa relecture minutieuse de chacune des versions successives de mon manuscrit ; Daniel, pour m'avoir fait participer à sa démarche expérimentale, qui associe une ingéniosité foisonnante avec un optimisme hardi ; et Georges, pour son regard critique et toujours objectif sur mes résultats. Merci à vous quatre pour nos longues conversations scientifiques et vos apports complémentaires à mon travail de thèse.

Je souhaite également remercier les membres de mon jury de thèse, pour avoir accepté d'assister à ma soutenance, et notamment Djimédo Kondo et Alexander Routh, qui ont consacré du temps à rapporter mon manuscrit. J'exprime également mes remerciements à Marianne Impéror, pour son accueil au LPS et pour son accompagnement dans la réalisation et le dépouillement des mesures SAXS, ainsi qu'à Fabrice Célarié, qui m'a accueilli à Rennes pour y réaliser des tests d'indentation Vickers. En consacrant du temps à me former à ces techniques expérimentales, ils ont apporté une contribution importante aux résultats présentés dans ce manuscrit.

Ma thèse s'est réalisée entre le SPEC et le FAST, et je remercie leurs directeurs, François Daviaud et Marc Rabaud, de m'avoir accueilli au sein de leurs laboratoires respectifs, ainsi que leurs secrétaires, Mai Guerrib, Monique Saint-Rose et Nathalie Royer, pour leur grande patience à mon égard.

Je remercie tous les membres du SPHYNX et du FAST, qui ont partagé mon quotidien pendant trois ans : Alizée et Simon (mes deux camarades de thèse, le yin et le yang), Kakoli et Thomas S. (pour avoir partagé mon bureau – dans des styles assez différents), Hugues F., Paul D. et Paul D., Benoît, Vincent B., Michel B., Mario, Houria, Damien, Jean-Baptiste, Denis, Samuel, Kanna, Benjamin, Valentina, Iaroslav, Vishwanath, Stefan, Thomas H., Vincent P. et Cécile (pour leur aide sur le montage expérimental), Roland, Hervé, Basile, Bérengère, Vadim, Caroline, François L. (pour nos conversations métaphysiques), Sébastien, Marco, Gilbert, Ivan, Saco, Thuy, Hughes C., Cesare, Éric, Antoine et Lamine (pour leur accompagnement au cours de

mon monitorat), et Marguerite (pour nos conversations sur la silice colloïdale). Un grand merci à Johann pour le stage qu'il a réalisé sous ma supervision.

Je souhaite enfin exprimer ma gratitude à tous les membres de ma famille : ils m'ont soutenu et accompagné tout au long d'études dont cette thèse représente l'aboutissement. Merci à Dominique et Gérard, Diep et Nicole, Philippe, Clémence et Françoise.

Summary

Introduction

Colloidal suspensions (also called colloidal sols or colloidal dispersions) are suspensions of small particles in a continuous liquid phase. When the particles are of the order of a micrometer in size or smaller, Brownian agitation stabilizes the suspension by preventing sedimentation of the particles. Colloidal suspensions are commonly found in biological and geological systems such as blood and clay. Many industrial applications also involve colloids: paints and lacquers to photonic crystals and artificial opals (Hunter, 1989; Dutta and Hofmann, 2004). In sol-gel processes, for example, the gelation and drying of colloidal suspensions allow the preparation of ceramics and glasses with tunable properties (Brinker and Scherer, 1990).

When a colloidal suspension dries, the removal of the liquid phase leads to the formation of a solid layer. If the colloidal particles are soft, they may deform during the drying process, and the resulting layer can be continuous and crack-free. This is for example the case for certain latex suspensions (Routh and Russel, 2001). Conversely, colloidal suspensions with harder, less deformable particles tend to yield porous layers, which crack during the desiccation process (Goehring et al., 2015). A major challenge is then to predict and control the crack morphology and density. For example, thin films can be prepared by pouring, dipping or spraying a colloidal suspension on a substrate. These films frequently have cracks; yet, many of the corresponding applications (such as protective paints, photographic film and paper coatings) require crack-free films. When fracture occurs, the crack patterns may shed light on the conditions under which the colloidal layer dried; thus, the cracking and peeling displayed by paintings can help ascertain their authenticity (Giorgiutti-Dauphiné and Pauchard, 2016). Finally, drying colloidal suspensions may serve to model analogous systems such as cooling materials in which shrinkage cracks appear.

Unidirectional drying experiments in capillary tubes (Allain and Limat, 1995; Gauthier et al., 2007) showed the crack density to depend on a balance between the elastic and fracture energy in the system. This balance was described by a dimensionless parameter involving both the mechanical loading and the material properties (elastic moduli and fracture toughness) at the apparition of the cracks (Gauthier et al., 2010; Maurini et al., 2013). A previous PhD work (Chekchaki, 2011) used beam

deflection measurements (Chekchaki et al., 2011) to relate the loading in drying colloidal layers to the evaporation rate; the experimental data was in agreement with a poroelastic model (Chekchaki and Lazarus, 2013).

In this work, I consider the second point; namely, the material properties. We focus on colloidal silica and explore the structural, elastic and fracture properties of dry colloidal silica layers, using the evaporation rate as a control parameter. Four different silica suspensions, with particle radius ranging from 5.5 nm to 14 nm, are used. Colloidal silica is a good model for a *hard* colloid: as the particles are very rigid, they only weakly deform during the drying process. The resulting dry layer is a packing of spherical particles, with little sintering or diffusion of solid material.

The manuscript is structured as follows:

- The first chapter gives an overview of the current knowledge on colloidal suspensions. I first review literature concerning colloidal chemistry, such as the DLVO theory of colloidal stability, and I discuss the preparation and stability of colloidal silica sols. The second section discusses the general process of colloidal drying, as well as the phenomena of solvent evaporation, particle convection and particle sintering. Finally, the last section reviews the mechanics of drying colloidal layers to explain how cracks arise during desiccation.

- The second chapter presents the experimental protocol that I used during my thesis. Four different silica suspensions are used. Concerning these suspensions SAXS measurements yield, for each suspension, the median particle size and the dispersity. I then present the experimental setup used to prepare the dry colloidal layers, and I discuss the evolution of mass and layer aspect during the drying process. Finally, SAXS measurements on the dry layers reveal their evolution over long timescales.

- The third chapter concerns the structural properties of the dry colloidal layers; it is an extension of a previous study (Piroird et al., 2016) in which I participated. This previous study, only carried out on one of the suspensions, evidenced a counter-intuitive evolution of the structure of the layers with the evaporation rate: faster evaporation yielded more ordered layers. In this chapter, I repeat the study on each of the other three suspensions, using AFM microscopy and hydrostatic weighting to probe the surface and volume ordering of the layers. Additionally, SAXS measurements on a suspension subjected to a holding period confirm the importance of aggregation processes on the structure of the resulting dry layers: faster drying reduces aggregation, and thus favors denser and more ordered packing.

- The fourth chapter concerns the elastic properties of the dried colloidal layers. Its main text reproduces an article published in *Soft Matter* in 2018, of which I am the first author (Lesaine et al., 2018). Ultrasound velocity measurements provide both the bulk and shear moduli of the porous materials. The experimental data is then compared and contrasted with the predictions of several models for the elasticity of porous media: homogenization schemes (Mori-Tanaka and self-consistent) based on continuum mechanics and asymptotic analysis, and Kendall's model for the elasticity of particle packings with surface adhesion. The study published in *Soft Matter* was carried out using dry layers prepared from a single suspension. Thus, an addendum to the chapter presents the elastic moduli measured on layers prepared from the three other suspensions.

- The fifth chapter concerns fracture properties of the colloidal layers, during the desiccation process as well as in the final dry state. The first part reviews the evolution of the layers' aspect during the drying process, as well as the crack patterns obtained for the different suspensions and the different drying rates. The processing of crack images and the analysis of mass curves allows quantifying the influence of particle size and evaporation rate on crack formation during the solvent evaporation: more cracks appear in faster-dried layers. In addition, indentation measurements yield the Vickers hardness and fracture toughness of the dry layers in their final state. In order to explain the influence of evaporation rate on the crack patterns and the fracture resistance of the dry layers, I show that two timescales need to be compared: one associated to the evaporation process and the build-up of stresses, and the other associated to the chemical consolidation processes, *i.e.* the formation of bonds between the particles.

Chapter 1

A review of colloidal suspensions

Colloidal suspensions (also called colloidal dispersions) are suspensions of small particles in a liquid phase. The dispersed phase which constitutes the particles is sometimes also liquid, as in the case of milk, but most colloidal suspensions concern solid particles.

This chapter reviews the properties of colloidal suspensions which will be of interest in this thesis. The first part discusses colloidal chemistry and stability with an emphasis on colloidal silica, which will be used as a model system in this work. The second section presents the process of colloidal drying and describes the evolution of the structure of a drying suspension. Different drying geometries (vertical vs. lateral and uniform vs. directional) are also discussed. Finally, the last section reviews the basics of poroelasticity theory to explain how stresses arise in drying colloidal films and lead to crack formation.

I The chemistry of colloidal suspensions

1 Colloidal stability

The first surprising property of colloidal suspensions is their stability. As the density of the solid particles generally differs from that of the liquid phase, the particles could be expected to sediment (in the case of denser particles) or float up (in the case of lighter particles), leading to phase separation in the suspension.

However, when the dispersed particles are small enough, forces such as gravity or buoyancy become negligible compared to the Brownian agitation, which acts to diffuse the particles and make the suspension homogeneous. This mechanism for the stability of colloidal suspensions puts an upper limit on the size of the colloidal particles: particles should not be larger than a few micrometers in order to avoid sedimentation.

Nevertheless, colloidal suspensions have a tendency to destabilize through a process known as aggregation. When colloidal particles interact attractively, they stick to each other, forming progressively larger aggregates. The aggregates then grow until they reach a critical size and sediment. Thus, the stability of a colloidal suspension requires repulsive interactions between the particles. This section outlines the different interactions relevant to colloidal stability.

1.1 Van der Waals interaction

Van der Waals forces are attractive and arise from induced electrostatic dipole interactions. An atom or molecule, through quantum fluctuations, acquires an instantaneous dipole moment $\overrightarrow{p_1}$, which in turn creates an electric field $\overrightarrow{\mathrm{E}}$. This field induces, in a second atom or molecule, a dipole moment $\overrightarrow{p_2} = \alpha\,\overrightarrow{\mathrm{E}}$. The resulting interaction energy, $\mathrm{U}_{\mathrm{V}d\mathrm{W}} = -\overrightarrow{p_2}.\overrightarrow{\mathrm{E}} = -\alpha\mathrm{E}^2$, is attractive. Since the electric field induced by a dipole scales as $1/r^3$ (with r the distance to the dipole), the interaction energy scales as $1/r^6$; thus, van der Waals forces are short-ranged.

In order to estimate the attractive forces between two bodies with a large number of atoms, Hamaker (Hamaker, 1937) and de Boer (de Boer, 1936) have proposed a model with two assumptions:

- Interactions are non-retarded, that is, the propagation delay of the electric field between two dipoles is much smaller than the characteristic time for dipole fluctuations. In practice, this condition is verified when the dipole separation does not exceeds a few tens of nanometers.

- Interactions are additive, that is, the dipole - dipole interactions can be summed over the two bodies in order to get the total interaction.

Hamaker and de Boer's model then expresses the van der Waals interaction as a function of the geometry and size of the bodies, their distance, and the Hamaker constant A, which has the dimensions of an energy and only depends on the nature of the bodies and on the separating medium. For two spheres of equal radius r and surface to surface separation d (*i.e.* center-to-center separation $2r + d$) the interaction potential is

$$\mathrm{U}_{v d\mathrm{W}} = -\frac{\mathrm{A}a}{12d} \tag{1.1}$$

1.2 Electrostatic interaction

Electrostatic interactions also play a role in the stability of colloidal suspensions (Fennell Evans and Wennerstrom, 1994; Israelachvili, 2011). Colloidal particles in water can acquire surface charge through two mechanisms:

- Molecular groups at the surface of the particles can dissociate into charged species.
- Ions present in the liquid phase can be adsorbed at the surface of the particles or attached to dissociated groups created through the first mechanism (a process known as ion exchange).

Since the dissociation reactions for the surface group often involve H^+ or OH^- ions, the pH of the solution generally has a strong influence on the surface charge of the particles. The pH at which surface charge is neutral is referred to as the isoelectric point.

The surface charge carried by the particle modifies the composition of the liquid phase in its vicinity. Some counter-ions (*i.e.* ions carrying a charge opposite to the surface one) attach to the surface, forming the Stern layer, which is a few angstroms thick. Additional counter-ions are attracted, but remain in solution in the vicinity of the surface, forming a diffuse layer. A plane, coined the Outer Helmholtz Plane (OHP), separates these two layers.

In the diffuse layers, the ions in the solution (whether pre-existent or arising from surface groups dissociation) obey the Boltzmann statistic. The concentration, ρ_i, of a given ion species i is:

$$\rho_i = \rho_{0,i} \exp(\frac{-z_i e \Psi}{k\mathrm{T}}) \tag{1.2}$$

where z_i the ion valence, e the elementary charge, Ψ the electrical potential inside the solution and $\rho_{0,i}$ the reference concentration (concentration at zero potential). Moreover, the potential, Ψ, can be related to the ion concentrations through Poisson's equation:

$$\nabla^2 \Psi = -\frac{e}{\varepsilon \varepsilon_0} \Sigma_i z_i \rho_i \tag{1.3}$$

where $\varepsilon = 80$ is the relative permittivity of water.

Combining eq. 1.2 and 1.3 gives the Poisson-Boltzmann equation. Solving this equation provides an expression for the ion concentration as a function of the potential at the outer Helmholtz plane (Ψ_{OHP}). Ψ_{OHP} is related to the surface charge density of the particles through Grahame's equation. In general, these equations

cannot be solved numerically; however, when $\Psi \ll k\mathrm{T}/e$, eq. 1.2 can be estimated to be linear and

$$\Psi = \Psi_{\mathrm{OHP}} \exp(-\kappa r) \quad \text{with} \quad \kappa^2 = \frac{\Sigma_i \rho_{0,i} z_i^2 e^2}{\varepsilon \varepsilon_0 k\mathrm{T}} \tag{1.4}$$

The parameter $\frac{1}{\kappa}$, called the Debye length, is the characteristic length for screening of the electrostatic interactions. These interactions are stronger when Ψ_{OHP} is higher and κ lower; in other words, for colloids with high surface charge in a solution with low ion concentration.

1.3 The DLVO theory

The DLVO theory (Derjaguin and Landau, 1941; Verwey and Overbeek, 1949) conjunctures colloidal stability as a competition between van der Waals and electrostatic forces:

$$\mathrm{U}_{\mathrm{DLVO}} = \mathrm{U}_{vd\mathrm{W}} + \mathrm{U}_{elec} \tag{1.5}$$

The behavior of the colloidal suspension depends on the relative strength of these two interactions. At short distances, the attractive van der Waals interaction dominates. At long distances, $\mathrm{U}_{vd\mathrm{W}} \propto -1/r^6$ and $\mathrm{U}_{elec} \propto \exp(-\kappa r)$, so the overall interaction remains attractive. In the intermediate range, electrostatic forces may dominate, creating a repulsive barrier which prevents particle aggregation and ensures the suspension stability.

The DLVO theory notably explains the influence of salt concentration on the stability of colloidal suspensions. As ion concentration increases in the liquid phase, the Debye length decreases, shortening the range of the repulsive interactions between particles. This results in a decrease of the repulsive maximum, and ultimately in the destabilization of the suspension, as the particle interaction becomes attractive at all distances. The deposition of mud in river deltas exemplifies this phenomenon: as the river reaches the sea, the increased salt concentration precipitates the submicron particles carried by the water.

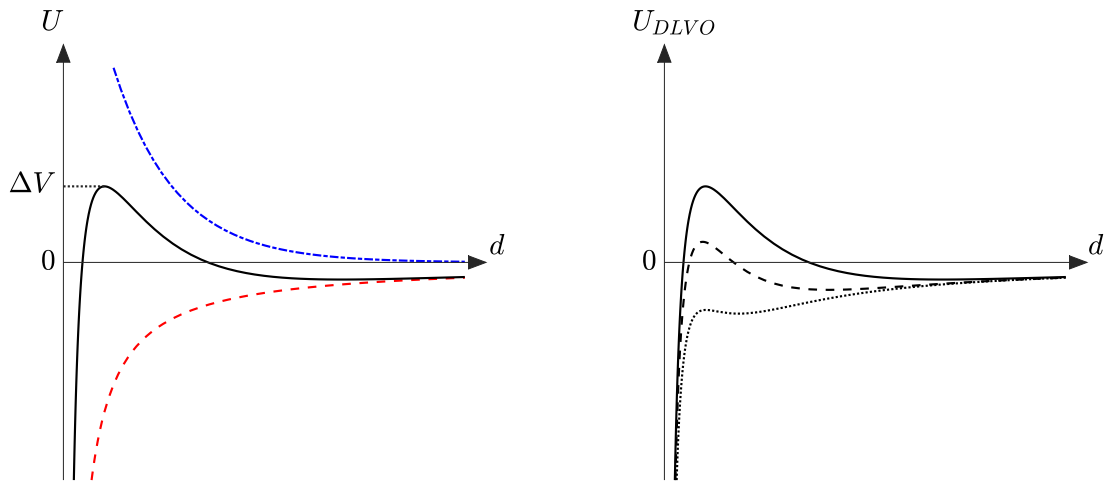

FIGURE 1.1: Left: The DLVO interaction potential (black solid line) between two particles with separation d is the sum of the attractive van der Waals potential (red dashed line) and a repulsive electrostatic contribution (blue dash-dot line). Under appropriate conditions, the total interaction is repulsive at intermediate distances, with a potential barrier ΔV ensuring the stability of the solution. Right: Influence of salt concentration on suspension stability. At low salt concentrations, the long-ranged electrostatic interactions ensure a high potential barrier (solid line). Adding salt shortens the range of these interactions and lowers the height of the barrier (dashed line). At high salt concentrations, the DLVO potential becomes attractive at all distances (dotted line). Thus, particles form aggregates and the suspension loses its stability.

2 The case of silica

The work presented in this manuscript concerns the properties of layers obtained by drying colloidal silica suspensions. These properties can be expected to depend on the stability and aggregation behavior specific to these suspensions. The following section thus presents relevant results on colloidal silica and on the chemistry of silica in water.

2.1 The preparation of colloidal silica

Silica is an amorphous material, of chemical formula SiO_2, *i.e.* silicon dioxide. At the atomic scale, each silicon atom is linked to four neighboring oxygen atoms through siloxane bonds -Si-O-Si-.

Nanometric or micrometric silica particles can be prepared in a variety of ways (Iler, 1979). Some methods involve the condensation of particles from a high temperature gas phase; thus pyrogenic silica is obtained from the combustion of volatile silicon compounds, whereas fumed silica results from the oxidation of silicon oxide SiO into silicon dioxide SiO_2. However, these vapor-phase methods tend to produce hydrophobic particles which need to be redispersed in a liquid phase to obtain a colloidal sol (Loftman and Thereault, 1957). Thus, colloidal silica suspensions are generally prepared by the precipitation of silica particles from water-soluble precursors.

Two methods permit the preparation of colloidal silica by precipitation:

- Silica particles can be precipitated from water-soluble sodium or potassium silicate. Silicates are obtained from the reaction of quartz (*i.e.* crystalline silica) with sodium or potassium carbonate, as follows (for the sodium salt):

$$3\,SiO_2 + Na_2CO_3 \longrightarrow CO_2 + 3\,Na_2SiO_3 \tag{1.6}$$

  The silicate solution is then transformed into monosilicic acid $Si(OH)_4$ (also named soluble silica) through acidification with a mineral acid or by ion exchange. At concentrations higher than 20 mmol, monosilicic acid immediately polymerizes and forms polysilicic acid through a condensation reaction.

- In the Stöber process, the hydrolysis of organic silicon compounds provide the source of silica for particle growth (Stöber et al., 1968). This process tends to produce particles with high internal porosity, in contrast with the particles produced through the silicate process, which are very compact.

Precipitation of colloidal silica generally proceeds in two stages. The *nucleation* stage produces polysilicic acid, a polymer of monosilicic acid structured as loose chains or dense solid particles. When containing less than 100000 $Si(OH)_4$ units (corresponding to particles with diameter smaller than 5 nm), polysilicic acid is unstable. Thus, a second stage (the *growth* stage) takes place, in which the mean particle size increases. Growth happens either through Ostwald ripening (*i.e.* transfer of silica from smaller to larger particles, through dissolution as $Si(OH)_4$ followed by redeposition) or through particle aggregation. Figure 1.2 represents the successive stages in the precipitation of a colloidal silica suspension (Iler, 1979).

Finally, suspension washing procedures along with evaporation, centrifugation or ultrafiltration techniques allows adjusting the silica and counter-ion concentrations to obtain stable suspensions containing $15 - 60\%$ silica by mass. The higher

surface area of small particles make them more soluble; thus, suspensions of small particles are harder to stabilize at high concentrations (Alexander, 1954).

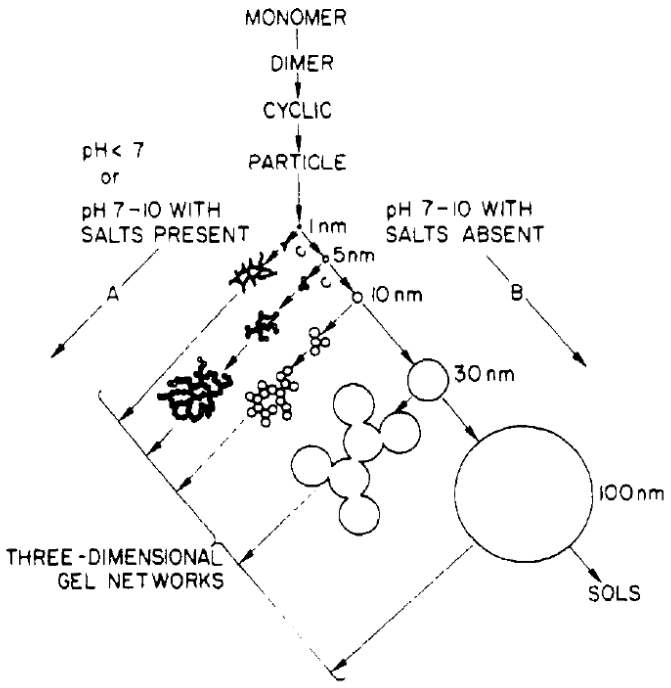

FIGURE 1.2: Polymerization behavior of silica (figure taken from Iler, 1979). Starting from $Si(OH)_4$ monomer, the nucleation process yields nanometer-sized particles. These particles can either aggregate to form a solid gel network (A) or, under appropriate pH and salt concentration conditions, grow in size through ripening (B) to form a stable sol (colloidal suspension).

2.2 The chemistry of silica in water

When silica is in contact with water, siloxane bonds at the surface of the material are converted to silanol groups through an hydrolysis reaction:

$$\equiv Si - O - Si \equiv + \ H_2O \longrightarrow 2 \equiv Si - OH \tag{1.7}$$

A silanol group can either adsorb a proton, following

$$\equiv Si - OH + \ H^+ \longrightarrow \ \equiv Si - OH_2^+ \tag{1.8}$$

or release a proton, following

$$\equiv SiOH \longrightarrow \ \equiv SIO^- + \ H^+ \tag{1.9}$$

The extent of these reactions, and thus the surface charge of silica, depends on the pH of the suspensions. The isoelectric point of silica is $p\mathrm{I} \simeq 2$; for $p\mathrm{H} > 2$, the second reaction is predominant. Thus, the surface of untreated silica particles in water generally carries a negative charge, except under very acidic conditions.

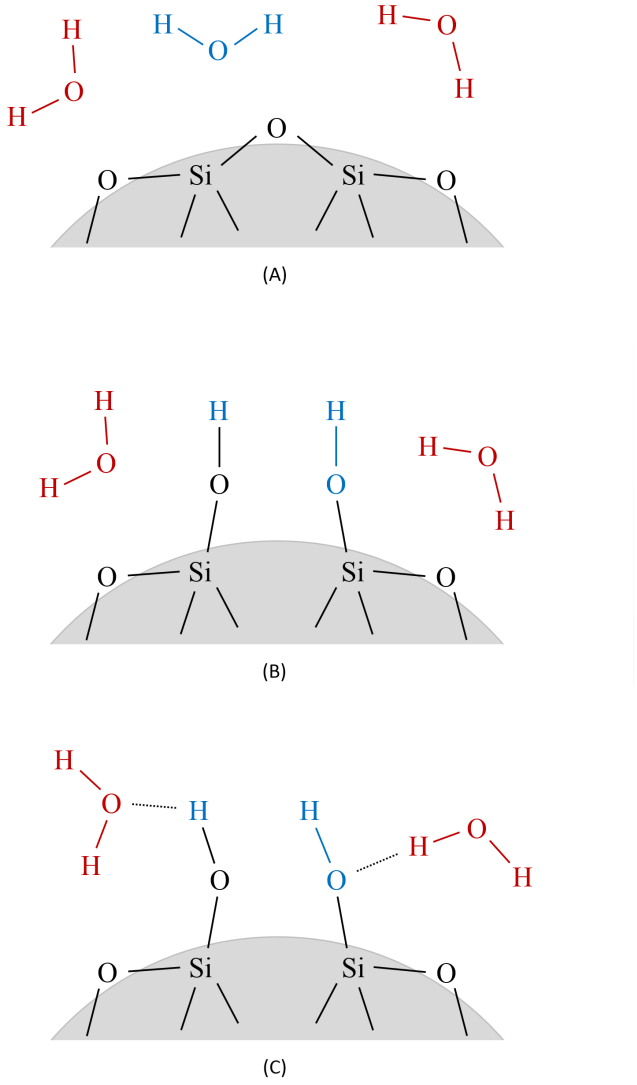

FIGURE 1.3: Schematic of water absorption at the surface of silica. (A) Dehydroxylated silica surface in water. (B) Chemical water absorption: a siloxane bond (Si-O-Si) is broken and transformed in two silanol groups (SiOH) through the absorption of a water molecule (in blue). (C) Physical water absorption: additional water molecules (in red) attach to pre-existing silanol groups through the formation of hydrogen bonds (dotted lines).

The density of silanol groups at the surface is $4 - 8\,\mathrm{nm}^{-2}$ (Zhuravlev, 1993). As silica is very hydrophilic, water easily attaches to its surface, not only through

silanol groups formation but also through hydrogen bonding with pre-existing silanol groups. These two mechanisms for water adsorption are respectively referred to as chemical and physical adsorption (see fig. 1.3). Evaporating water off the surface of silica requires a heat treatment. Drying silica between 100 and 200° C eliminates all physically adsorbed water, whereas removal of chemically absorbed water (a process coined dehydroxylation) gradually happens when heating silica between 150 and 1000° C (Zhuravlev, 2000; Peng et al., 2009).

2.3 The stability of colloidal silica

Experiments on colloidal silica suspensions reveal their unexpected stability (Allen and Matijevic, 1969; Allen and Matijevic, 1970). Under appropriate pH conditions, close to the isoelectric point, they can be stable even in saturated salt solutions. Conversely, increasing the pH of the suspensions decreases their stability, despite the increase in surface charge.

This stability behavior is explained by the presence of silanol ($\equiv$ SiOH) groups at the surface of the particles (Vigil et al., 1994). These groups 'stick out' of the surface, extending out the outer Helmholtz plane, and making the DLVO potential U_{DLVO} repulsive at all distances. Thus, van der Waals forces play an insignificant role in the behavior of colloidal silica suspensions. However, another mechanism still permits the aggregation of silica particles: the formation of siloxane bonds (Depasse and Watillon, 1970). In this process, a hydrogen bond first forms between a non-dissociated silanol group ($\equiv Si - OH$) and a dissociated one ($\equiv Si - O^-$). The two groups then undergo a condensation reaction:

$$\equiv Si - OH + {}^-O - Si \equiv \longrightarrow \equiv Si - O - Si \equiv + OH^- \tag{1.10}$$

This aggregation mechanism relies on the presence of dissociated silanol groups. As the equilibrium for the corresponding dissociation reaction (eq. 1.9) is pH dependent, the stability of the silica suspensions also depends on the pH of the solution:

- for $pH < 2$, the concentration of dissociated silanol group is too low to allow aggregation, and the suspension is stable;
- for $2 < pH < 7$, there are more dissociated groups, which allows particle aggregation; thus the silica suspensions are instable in this pH range;
- for $pH > 7$, there are enough dissociated silanol groups to create electrostatic repulsion between the particles, ensuring the stability of the suspension. The limit value $pH \simeq 7$ is dependent on the ion concentration of the suspension,

as adding salt to the suspension decreases the Debye length (Pauchard et al., 1999; Giuseppe et al., 2012).

II How does a colloidal layer dry?

1 General description of the process

Many review works describe the process of colloidal drying (Brinker and Scherer, 1990; Xu et al., 2009; Routh, 2013; Goehring et al., 2015). As a colloidal layers dries, it gradually transitions from a liquid to solid state. This evolution happens through three stages, pictured on fig. 1.4:

- During the first stage (fig. 1.4a), evaporation of the liquid phase increases the concentration of the suspension, bringing the solid particles closer to each other.

- During the second stage, colloidal particles come in contact with each other. This forms a solid, cohesive network. The air - liquid interface contacts the solid particles and menisci appear at the top surface of the layer (fig. 1.4b), in the throats between the particles. According to Laplace's law, the presence of the menisci entails a pressure drop at the interface,

$$\Delta \mathrm{P} = \mathrm{P}_{liq} - \mathrm{P}_{atm} = -\frac{2\gamma \cos\theta}{r} \tag{1.11}$$

  with r the radius of the menisci and γ the surface tension of the liquid. As the desiccation proceeds, the menisci deepen, and an increasing pressure is applied on the solid particle network. The network reacts through particle deformation and consolidation; that is, particles reorganize into a denser packing, making the network more rigid (fig. 1.4c).

- When the pressure differential becomes too large, a meniscus will depin and jump to a neighboring throat, leaving an empty pore behind, a process coined a Haines jump (Haines, 1930). Thus, a close-packed layer of monodisperse particles of radius a can only sustain a maximal capillary pressure

$$\mathrm{P}_{cap,max} \simeq 10\frac{\gamma}{a} \tag{1.12}$$

  with the prefactor estimated to range from 5.3 (see White, 1982 for the corresponding thermodynamical argument) to 13 (from geometrical considerations,

see *e.g.* chap. 6 of Goehring et al., 2015). The consolidation of the particle network increases its yield strength σ_Y. Once $\sigma_Y > P_{cap,max}$, consolidation will stop; the air-liquid interface will depin from the layer surface and recede into the network. This marks the beginning of the third stage of the drying, in which the layer is partially desaturated (fig. 1.4d).

As colloidal suspensions contain very small particles, the corresponding capillary pressure can be very large. For silica particles with radius $r = 5 - 15\,\text{nm}$ in water ($\gamma = 70\,\text{mN/m}$), eq. 1.12 gives $P_{cap,max} \simeq 50 - 150\,\text{MPa}$.

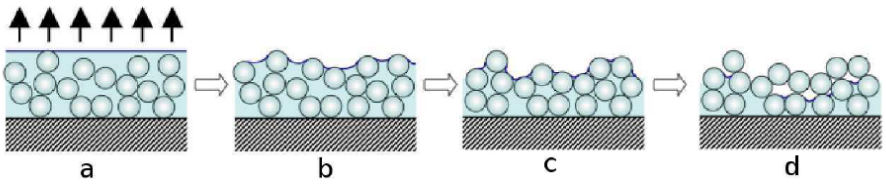

FIGURE 1.4: Stages of colloidal drying. (a) Liquid stage: evaporation reduces the volume of solvent and brings the particles closer to each other. (b-c) Saturated solid stage: particles form a solid network which consolidates under the capillary pressure. (d) Desaturated solid stage: the air-liquid interface recedes into the layer and the pores gradually empty.

2 Solvent evaporation

A crucial parameter to describe a drying process is the evaporation rate of the solvent. It is defined as the volume of solvent evaporated per unit time and unit surface; it has the dimension of a velocity. The evaporation rate depends on the geometry of the drying setup as well as the ambient atmospheric conditions (*e.g.* externally imposed air flows).

As a colloidal layer dries, the evaporation rate gradually decreases, and its evolution with time can be divided in two periods:

- During the first period (Constant Rate Period, CRP), the suspension is dilute enough so that the solid particles do not hinder evaporation. The evaporation rate is thus constant, and very close to the evaporation rate of the pure liquid phase (water) under identical conditions.

- During the second period (Falling Rate Period, FRP) the network of solid particles is dense enough to hinder the liquid flow to the surface, and the evaporation rate decreases.

Finally, the mass of the layer stabilizes and evaporation stops ($\dot{E} = 0$). The evaporation may not be complete, that is, some liquid water may remain trapped in the pores, in an equilibrium that depends on temperature, ambient humidity and pore size.

The transition between the two drying periods, *i.e.* the instant at which the evaporation rate starts dropping, is coined the critical point. It is generally believed to coincide with the end of the network shrinkage and the beginning of the penetration of the air - liquid interface in the porous medium; that is, the transition between the second and the third drying stages, represented on fig. 1.4c and 1.4d (Sherwood, 1929; Toei and Okazaki, 1970; Scherer, 1990). In granular media, the Falling Rate Period can further be divided in two stages. During the first stage, a continuous liquid film at the surface of the particles carries water from saturated pores to the surface of the porous medium, where it evaporates. During the second stage, no liquid film coats the particles; instead, water evaporates inside the pores and diffuses as a gas to the surface. The mechanisms at work during the FRP may be different for packings of nanometer-sized particles, in which a liquid film is conjectured to coat the solid particles at all times (Thiery et al., 2015). Moreover, in some systems (Lazarus and Pauchard, 2011; Chekchaki, 2011), the FRP begins when the first cracks appear, well before the pores begin emptying; in these systems, the decrease in evaporation rate may be due to the formation of menisci, rather than to the desaturation of the layer.

3 Particle convection and drying geometries

As evaporation progresses, molecules of liquid are removed from the interface and need to be replaced. The associated liquid flow convects the solid particles and can cause concentration gradients in the layer. The steepness of these gradients can be quantified from the Péclet Pe number, which compares the advection (t_{adv}) of the colloidal particles with their diffusion (t_{diff}):

$$\mathrm{P}e = \frac{t_{diff}}{t_{adv}} = \frac{h\dot{\mathrm{E}}}{\mathrm{D}} \tag{1.13}$$

$t_{adv} = h/\dot{\mathrm{E}}$ represents the characteristic time for the advection of the solid particles across a length scale h, considering an evaporation rate of the liquid $\dot{\mathrm{E}}$. $t_{diff} = h^2/\mathrm{D}$ is the characteristic time for the diffusion of particles. The diffusion coefficient, D,

can be expressed through the Stokes-Einstein relation,

$$\mathrm{D} = \frac{k\mathrm{T}}{6\pi r\mu} \tag{1.14}$$

where r is the particle radius and μ is the dynamic viscosity of the fluid.

When $\mathrm{P}e \ll 1$, particles diffuse fast enough so that their concentration remains spatially uniform and the layer dries through uniform compaction. In contrast, when $\mathrm{P}e \gg 1$, advection dominates over diffusion and a gradient appears in the drying suspension, with the particles concentrating at the drying edge.

In general, two drying geometries exist: vertical and lateral drying, respectively. Vertical drying is one-dimensional and a good model for the drying of large surfaces of liquid in still air. Far away from the edges of the liquid layer, the flow of liquid towards the evaporation surface is vertical and quantities such as liquid velocity, particle concentration, or pressure, only depend of the considered height. In contrast, lateral drying happens when a non-uniform evaporation rate occurs over the drying surface. This creates lateral liquid flows though the layer. When a colloidal suspension undergoes lateral drying, a drying front will often appear and propagate across the layer, with the three stages outlined above (liquid suspension, solid saturated layer and solid desaturated layer) happening in succession. Lateral drying can for example arise when air is blown laterally over the surface of the liquid layer, or in drying droplets, in which the edge dries faster than the center (Deegan et al., 1997).

4 Particle sintering

Drying a colloidal suspension of soft particles, such as a latex suspension, can yield a continuous film with no porosity, as the particles are able to sinter together and close the gaps between them. When the suspension dries uniformly, three mechanisms may account for the deformation of particles (Routh and Russel, 2001):

- In the wet sintering regime, particles deform as the layer is still saturated. The deformation is driven by the surface energy of the particles in the liquid phase.
- In the capillary deformation regime, particles deform under the capillary pressure as menisci form at the air/liquid interface.
- In the dry sintering regime, particles deform as the layer is desaturated. As for the wet sintering regime, the deformation is driven by the surface energy of the particles (in air).

The extent of wet sintering during the desiccation process can be estimated via a dimensionless ratio λ,

$$\lambda = \frac{a\dot{\mathrm{E}}}{\eta_0 \gamma h} \tag{1.15}$$

with $\dot{\mathrm{E}}$ the evaporation rate of the colloidal layer, h its thickness, a the particle radius, γ the surface energy of the particle (in the liquid phase), and η_0 the viscosity of the particle material. λ can be understood as a ratio of two characteristic times: $\lambda = \frac{t_v}{t_{ev}}$ with $t_{ev} = \frac{h}{\dot{\mathrm{E}}}$ a characteristic evaporation time and $t_v = \frac{\eta_0 a}{\gamma}$ a characteristic time for the viscous deformation of the particles. When $\lambda \ll 1$, wet sintering is predominant; when $\lambda \gg 1$, particles deform through the dry sintering regime or as a result of capillary forces.

In contrast to latex particles, silica is much harder; thus wet sintering can be expected to be negligible in colloidal silica layers. For particles of radius $a = 10\,\mathrm{nm}$ in water ($\gamma \simeq 10\,\mathrm{mJ.m^{-1}}$), and taking $\eta_0 \simeq 10^{17}$ Pa.s for the viscosity of silica at room temperature (Vannoni et al., 2011), the characteristic time for viscous particle deformation is $t_v \simeq 30000$ years, which is much longer than any practical drying experiment. Moreover, the silica particles should undergo little plastic capillary deformation: the maximum capillary pressure (estimated above at $\mathrm{P}_{cap,max} \simeq 50 - 150\,\mathrm{MPa}$) is lower than the compressive yield strength of silica ($\sigma_\mathrm{Y} \simeq 1\,\mathrm{GPa}$) and much lower than its Young's modulus (E = 72 GPa, see chap. 4 for a measurement of this value). Thus, sintering is unlikely to take place during the drying of a colloidal silica layer.

III Mechanics of a drying colloidal layer

In the previous section, the consolidation and fracture of drying colloidal layers were attributed to the stresses generated by the evaporation of the liquid phase. We now present a simple poroelastic model for a colloidal layer in order to gain a more quantitative understanding of the mechanisms leading to desiccation cracks.

1 An introduction to poroelasticity

Poroelasticity theory was developed by Biot (Biot, 1941) to describe the mechanical behavior of an elastic porous solid whose connected pores are filled with a liquid; it is thus applicable to a wide array of systems, from soils and rocks (Wang, 2000) to bones and living cells (Cowin, 1999; Moeendarbary et al., 2013).

Poroelasticity theory models the biphasic system as an equivalent continuous medium, at each point of which two phases are superposed:

- a solid, porous phase which undergoes small, linear elastic deformations, with displacement $\boldsymbol{u}$;
- a liquid phase which saturates the pores and flows with velocity $\boldsymbol{v}$.

1.1 Variables

The state of the equivalent continuous medium can be described using the classical variables of linear elasticity, that is the stress $\boldsymbol{\sigma}$ and the strain $\boldsymbol{\varepsilon}$, defined by

$$\varepsilon_{ij} = \frac{1}{2}(\frac{\partial u_i}{\partial x_j} + \frac{\partial u_j}{\partial x_i}) \tag{1.16}$$

In order to describe the behavior of the liquid phase, two additional variables are introduced: the pressure p and the increment of fluid content ξ, which represents the variation of the volume fraction of liquid (*i.e.* the porosity of the solid skeleton) with respect to a reference state ($\xi = 0$ for a medium with zero stress and zero pressure).

1.2 Constitutive equations

The increment of fluid content ξ is related to the fluid velocity $\boldsymbol{v}$ through a conservation equation:

$$\frac{\partial \xi}{\partial t} = \nabla.\boldsymbol{v} \tag{1.17}$$

and $\boldsymbol{v}$ itself can be expressed from the pressure gradient ∇p through Darcy's law:

$$\boldsymbol{v} = \frac{k}{\eta}\nabla p \tag{1.18}$$

with η the dynamic viscosity of the fluid ($\eta = 10^{-3}$ Pa.s for water at room temperature). The parameter k is called the permeability of the porous medium. For a packing of monodisperse spheres with radius r, k can be, through Kozeny-Carman's expression, expressed as a function of packing fraction ϕ:

$$k = \frac{(1-\phi)^3}{45\phi^2}r^2 \tag{1.19}$$

Two constitutive equations describe the mechanical behavior of the biphasic medium:

$$\sigma_{ij} = \lambda\delta_{ij}\,\mathrm{tr}\boldsymbol{\varepsilon} + 2\mu\varepsilon_{ij} - \alpha p\delta_{ij} \tag{1.20}$$

and

$$\xi = \alpha \, \mathrm{tr}\boldsymbol{\varepsilon} + \frac{1}{\mathrm{M}} p \tag{1.21}$$

with λ and μ the drained Lamé coefficients, *i.e.* the elasticity coefficients of the solid skeleton in the absence of the liquid phase, and α and M two coupling parameters:

- the Biot-Willis coefficient α represents the variation of stress $\boldsymbol{\sigma}$ with pressure p at constant strain $\boldsymbol{\varepsilon}$; it also represents the variation of fluid content with volume $(\frac{\partial \xi}{\partial \mathrm{tr}\boldsymbol{\varepsilon}})$ at constant pressure p;
- the Biot modulus M represents the variation in pore pressure p with fluid content ξ at constant strain.

The Biot-Willis coefficient can be expressed as $\alpha = 1 - \frac{k_d}{k_s}$ with k_s the bulk modulus of the solid phase material and k_d the drained bulk modulus (Biot, 1962). In drying colloidal suspensions with hard particles, the porous particle network is much more compliant than the particles themselves, and $\alpha \simeq 1$. In addition, $\frac{1}{\mathrm{M}} = 0$ for an incompressible fluid.

Finally, in the absence of body forces, momentum balance for the biphasic medium can be expressed as:

$$\nabla . \boldsymbol{\sigma} = 0 \tag{1.22}$$

2 Poroelasticity applied to colloidal layers

Poroelasticity theory yields estimates for the stresses arising in a colloidal layer during the second stage of the drying (fig. 1.4b-c). Assuming one-dimensional vertical drying, the colloidal suspension can be modeled as an infinite layer of thickness h, translation invariant along the x and y directions (Scherer, 1989; Chekchaki, 2011; Chekchaki and Lazarus, 2013).

In addition to the equations 1.16-1.22 above, the following boundary conditions apply:

- At $z = 0$ (suspension/substrate interface), $\boldsymbol{u} = \mathbf{0}$ (the colloidal layer adheres to the non-deformable substrate) and $\frac{\partial p}{\partial z} \propto \boldsymbol{v}.\boldsymbol{e_z} = 0$ (the substrate is impermeable);
- At $z = h$ (suspension/air interface), $\boldsymbol{\sigma}.\boldsymbol{e_z} = 0$ (stress-free interface) and $\boldsymbol{v}.\boldsymbol{e_z} = \dot{\mathrm{E}}$.

The pressure p can then be shown to obey a diffusivity equation:

$$\frac{\partial p}{\partial t} = \mathrm{D}_p \frac{\partial^2 p}{\partial z^2} \tag{1.23}$$

with D_p the hydraulic diffusivity of consolidation coefficient, defined by

$$D = \frac{k}{S\eta} \text{ with } S = \frac{\alpha^2(1+\nu)(1-2\nu)}{E(1-\nu)} + \frac{1}{M} \tag{1.24}$$

From the above equations and the boundary conditions, one can express the pressure, the displacement and finally the stress field in the layer (Scherer, 1989):

$$\sigma_{xx} = \sigma_{yy} = -\alpha \frac{1-2\nu}{1-\nu} p \tag{1.25}$$

with

$$p(z,t) = -\frac{\eta \dot{E} h}{k} \left[\frac{z^2}{2h^2} + \frac{D}{h^2} t - \frac{1}{6} - \frac{2}{\pi^2} \sum_{m=1}^{+\infty} \frac{(-1)^m}{m^2} \exp\left(-\frac{m^2 \pi^2 D t}{h^2} \right) \cos\left(\frac{m\pi z}{h} \right) \right] \tag{1.26}$$

As the pressure $p(z,t)$ is negative, σ_{xx} and σ_{yy} are positive; that is, the layer is in tension[1]. Note that, from eq. 1.20, the total stress in the layer σ_{ij} can be understood as the sum of a pressure contribution from the liquid, $-\alpha p \delta_{ij}$, and an effective stress in the solid network,

$$\widetilde{\sigma}_{ij} = \lambda \delta_{ij} \operatorname{tr}\boldsymbol{\varepsilon} + 2\mu \varepsilon_{ij} \tag{1.27}$$

From eq. 1.20 and 1.25, one has

$$\widetilde{\sigma}_{xx} = \widetilde{\sigma}_{yy} = \alpha \frac{\nu}{1-\nu} p \leqslant 0 \tag{1.28}$$

$$\widetilde{\sigma}_{zz} = \alpha p \leqslant 0 \tag{1.29}$$

with $\widetilde{\sigma}_{ij} = 0$ for all $i \neq j$. Although the total stress $\boldsymbol{\sigma}$ is tensile, the stress on the particle network $\widetilde{\boldsymbol{\sigma}}$ is indeed compressive and drives particle compaction during the second stage of the drying (fig. 1.4b-c). In the presence of a flaw, the stress $\widetilde{\boldsymbol{\sigma}}$ becomes tensile at the crack tip: thus the crack is able to propagate, despite the particle network being in compression (Scherer, 1992).

Drying colloidal suspensions on a mercury bath (Chiu et al., 1993) or on glass substrates treated with grease (Groisman and Kaplan, 1994; Thiery et al., 2015) yields an experimental verification of the importance of substrate adhesion on crack formation. In the absence of adhesion between the layer and the substrate (that is, when the boundary condition $\boldsymbol{u}(z = 0) = \mathbf{0}$ is relaxed), cracks are reduced or

[1] Note the opposite sign conventions on p and $\boldsymbol{\sigma}$: a fluid under positive pressure is in compression, while a solid under positive stress is in tension.

eliminated. Desiccation cracks thus arise from the strain mismatch created by simultaneous substrate adhesion and shrinking caused by capillary pressure.

When a colloidal suspension is dried on a flexible beam, the shrinkage of the layer causes the beam to deflect. From this deflection, the stress state in the layer can be obtained (Stoney, 1909; Yow et al., 2010; Chekchaki et al., 2011). Using this method, Chekchaki and Lazarus, 2013 have shown that the stress state is in agreement with a quasi-constant evaporation rate at the evaporation surface. This boundary condition yields a growing negative pressure in the pores (eq. 1.26) which arises from the progressive receding of the menisci at the interface.

3 Fracture mechanics

When a solid is subjected to stresses, it can respond continuously through elastic (reversible) or plastic (irreversible) deformation. Above a critical applied load, the material can respond catastrophically, by fracture.

As a crack opens, new surfaces are exposed on the material. Fracture thus involves the rupture of bonds between atoms, which requires energy: from $\sim 10^{-20}$ J for hydrogen bonds (*i.e.* in liquid or weakly bond solids) to $\sim 10^{-19}$ J for ionic or covalent bonds (*i.e.* in solids).

The propagation of a crack allows the material to deform to release stresses and decrease its stored strain energy. Griffith criterion (Griffith, 1921) states that a fracture will nucleate or propagate if the energy expanded for surface creation is lower than the energy gained through elastic relaxation:

$$G \geqslant G_c \tag{1.30}$$

where G is the elastic energy release rate and G_c the fracture energy (that is, the energy required to open a unit area of crack). In ideally brittle materials, G_c can be estimated as the product of bond energy and bond density, as fracture only requires rupture of the atomic bonds over the crack plane. However, fracture generally involves dissipation processes in a small volume in the vicinity of the crack tip, making G_c much higher than expected from the value of bond energy.

The propagation of a crack can also be understood as due to stress concentration at the vicinity of the crack tip. The opening of a crack can be described as the superposition of three modes (fig. 1.5): opening (mode I), in-plane shear (mode II) and out-of-plane shear (mode III). In the vicinity of the crack tip, the stress in the

material diverges as $1/\sqrt{r}$ and can be expressed as

$$\sigma_{ij} = \frac{K_I}{\sqrt{2\pi r}} f_{ij}^{I}(\theta) + \frac{K_{II}}{\sqrt{2\pi r}} f_{ij}^{II}(\theta) + \frac{K_{III}}{\sqrt{2\pi r}} f_{ij}^{III}(\theta) \tag{1.31}$$

where f_{ij}^{I}, f_{ij}^{II} and f_{ij}^{III} are universal functions. K_I, K_{II} and K_{III} are called the stress intensity factors; they are a function of the load applied and of the geometry of the crack (Lawn, 1993).

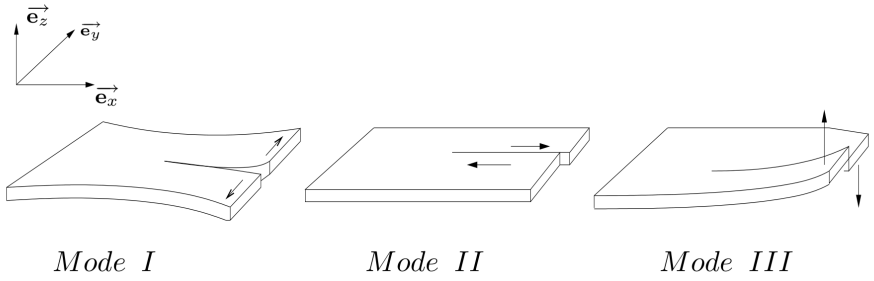

FIGURE 1.5: Schematics of the three crack modes: opening (mode I), in-plane shear (mode II) and out-of-plane shear (mode III).

Consider as an example a drying colloidal layer of thickness h adhering to a non-deformable substrate along the (xy) plane, as illustrated on fig. 1.6, with a crack of length $L_0 \gg h$. Far away from the crack tip, the stress in the layer is $\sigma_{xx} = \sigma_{yy} = \sigma_0$, given by eq. 1.25. The crack is loaded in mode I only, so that $K_{II} = K_{III} = 0$ and K_I can be expressed as (Xia and Hutchinson, 2000):

$$K_I = \sigma_0 \sqrt{h} \tag{1.32}$$

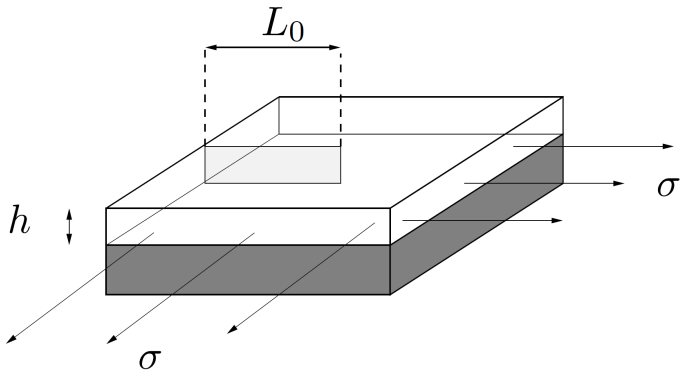

FIGURE 1.6: Propagation of a single crack in a drying colloidal layer adhering to a non-deformable substrate (in grey).

Irwin's criterion for fracture then states that crack propagation happens when the stress intensity factor exceeds a critical value, that is

$$K_I \geqslant K_c \tag{1.33}$$

where the fracture toughness K_c is a material constant (Irwin, 1957). The fracture energy G_c can be expressed as

$$G_c = K_c^2 \frac{1-\nu^2}{E} \tag{1.34}$$

where E is the Young's modulus and ν the Poisson ratio of the material.

Chapter 2

From the liquid suspension to the dry solid material

This chapter first introduces the suspensions used as model colloidal system, Ludox HS, SM and TM, and gives their relevant properties. Then, the drying process the samples are subjected to is presented. Finally a few results relative to the behavior of dry layers at long timescales are given.

I A model colloidal system

1 General properties of Ludox colloidal silica

Ludox colloidal suspensions are slightly basic ($p\mathrm{H} \simeq 9 - 10$) suspensions of very small amorphous silica ($\mathrm{a-SiO_2}$) spheres in water. The silica particles are grown chemically by the polymerization of silicic acid; they are negatively charged with sodium as the counter-ion, in order to prevent their aggregation. Ludox suspensions are used industrially as organic binders for granular and fibrous materials, for example as an anti-slip additive for flooring or in the manufacture of paper. They are manufactured by Grace Davidson and packaged by Sigma-Aldrich in 1 L bottles for lab use. Ludox suspensions are a good model system for stiff colloids (that is, colloids with only weakly deformable particles).

Studies presented in this manuscript involve three different types of Ludox suspensions:

- SM (for Ludox SM-30) with particle radius $r \simeq 5.5\,\mathrm{nm}$
- HS (for Ludox HS-40) with particle radius $r \simeq 8\,\mathrm{nm}$
- TM (for Ludox TM-40) with particle radius $r \simeq 14\,\mathrm{nm}$

	SM	HS	TM
Silica (mass fraction)	$0.29 - 0.31$	$0.39 - 0.41$	$0.39 - 0.41$
Surface area (m^2/g)	$320 - 400$	$198 - 258$	$110 - 150$
Particle radius (nm)	$3.7 - 4.6$	$5.7 - 7.4$	$9.8 - 13.4$
Sodium (SiO_2/Na_2O molar ratio)	$45 - 56$	$89 - 101$	$200 - 250$
pH	$9.7 - 10.3$	$9.2 - 9.9$	$8.5 - 9.5$

TABLE 2.1: Specifications supplied by the producer for the three Ludox suspensions used in this study. Particle radius (r) is inferred from specific area (s) using $r = 1/(3\rho_{sil}s)$ with $\rho_{sil} = 2.26\,g/cm^3$ (see chap. 3 for the determination of silica density).

Table 2.1 gives the values specified by the producer (Grace Davidson) for the three suspension types.

The three suspensions are chemically very similar, as they are aqueous suspensions of silica nanospheres. However, they differ in their pH and sodium concentration. This difference is significant as it will play a role in some observations made in this manuscript. The larger the particle radius r, the lower the pH and amount of sodium:

- Ludox TM (particle radius $r \simeq 14\,nm$) has the smallest amount of sodium ($\sim 0.5\%$ of Na_2O as a percentage of silica mass)
- Ludox HS ($r \simeq 8\,nm$) has $\sim 1\%$ of Na_2O.
- Ludox SM ($r \simeq 5.5\,nm$) has the largest amount of sodium ($\sim 2\%$ of Na_2O).

This difference arises because smaller particles are less stable with respect to aggregation. Ensuring the stability of the suspension requires higher repulsive electrostatic interactions between the particles, which means higher surface charge and consequently higher counter-ion concentration. In short, Ludox suspensions with smaller particles require higher amounts of Na_2O for stability.

2 In-house characterization of the suspensions

The specifications provided by Grace Davidson only give a rough estimate of particle size, which exhibits some batch to batch variations. Moreover, there is no information on the polydispersity of the suspension: Grace Davidson states that the suspension are monodisperse but does not provide any value for the spread in actual particle size, which is always non-zero. In order to infer particle size and polydispersity for the specific suspension batches used in this study, I conducted small-angle

X-ray scattering (SAXS) measurements at LPS (Orsay, France) under the guidance of Marianne Impéror.

The theory of small-angle X-ray scattering, as well as the methods we used in this study, are detailed in appendix A. In short, SAXS measurements on granular media yield *global* average information which depends on both the structure of the sample (*i.e.* the correlations in particle positions) and its grain shape and size. Invoking SAXS on dilute colloidal suspensions, in which particles are spheres with uncorrelated positions, directly provides information on the size distribution of the particles. I measured the form factor of dilute Ludox suspensions, and the median particle size (R_m) and dispersity index (σ) were subsequently inferred by fitting a model form factor (the form factor for a lognormal distribution) to the experimental data.

Table 2.2 gives the inferred particle size and polydispersity from SAXS experiments for each of the four Ludox batches under study. We used two batches of Ludox HS. The first (batch number STBF8427V) was used by K. Piroird during his post-doctorate in 2014, and was relatively monodisperse (σ/r_m = 0.14). The second batch (batch number STBF8427V), used during my PhD, has higher polydispersity (σ/r_m = 0.31). In the rest of this manuscript, the first batch will thus be referred to as the HS-m (”monodisperse”) suspension, whereas the second one will be referred to as the HS-p (”polydisperse”) suspension. As we will show in the following chapters, these two suspensions yield dry layers with contrasting properties.

Suspension	Batch number	R_m (nm)	σ/R_m
SM	MKBP6397V	5.5	0.19
HS-m	BCBK7778V	8.1	0.14
HS-p	STBF8427V	8.6	0.31
TM	05105EE	14.0	0.10

TABLE 2.2: Median particle radius and relative polydispersity for the four Ludox batches used in this study, obtained by fitting the measured form factors to a lognormal distribution. Batch STBF8427V has much higher dispersity than batch BCBK7778V, despite both of them being sold as monodisperse HS-40.

II Experimental setup

Layers obtained through colloidal drying differ in many of their properties, such as porosity, stiffness, mechanical strength (Sibrant and Pauchard, 2016)... One of the most conspicuous and industrially relevant properties of colloidal layers is their

propensity to crack during the drying process. Many experimental parameters, such as the stiffness and surface energy of the particles, the composition of the liquid phase (Pauchard et al., 1999; Boulogne et al., 2012), the initial thickness of the layer (Lazarus and Pauchard, 2011), or the adhesion of the substrate (Groisman and Kaplan, 1994; Lazarus, 2017), play a role on the formation of the crack network and on the size and shape of the resulting morsels.

Notably, the relative humidity RH of the drying atmosphere is an easily tunable parameter which affects the evaporation rate and thus influences the cracking of the colloidal layers (Caddock and Hull, 2002; Boulogne et al., 2014). I thus selected it as the control parameter in all the experiments. Relative humidity is defined as the ratio between the concentration of water vapor in the atmosphere under consideration (proportional to the partial pressure of water P_{H_2O}) and the concentration of water vapor in saturated atmosphere (proportional to the saturation pressure $P_{sat,H_2O}(T)$):

$$RH = \frac{P_{H_2O}}{P_{sat,H_2O}(T)} \tag{2.1}$$

RH ranges between 0 (for a completely dry atmosphere) and 1 (for an saturated atmosphere). In the rest of the manuscript, it will generally be expressed as a percentage.

Samples from the four suspension batches were dried at room temperature under varying humidities, from RH = 10% (dry atmosphere, fast evaporation) to RH = 95% (humid atmosphere, slow evaporation). The typical duration of an experiment varied between two days and three weeks. For HS-m and HS-p suspensions, 8 drying experiments were made on each suspension (tab. 2.3 and 2.4); for SM and TM, only 4 experiments per suspension were made (tab. 2.5 and 2.6), spanning a reduced number of RH. The drying and storage protocols used were the same for all layers, except for the ones obtained from the HS-m suspension. The HS-m layers were prepared by K. Piroird in 2014, before the beginning of this PhD work (2015), and the protocols were slightly different. Relevant differences will be detailed in the text.

The following sections introduce the experimental setup and protocol and present a few elementary observations on the drying experiment, such as the evolution of mass and layer appearance with time.

1 Drying setup

A Labview routine, interfaced with a scale (Sartorius Cubis MSE225S, display resolution 10^{-5} g) and a hygrometer, records the suspension mass (m) as well as the

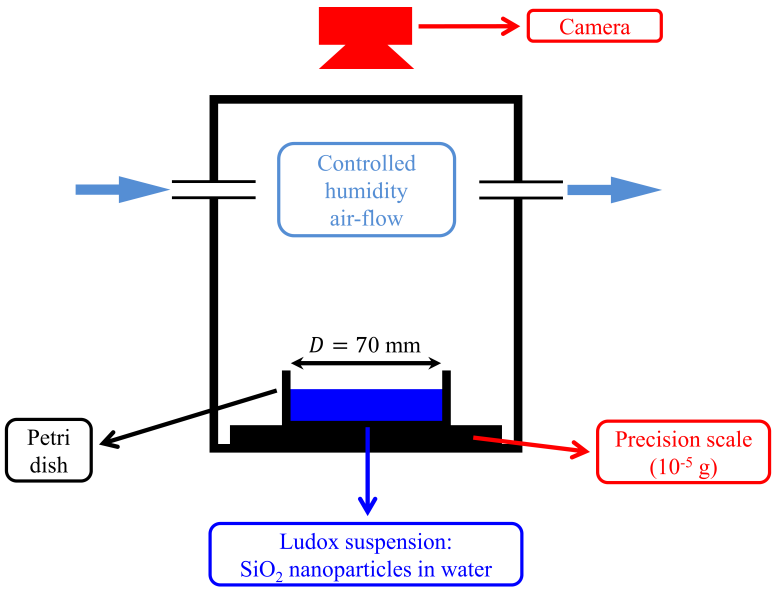

FIGURE 2.1: Schematic of the drying setup used for the preparation of the colloidal layers. The colloidal suspension is poured in a Petri dish and left to dry in an enclosure under controlled humidity. A precision scale and a camera record the mass and visual evolution of the sample. Schematic is not to scale. Internal dimensions of the enclosure: 200x200x260mm (width x depth x height).

temperature (T) and the relative humidity (RH) in the enclosure. Additionally, this routine maintains the relative humidity in the scale enclosure around a prescribed value RH_c. When the relative humidity RH drifts from RH_c by more than 1%, a pump forces air from the scale enclosure into either a drying circuit (columns of silica gel, which absorbs moisture) or a humidifying circuit (a water bottle in which the air stream bubbles). This allows monitoring of the RH value. The entire setup (scale enclosure and pump circuits) is made airtight using glove box quality putty; sealing quality is especially important at low RH, as ambient air is a source of humidity. A camera placed above the enclosure and interfaced with a second Labview routine captures images of the drying colloidal layer at specified time intervals.

2 Sample preparation

Ludox suspensions are used directly as supplied by Grace Davidson; that is, no treatment such as washing or filtering occurs before the drying experiments. The initial suspension mass m_0 is chosen such that the final layer represents 10 g of dry solid material. Hence, m_0 = 25 g for HS-m, HS-p and TM suspensions (initial mass

concentration ϕ_m = 40%) and m_0 = 33.33 g for SM suspensions (initial mass concentration ϕ_m = 30%).

Glass Petri dishes (diameter 7 cm) hold the suspension during drying. The Petri dishes are washed with soap and rinsed in water, with a final rinse in deionized water. The Petri dish rests on the scale, which is protected by a sheet of black paper (graph paper for the HS-m experiments); the scale is zeroed and a mass m_0 of suspension is poured.

During the drying experiment, the sample mass decreases as water evaporates off the suspension. After some time, the mass of the drying layer stabilizes to its final value. However, samples dried at high relative humidities may retain a significant amount of water in their pores (up to 25% in mass). Thus, all HS-p, SM and TM layers undergo a "quenching" process by dropping RH_c to 10% until their mass is stable again. HS-m layers were not quenched to RH_c = 10%; rather, they were brought back to ambient humidity (RH $\simeq$ 40%) in a stepwise process. Both procedures remove most of the remaining water from the samples, as a heat treatment of the samples at 200° C (which is expected to make them completely dry) only results in $1-2$% mass loss.

TABLE 2.3: Command relative humidity (RH_c), measured relative humidity (RH), temperature (T) and evaporation rate ($\dot{E}_0$) for the 8 layers dried from the HS-m suspension. Initial mass was m_0 = 25 g for all the layers.

RH_c (%)	RH (%)	T (° C)	$\dot{E}_0$ (nm/s)
10	$11.4_{\pm 1.3}$	$24.7_{\pm 0.5}$	35.8
23	$23.6_{\pm 0.5}$	$27.5_{\pm 0.3}$	29.7
36	$36_{\pm 0.8}$	$27_{\pm 0.3}$	25.7
50	$50_{\pm 1.1}$	$24_{\pm 0.7}$	17.7
65	$65_{\pm 1.1}$	$23.6_{\pm 0.5}$	12.7
80	$80_{\pm 0.9}$	$24.1_{\pm 1.1}$	7.2
90	$90.8_{\pm 1.4}$	$25.5_{\pm 0.4}$	4.8
95	$96_{\pm 2.3}$	$26.4_{\pm 1.8}$	3.5

Dry layers tend to absorb moisture from the air; thus, the storage procedure might have some influence on the properties of the layers. HS-m layers are kept in ambient conditions, whereas HS-p, SM and TM layers are stored in boxes with silica gel, in order to create a lower-RH environment. The storage room is air-conditioned with constant temperature T = 23 ± 2° C.

TABLE 2.4: Command relative humidity (RH_c), measured relative humidity (RH), temperature (T) and evaporation rate ($\dot{E}_0$) for the 8 layers dried from the HS-p suspension. Initial mass was m_0 = 25 g for all the layers.

RH_c (%)	RH (%)	T (° C)	$\dot{E}_0$ (nm/s)
10	$9.3_{\pm 0.3}$	$21.2_{\pm 0.3}$	28.1
23	$24.6_{\pm 2.3}$	$23_{\pm 0.5}$	22.8
36	$37.4_{\pm 2.9}$	$23.2_{\pm 0.5}$	19.5
50	$50.4_{\pm 3.3}$	$22.9_{\pm 0.4}$	16.5
65	$63.7_{\pm 3.4}$	$22.5_{\pm 0.4}$	13.5
80	$77.8_{\pm 2.8}$	$23.9_{\pm 2.2}$	10.8
90	$89.5_{\pm 2.1}$	$23.7_{\pm 1.1}$	4.9
95	$95.3_{\pm 0.7}$	$22.4_{\pm 0.7}$	3.2

TABLE 2.5: Command relative humidity (RH_c), measured relative humidity (RH), temperature (T) and evaporation rate ($\dot{E}_0$) for the 4 layers dried from the SM suspension. Initial mass was m_0 = 33.33 g for all the layers.

RH_c (%)	RH (%)	T (° C)	$\dot{E}_0$ (nm/s)
10	$10.7_{\pm 0.6}$	$22.4_{\pm 1.4}$	27.3
36	$37_{\pm 2.8}$	$21.7_{\pm 0.6}$	18.4
80	$78.5_{\pm 3}$	$21.5_{\pm 0.3}$	5.9
95	$95.5_{\pm 0.5}$	$21.8_{\pm 0.6}$	2.6

TABLE 2.6: Command relative humidity (RH_c), measured relative humidity (RH), temperature (T) and evaporation rate ($\dot{E}_0$) for the 4 layers dried from the TM suspension. Initial mass was m_0 = 25 g for all the layers.

RH_c (%)	RH (%)	T (° C)	$\dot{E}_0$ (nm/s)
10	$14.4_{\pm 1.1}$	$22.3_{\pm 0.3}$	22.6
36	$35.9_{\pm 2.7}$	$22.1_{\pm 0.2}$	17.4
80	$78_{\pm 3.3}$	$22.4_{\pm 0.3}$	7.6
95	$95.6_{\pm 0.4}$	$21.9_{\pm 0.5}$	2.3

3 Layer evolution during drying

3.1 Mass curves

Drying the colloidal layers on a scale allows the measurement of mass evolution with time. Figure 2.2 shows two mass curves, obtained with RH_c = 23% and 80% for HS-p suspension. The mass loss rate of the suspension is defined as $\dot{m}(t) = \frac{dm(t)}{dt}$. As water evaporates from the suspension, the free surface of the liquid gradually moves down; the corresponding speed, called the evaporation rate or drying rate, can be expressed as

$$\dot{E}(t) = \frac{\dot{m}(t)}{\rho_w \pi R^2} \tag{2.2}$$

with ρ_w the density of water and R = 7 cm the diameter of the Petri dish. During the first phase of colloidal drying, the mass loss is nearly linear; that is, $\dot{m}$ and $\dot{E}$ are constants, respectively coined $\dot{m}_0$ and $\dot{E}_0$. In the rest of the thesis, the expression "drying rate" will, unless specified otherwise, refer to the *initial* drying rate $\dot{E}_0$.

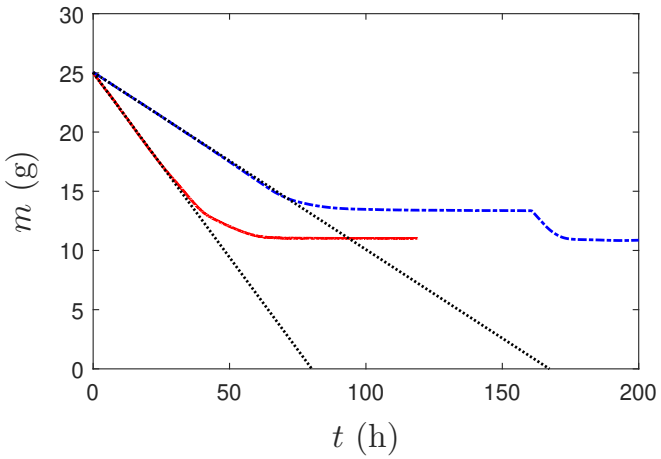

FIGURE 2.2: Evolution of layer mass with time on two experiments on HS-p suspension, with RH_c = 23% (red solid line) and RH_c = 80% (blue dashed line). Black dotted lines represent linear fits on the part of the experiment with $m > 20$ g: they evidence that the mass loss is initially linear with time. The slowly-dried sample was quenched in dry atmosphere (RH = 10%) at $t = 160 - 180$ h.

The mass loss rate of the silica suspension can be compared to that of pure water. As a pure liquid evaporates, the atmosphere at the vicinity of the liquid interface is more concentrated in vapor than the atmosphere far from the interface. Denoting h_{lim} the height of the concentrated layer, and using a one-dimensional transport model over this interface, the evaporation rate of pure water can be expressed as

(Coussot, 2000):

$$\dot{E}_0 = \frac{D}{h_{lim}} \frac{n_{sat}}{n_{liq}} (1 - RH) \tag{2.3}$$

where D is the diffusion coefficient of vapor in air, n_{sat} the number of water molecules per unit volume in water-saturated atmosphere and n_{liq} the number of water molecules per unit volume in the liquid phase. D and n_{sat} are strongly temperature-dependent. However, assuming constant temperature and that h_{sat} does not depend on RH, the evaporation rate is a linear function of $1 - RH$. Experiments herein were run at constant temperature for a given suspension ($T = 23 \pm 2^\circ$ C for HS-p, SM and TM layers and $T = 25 \pm 2^\circ$ C for HS-m layers). Figure 2.3 evidences the relationship between $(1 - RH)$ and $\dot{E}_0$, which is approximatively linear. However, there are some discrepancies which may be due to the slight temperature differences between the different experiments. Hence $\dot{E}_0$ is used as the control parameter in the rest of the manuscript.

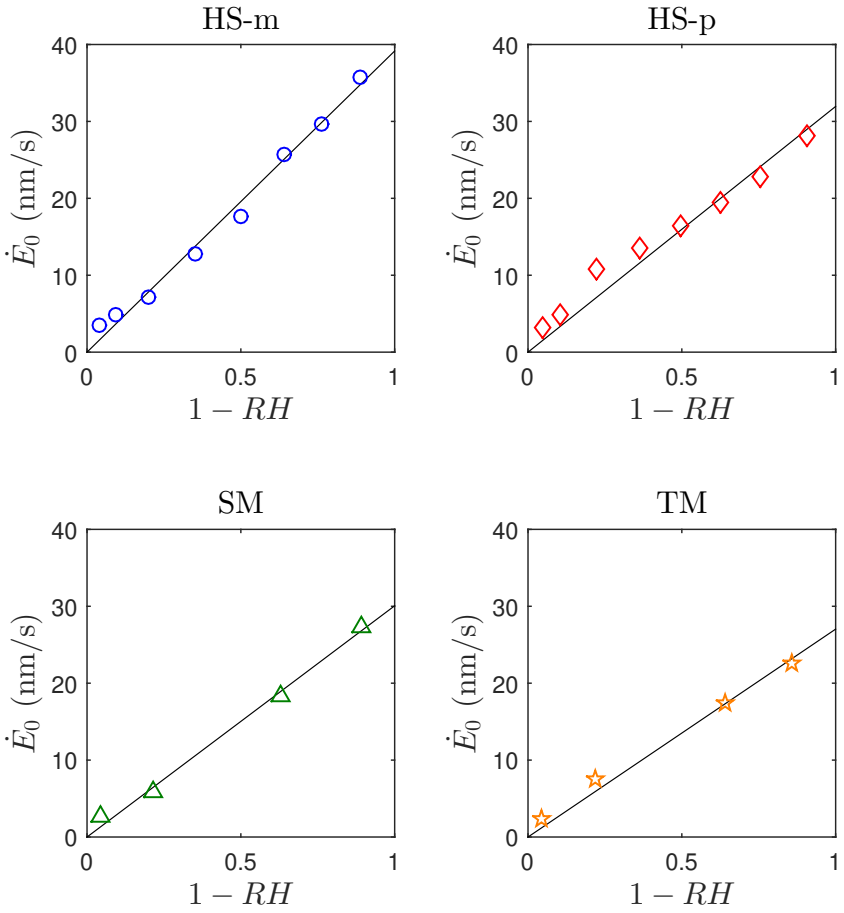

FIGURE 2.3: Evaporation rate $\dot{E}_0$ as a function of relative humidity RH for all drying experiments. Black lines represent linear fits (the data for each suspension were fitted separately). Temperature variations from experiment to experiment explain the deviation of experimental data from the expected linear law.

3.2 Visual appearance

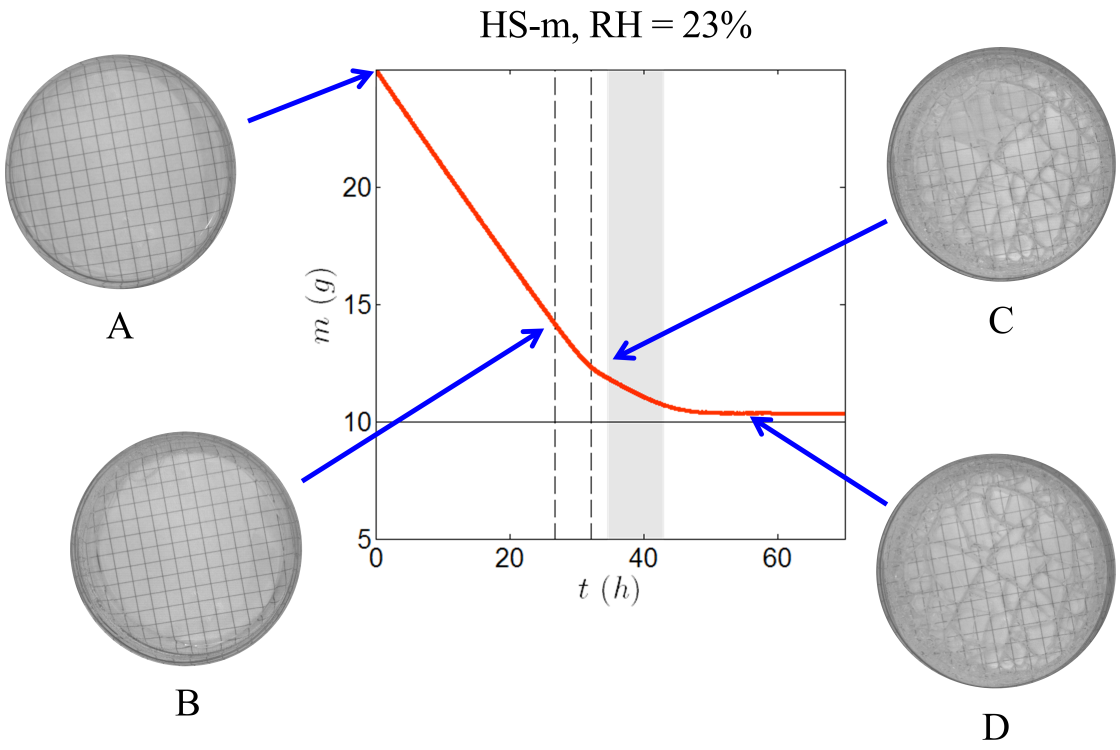

FIGURE 2.4: Mass evolution of a layer of HS-m suspension dried at RH = 23%. The layer is pictured at four different stages: (A) beginning of the drying; (B) beginning of crack formation; (C) beginning of the opaque phase; (D) end of the drying. The two vertical dashed bars delimit the beginning and the end of fracture formation. The gray vertical band represents the opaque phase.

Concurrently to the measurement of mass evolution, image acquisition tracks the evolution of the visual appearance of the layers. As the layers dry, they all undergo the same transformations.

- During the first phase of the drying, the layer remains clear and continuous (fig. 2.4A). When dried at very high evaporation rate (RH $\leqslant$ 10%), layers tends to buckle as they gel. This is sometimes visible on camera. Layers dried at other RH do not buckle and the gelling of the suspension is not visible via the camera.
- At some point in the drying close to the end of the linear period ($\dot{m}(t) = \dot{m}_0$), a hierarchical network of cracks begins to form in the layer (fig. 2.4B).

- As soon as a crack is formed, it starts widening and the adjacent morsels delaminate, from their edge (where they touch the crack opening) to their center. This happens as other cracks are still opening.
- At some point, the layer becomes opaque (fig. 2.4C). This normally happens once the formation of the crack network is complete. However, layers dried at RH = 10% can have directional drying, with one side of the sample drying faster than the other does. On these layers, opacification can coexist with fracture formation.
- Finally (fig. 2.4D), the layer becomes transparent again (it may still show a very slight opalescence). Sometimes thin, non-opening cracks can form during the opaque phase and become visible at this stage.

III When is dry really dry?

At the end of the drying experiment, layer mass and appearance stop evolving. However, chemical and structural changes can still take place in the layers: sintering and grain growth can occur, especially in the presence of absorbed water. The following section presents results on the evolution of the layer properties on time scales ranging from a few days to a few months after mass is stabilized.

1 Structural evolution on long time scales

1.1 Small-angle X-ray scattering

In order to obtain information on the structure of our materials, I performed small-angle X-ray scattering (SAXS) on dry solid layers. The following section summarizes the theory of SAXS measurements. A summary of the experimental setup and the methods used in this work is given in appendix A.

SAXS experiments use a monochromatic, collimated X-ray beam to measure the material inhomogeneities at the particle scale. As the beam goes through the sample, most photons remain undeflected, but some of them are scattered as a result of differences in electron density. A detector placed behind the sample measures the scattered intensity I as a function of the scattering vector, defined as $\vec{q} = \vec{k} - \vec{k_0}$, with $\vec{k_0}$ the wavevector of the incident beam and $\vec{k}$ the wavevector of the scattered beam (see fig. 2.5). For an isotropic sample, such as an amorphous or polycrystalline solid, the scattered intensity is rotationally invariant, and only depends on $q = |\vec{q}|$, which

can be expressed as

$$q = \frac{4\pi sin(\theta)}{\lambda} \tag{2.4}$$

with 2θ the scattering angle and λ the wavelength of the beam.

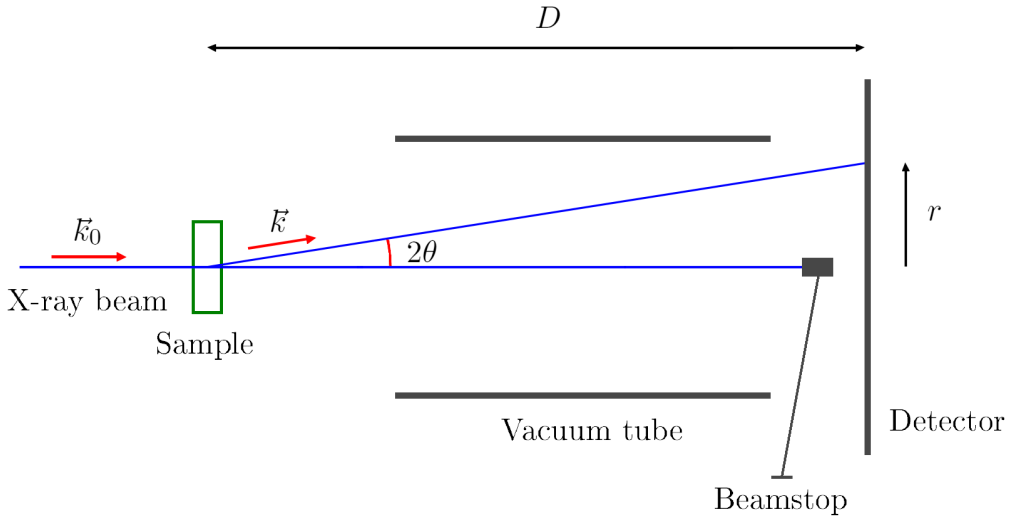

FIGURE 2.5: Basic setup of a SAXS experiment

The intensity I(q_0) diffracted at a given q_0 gives information on the material structure at a scale $d_0 = \frac{2\pi}{q_0}$. Small-angle X-ray scattering probes low q values (corresponding to $\theta < 0.1$) and provides information concerning comparatively larger structures ($d_0 \gg \lambda \sim 1$ Å). It is thus particularly useful in probing colloidal systems with particle sizes ranging between 1 and 100 nm in diameter. On the beamline used in this study, we could measure q in the range $q = 0.1 - 1.6\,\mathrm{nm}^{-1}$, corresponding to length scales $d = 4 - 60$ nm.

Since silica is fairly absorbent for X-rays, our layers as prepared in the experiments had a very low transmission coefficient. In order to allow for reasonable acquisition times, additional drying experiments were run, using half as much initial suspension ($m_0 = 12.5$ g) and yielding thinner layers (final thickness $h \sim 1$ mm).

The evolution of diffracted intensity on short timescales was measured on a layer of HS-p dried at RH = 10% with initial mass $m_0 = 12.5$ g. Figure 2.6 represents the measured intensity profiles a few hours after the end of drying (solid black curve), as well as 2 days (dashed green line) and 9 days (dotted red line) later. No shift in the position of the maximum intensity is visible. As the position of the maximum corresponds to a correlation distance, *i.e.* the particle separation, there is no change in the interparticle distance. Hence, layer porosity does not evolve after the end of drying.

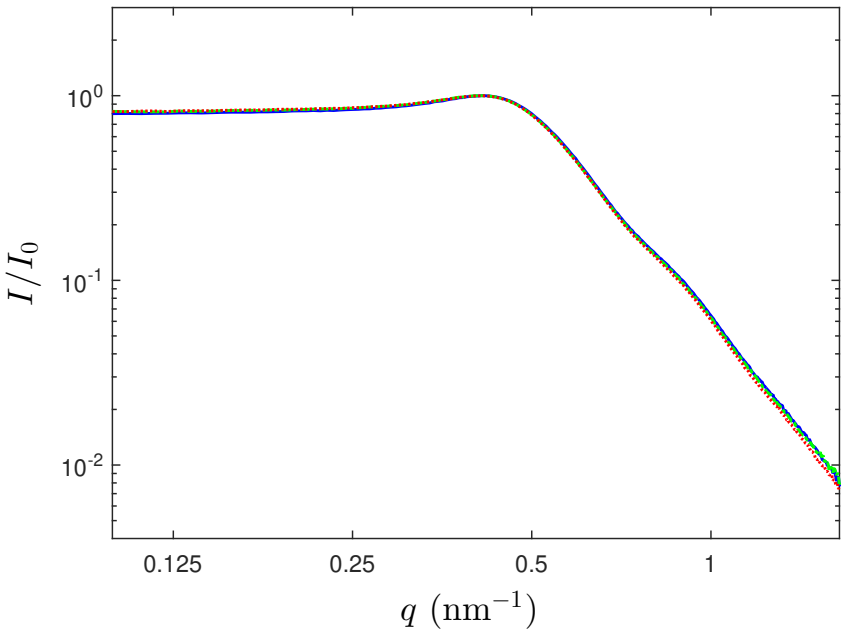

FIGURE 2.6: Intensity profiles for a sample dried at RH_c = 10% with initial mass m_0 = 12.5 g. Measurements were taken a few hours (solid black line), 2 days (dashed green line), and 9 days (dotted red line). No evolution of the signal is visible; in particular, there is no shift in the position of the intensity maximum.

The superposition of the three signals also underlines the excellent repeatability of the measurements.

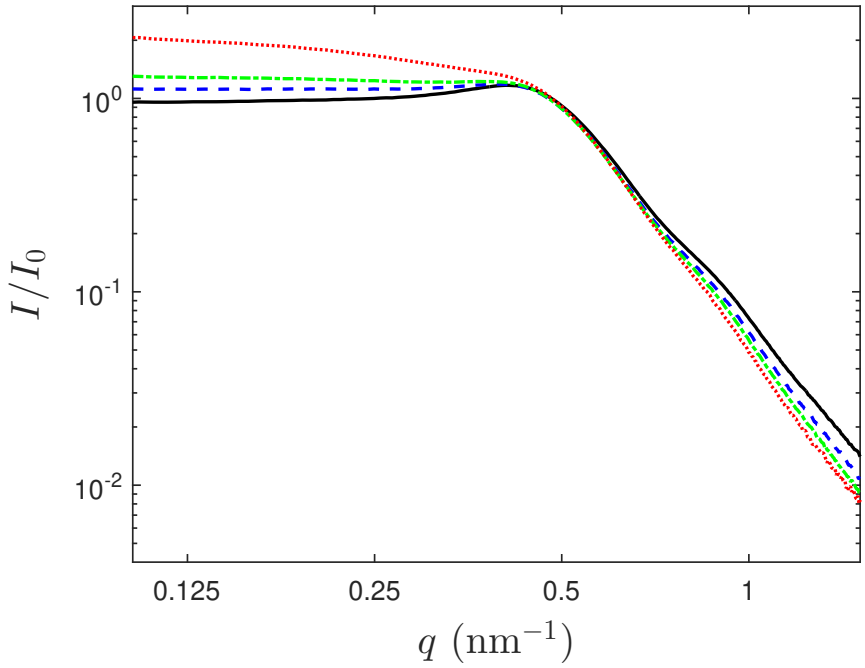

FIGURE 2.7: Intensity profiles for a sample dried at RH_c = 10% with initial mass m_0 = 12.5 g. Measurements were taken 4 days (solid black line), 49 days (dashed blue line), 89 days (dash-dot green line) and 192 days (dotted red line) after the end of the drying. The effect of aging is visible as a increase of the scattered intensity at small q.

In order to evidence structural changes in the silica layers on long time scales, another sample of HS-p suspension (m_0 = 12.5 g) was dried at RH_c = 10%. From the end of drying (t_0), measurements on the SAXS beamline (see fig. 2.7) were taken at $t = t_0 + 4$ days (solid black line), $t = t_0 + 49$ days (dashed blue line) and $t = t_0 + 89$ days (dash-dot green line). An increase of the scattered signal at low q (that is, larger scales in direct space) is visible.

This evolution could result either from a change in the structure of silica, or from the slow absorption of water from the atmosphere. In order to test this hypothesis, the sample was dismounted from the sample holder, dried in an oven (3 hours at 200°C), remounted on the holder, and subsequently remeasured (see fig. 2.8). No change in the signal is visible after the oven drying. Since the drying process drives off all water from the sample, the evolution of I(q) with time cannot be explained by water adsorption; it is indicative of an actual change in the structure of the silica. Although some water is probably reabsorbed by the sample after the oven treatment,

it is unlikely that a significant amount would be absorbed in the few hours preceding the measurement. Moreover, water absorption by the porous layer would be expected to eventually saturate, whereas the increase in scattered intensity at small angles does not saturate on the time scales considered here (months). Visual observation of the layers also suggests the silica structure is evolving: as the samples age, they become whiter and more opaque, and this change is not reversed by oven drying.

The change of the layer structure measured in SAXS may be due to grain growth: as the grains grow, for example through the accretion of silica at the necks between particles, the characteristic length scale of the inhomogeneities in the layers increases, hence the evolution of the scattered intensity I(q) at low q. Since the initial characteristic length scale is of the order of the particle diameter, which is very small compared to the wavelength of visible light, an increase in this length scale would also make the layers more opaque, as they would scatter more light.

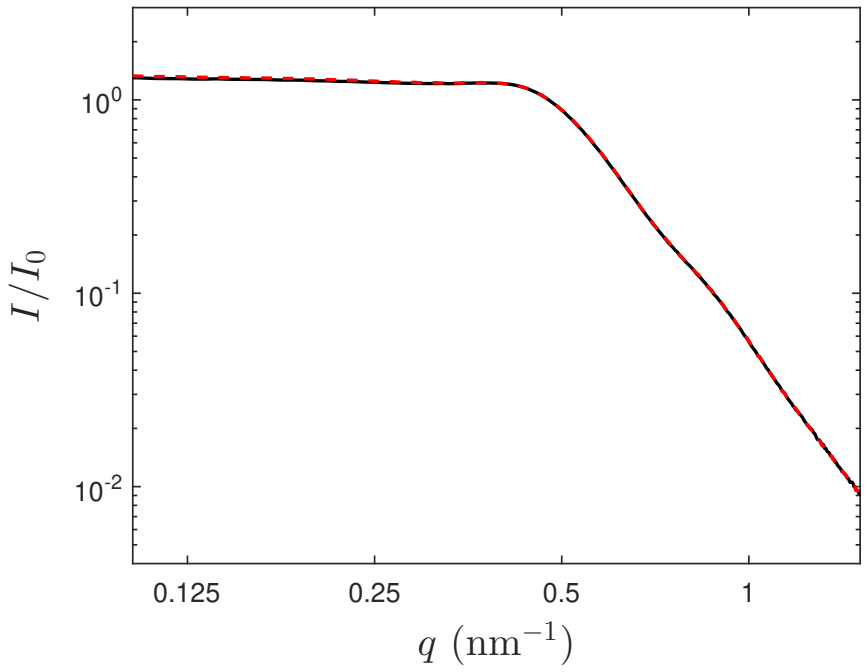

FIGURE 2.8: Intensity profiles for a sample dried at RH_c = 10% with initial mass m_0 = 12.5 g (same drying experiment as fig. 2.7). Measurements were taken at $t = t_0 + 89$ days before (solid black line) and after (red dashed line) drying the sample in an oven at 200° C. The oven drying removes most of the water from the pores, yet the scattered intensity is unchanged. Thus, the evolution of scattered intensity with time cannot be explained by water adsorption, but is instead indicative of structural changes in the layer.

Conclusion

This chapter introduced Ludox SM, HS, and TM, three industrial suspensions of colloidal silica which will be used as model colloids in this thesis. They are chemically very similar, and only differ in particle size. By measuring the form factor of dilute suspensions, we could infer particle size for the four batches on which we ran drying experiments. Notably, the two HS batches have different particle dispersity, one being much more polydisperse than the other.

We then presented the drying setup, as well as a few results concerning the drying process. Our experimental setup allows controlling the relative humidity of the drying atmosphere, which directly plays on the evaporation rate of the liquid phase. For each of the four Ludox batches, several dry layers were prepared with relative humidity ranging from 10% to 95%.

SAXS measurements of the dry colloidal layers revealed that they were still undergoing structural changes well after the apparent end of the desiccation process. However, in the rest of the manuscript, we will not be concerned with the temporal evolution of the layers properties. Rather, the mechanical and structural properties of the layers will be measured several months after their preparation, when they have been observed to be stable.

Chapter 3

Influence of drying rate and particle size on layer structure

In a previous article (Piroird et al., 2016), we studied layers obtained by drying HS-m suspension and evidenced the influence of drying rate and particle aggregation on the structure of the layers (particle arrangement and porosity). Layers dried at high evaporation rates showed a crystalline surface structure and a denser packing of the silica spheres in the bulk, while slowly-dried layers were amorphous and had lower compacity. This counter-intuitive transition from a ordered to a disordered system was explained by conjecturing aggregate formation: when layers dry slowly, they remain long enough in a concentrated, liquid state for silica particles to aggregate. These aggregates then preclude the crystallization and tighter packing observed in fast-dried layers. Our 2016 paper substantiated this conjecture using holding period experiments: layers dried at a high evaporation rate, but with a holding period introduced while the suspension is in a liquid concentrated state, show no crystallinity.

However, experiments performed during my PhD using HS-p suspension did not allow us to reproduce these results. SAXS analysis of the suspension revealed its higher polydispersity. This motivated us to extend the previous study using layers dried from three additional suspensions, HSp, TM and SM .

This chapter thus compares and contrasts the properties of layers obtained from the four suspensions. I first present the methods specific for this chapter: hydrostatic weighing for packing density and AFM imaging for surface structure. The structures of the colloidal layers are then compared and contrasted using two parameters (ψ_6 and $g(r)$) in order to quantify surface crystallinity. Finally, SAXS measurements on a suspension subjected to a holding period experiment confirm that aggregate formation explains the order to disorder transition observed in HS-m suspensions.

I Methods

1 Packing fraction

The packing fraction (or compacity) of the colloidal layers can be defined as the proportion of solid volume (V_s) to the total volume (V_T): $\phi = V_s/V_T$. The tightness of the particle packing can also be described using the porosity, p, which is defined as $p = 1 - \phi = V_p/V_T$, where V_p is the pore volume (with $V_T = V_s + V_p$). Thus, in order to estimate ϕ, it is necessary to measure at least two parameters of the three: V_s, V_p and V_T.

The volume V_s occupied by the solid particles can be expressed as $V_s = m/\rho_s$, where m is the mass of the sample and ρ_s is the density of the particles. The mass m of the samples was measured after a 3 hours heating treatment at 200°C, in order to evaporate off all water absorbed at the surface of the silica particles. In order to estimate the density of the silica particles, a dilution method, outlined in Caddock and Hull, 2002, was invoked on the HS-m suspension. Several dilutions of HS-m were prepared at prescribed mass fractions ϕ^m_{dil} and their densities ρ_{dil} were measured. From the relationship $1 - (\rho_w/\rho_{dil}) = \phi^m_{dil}(1 - (\rho_w/\rho_s))$, where ρ_w is the density of water, a linear regression yielded $\rho_s = 2.26 \pm 0.02\ \mathrm{g\ cm^{-3}}$.

A common expression for the packing fraction is: $\phi = V_s/(V_s + V_p)$. Thus, a first possibility is to measure V_p using an imbibition technique. The sample is weighted dry (mass m) and soaked with water (mass m_{wet}). The pore volume is the volume of water absorbed by the sample, $V_p = (m_{wet} - m)/\rho_w$. Such a method, however, yields the open porosity: that is, only pores which are linked to the surface of the sample are counted in the pore volume. Closed pores, which are not accessible to the water molecules, will actually be counted in the solid volume. Moreover, since the silica beads are only a few nanometers in diameter, it is doubtful that the water can fully fill the thinnest pores between the particles. Such a method risks underestimating V_p and thus overestimating ϕ.

A more accurate method invokes the measurement of V_T via hydrostatic weighting, in order to infer $\phi = V_s/V_T$. A sample of dried suspension is soaked in water and weighted in air (mass m_{wet}) and in water (apparent mass $\widetilde{m}_{wet}$) and V_T is expressed using Archimedes' principle: $V_T = (\widetilde{m}_{wet} - m_{wet})/\rho_w$. Note that if the pores are only partially filled, this will equally affect m_{wet} and $\widetilde{m}_{wet}$ and cancel out in the expression of V_T. Thus, the accuracy of this method does not require the complete filling of the pores by water, in contrast to the imbibition method previously outlined. Thus, I use this method in the rest of the study.

For each drying experiment, the packing fraction measurements were repeated on two morsels. For HS-m layers, one morsel was soaked and weighted in water, and another one in ethanol. The density of the ethanol bath was found to slightly increase with time, probably through water absorption from the atmosphere. For more accurate results, measurements on the layers obtained from the three other suspensions (HS-p, SM and TM) were made using water for all morsels.

2 Atomic Force Microscopy

In order to obtain spatial information on particle position, I used atomic force microscopy to image the drying surfaces of the layers. An atomic force microscope (AFM) uses a sharp tip (a few nanometers in diameter) to image the surface of a sample. Literature details how an AFM works, thus only experimental parameters will be presented therein.

I imaged the drying surfaces of the morsels using a Bruker Dimension Icon Nanoscope AFM mounted with a MPP-11220-10 tip. I transitioned to RTESPA-300 tips when Bruker phased out MPP-11220-10 tips; both models have a tip radius of 5 nm and were used in Tapping mode. For each drying experiment considered, a morsel is taken after the drying is complete and placed under the AFM head. To enable averaging of the surface properties, multiple images (500x500 nm^2, 512x512 $pixels^2$) are taken on the surface of each sample. As the samples are quite abrasive, tip wear occurs rapidly. The tip is thus replaced as soon as wear is visible, usually after 5 to 10 images.

In order to compute statistics on the arrangement of the colloidal particles, it is necessary to extract the position of the particle centers from the topographical images obtained via AFM. I used a Matlab routine which detects the local height maxima over the image. In order to avoid overdetection of particle centers, a parameter in the routine can be used to define the minimum separation between two centers. I adjusted this parameter to a value close to the particle size. Some spurious particle centers were still detected and manually removed. Figure 3.1 represents an typical output of this routine.

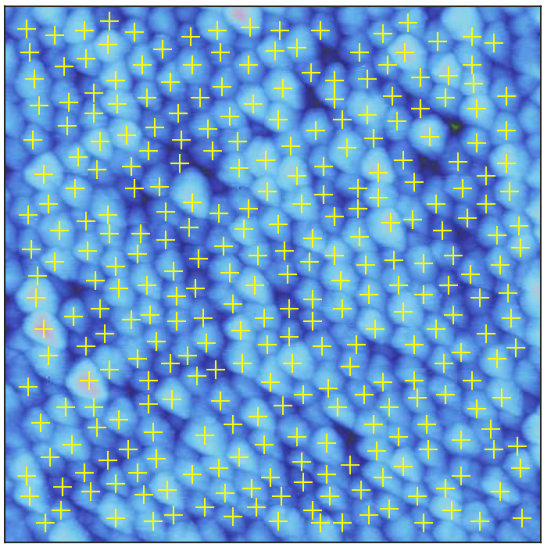

FIGURE 3.1: Typical topographical AFM image, taken from the surface of a TM layer dried at RH = 95%. Image size is 500x500 nm^2. Yellow crosses represent the positions of the particles centers as detected by the Matlab routine used in this study.

II Results

1 Packing fraction vs drying rate

Figure 3.2 provides the packing fraction as a function of the drying rate for the layers obtained from the four suspensions. Error bars are larger on the lower side, as they take into account the possible presence of water at the surface of the nanoparticles, which could lead to an up to 1.5% overestimation of ϕ (Iler, 1979).

For all layers, the packing fraction increases with increasing drying rate: slowly-dried layers are more porous. For layers obtained from HS-m and HS-p suspensions, there is a plateau in the packing fraction, for $\dot{E}_0 > 10\,nm/s$; at lower $\dot{E}_0$, the packing fraction decreases significantly. Compared to the HS-m and HS-p layers, layers obtained from SM suspension (smaller particles) are more porous at all drying rates. Conversely, layers obtained from TM suspension (larger particles) are less porous, especially at lower drying rates.

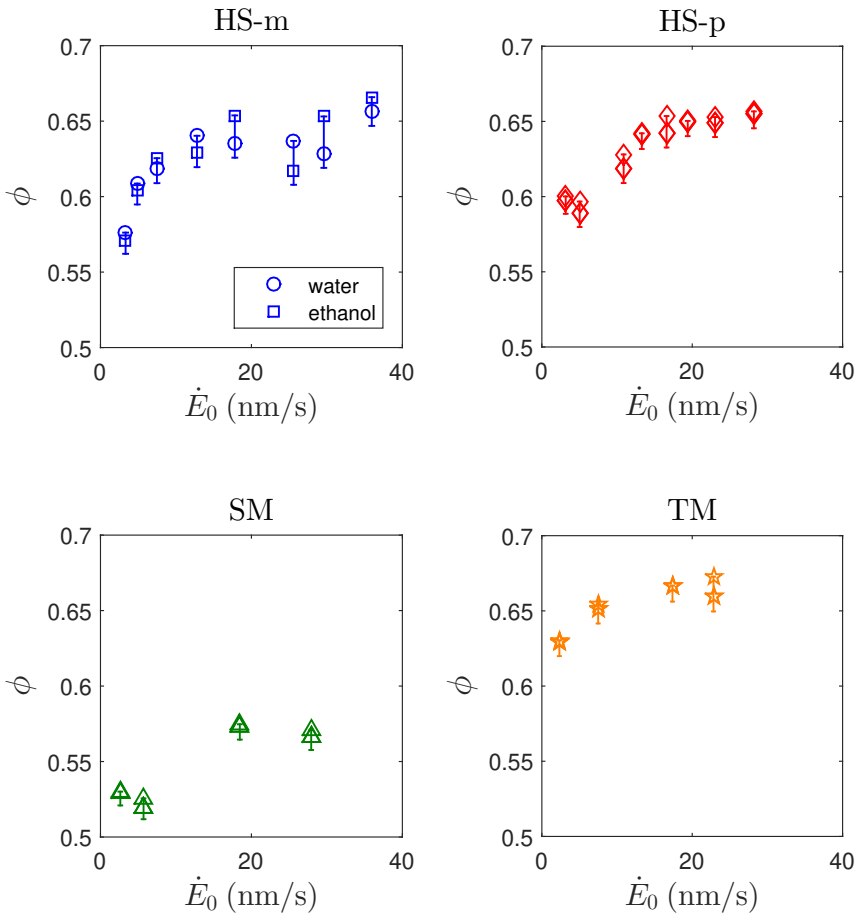

FIGURE 3.2: Packing fraction (ϕ) as a function of drying rate for all layers. The axes limits are the same on each plot for easier comparison of the packing fraction yielded by drying the different Ludox suspensions.

2 AFM measurements

2.1 Images

Figure 3.3 shows typical images obtained from the surfaces of the different drying experiments. Depending on the suspension type and the drying rate, some layers exhibit an hexagonal ordering of the particles.

- Layers made from HS-m suspension show an hexagonal surface pattern when dried at high drying rates; layers dried at lower drying rates have an amorphous structure.
- Layers dried from SM as well as from HS-p suspension do not have visible crystallinity at any drying rate.

- Layers dried from TM suspensions exhibit crystallinity at all drying rates. On the fast Fourier transform (FFT) for the TM layer shown on fig. 3.3, both first-order and second-order diffraction peaks are visible.

From the positions of the particle centers, I use two parameters to quantify the long-range order (in translation as well as in rotation) of the layers.

2.2 Translational order

The long-range translational order of the images can be characterized using the pair correlation function $g(r)$. This function represents the probability of finding a particle center at a distance r of a given particle, normalized by the probability for an ideal gas (*i.e.* for random non-correlated particle positions). Figure 3.4 shows $g(r)$ for all Ludox types at maximal (blue, top curves) and minimal (red, bottom curves) drying rates. TM layers, as well as fast-dried (RH = 10%) HS-m layers, have pair correlation functions exhibiting well-defined long range peaks, which are the signature of a long-range translational order. Conversely, $g(r)$ functions for slowly-dried (RH = 95%) HS-m layers, as well as for SM and HS-p layers, lack such long range peaks for r larger than two particle diameters: thus, no translational order exists at the surface of these layers.

2.3 Rotational order

Crystallinity at the drying surface can be further characterized using the bond angle order parameter ψ_6, defined by:

$$\psi_n = \left| \frac{1}{\mathrm{M}} \sum_{k=1}^{\mathrm{M}} \frac{1}{\mathrm{N}_k} \sum_{l=1}^{\mathrm{N}_k} \exp\left(i\, n\, \theta_{kl}\right) \right|, \tag{3.1}$$

where n is the number of nearest neighbors, M is the number of particles in the AFM image, N_k the number of nearest neighbors for particle k, and θ_{kl} is the angle between a fixed direction and the line joining particles k and l. For a hexagonal arrangement, as observed on our layers, $n = \mathrm{N}_k = 6$. ψ_6 is a measure of the orientational order of the particle arrangement. For an amorphous arrangement, $\psi_6 = 0$, while for an arrangement with sixfold symmetry (such as a perfect hexagonal lattice), $\psi_6 = 1$. Figure 3.5 gives ψ_6 as a function of the drying rate for each of the four Ludox types. For all SM and HS-p layers, $\psi_6 \simeq 0.05 \ll 1$, which suggests that the layers are amorphous. This is in agreement with the $g(r)$ profiles on these layers, which show no crystalline peaks. Conversely, $\psi_6 \simeq 0.47 \pm 0.03$ for TM layers, a value

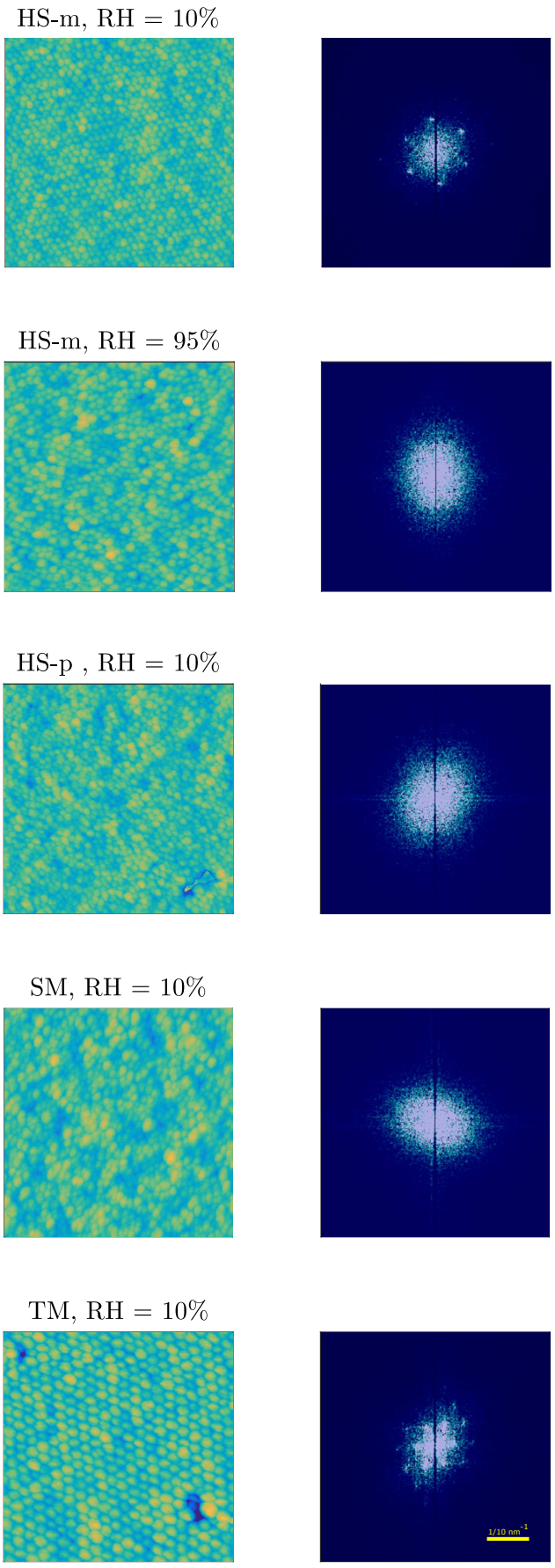

FIGURE 3.3: 500x500 nm^2 AFM images (left) and corresponding fast Fourier transforms (right) for representative layers.

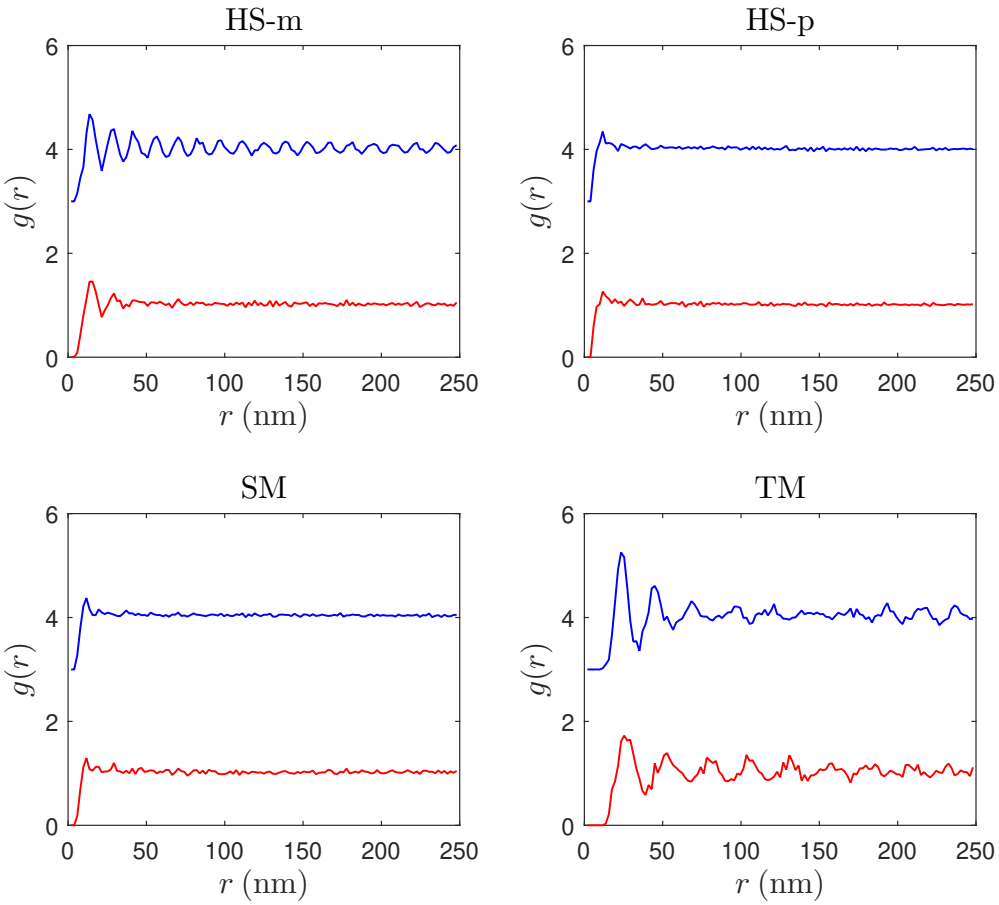

FIGURE 3.4: Pair correlation function $g(r)$ for all Ludox types, at the highest drying rate (blue, top curves) and at the lowest drying rate (red, bottom curves). For the sake of clarity, $g(r)$ was shifted upwards by three units for RH = 10%.

indicating of crystallinity. HS-m layers show two regimes, one with an amorphous structure ($\psi_6 \simeq 0.05$) at low evaporation rates ($\dot{E}_0 \leqslant \dot{E}_c = 10\,\mathrm{nm/s}$), and one with increasing crystallinity for $\dot{E}_0 > \dot{E}_c$, with $\psi_{6,max} = 0.38 \pm 0.07$ at the highest evaporation rate. Even for the most crystalline layers, the particle centers are not perfectly aligned with the vertices of a hexagonal lattice; hence, ψ_6 is always significantly lower than one.

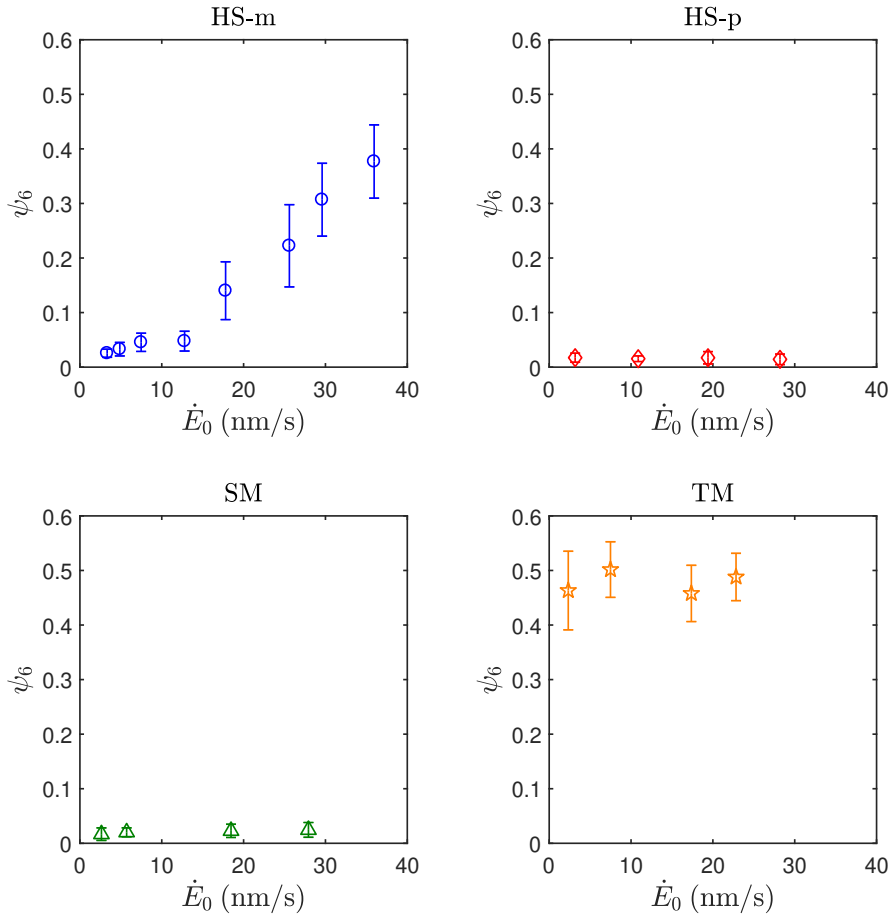

FIGURE 3.5: Bond orientation parameter ψ_6 for the four Ludox types as a function of evaporation rate.

2.4 Summary

Table 3.1 summarizes the effect of drying rate on surface structure and packing fraction for each Ludox suspension used. The main observations are as follows:

- Surface structure was crystalline for TM layers and fast-dried ($\dot{E}_0 > 10\,\mathrm{nm/s}$) HS-m layers; all other layers were amorphous;
- Packing fraction increases with higher $\dot{E}_0$ and larger particle size.

III Discussion

1 Role of aggregation

A striking feature of dry layers of HS-m is the transition from a disordered to an ordered system with *increasing* drying rate: the surface of faster-dried layers shows an

Suspension	Particle radius (nm)	Surface (low $\dot{E}_0$)	Surface (high $\dot{E}_0$)	ϕ (low $\dot{E}_0$)	ϕ (high $\dot{E}_0$)
SM	5.5	amorphous	amorphous	low	low
HS-m	8.1	amorphous	crystalline	medium	high
HS-p	8.8	amorphous	amorphous	medium	high
TM	14.0	crystalline	crystalline	high	high

TABLE 3.1: Summary of the influence of drying rate on surface structure and packing fraction. ϕ values were sorted as low ($\phi < 0.58$), medium ($0.58 < \phi < 0.63$) or high ($\phi > 0.63$).

hexagonal arrangement of the silica beads, while slowly-dried layers have an amorphous surface. Such an evolution is counterintuitive: slow evolution of a system generally favors order formation.

A natural parameter to explain this transition would be the Péclet number, defined as $Pe = h_0\dot{E}_0/D_0$, where h_0 is the height of the layer at the beginning of the drying, $\dot{E}_0$ the initial drying rate and D_0 the diffusion coefficient of the colloidal particles in the liquid phase (which can be expressed through the Stokes-Einstein relation). The Pe number is the ratio between the convection time of the particles, carried by the liquid flow through the drying layer, and their Brownian diffusion time. At high Pe (corresponding to high drying rates when h_0 is kept constant), the solid material forms layer by layer as the particles are convected to the surface, whereas at low Pe (low drying rates), diffusion keeps the layer homogeneous and the solid forms by uniform compaction of the particles. However, experiments realized in Piroird et al., 2016 showed that Pe was not the relevant control parameter for the transition. Slowly-dried, thicker (*i.e.* with higher h_0) layers were observed to be amorphous, despite having a higher Pe than fast-dried and thin layers, which were crystalline.

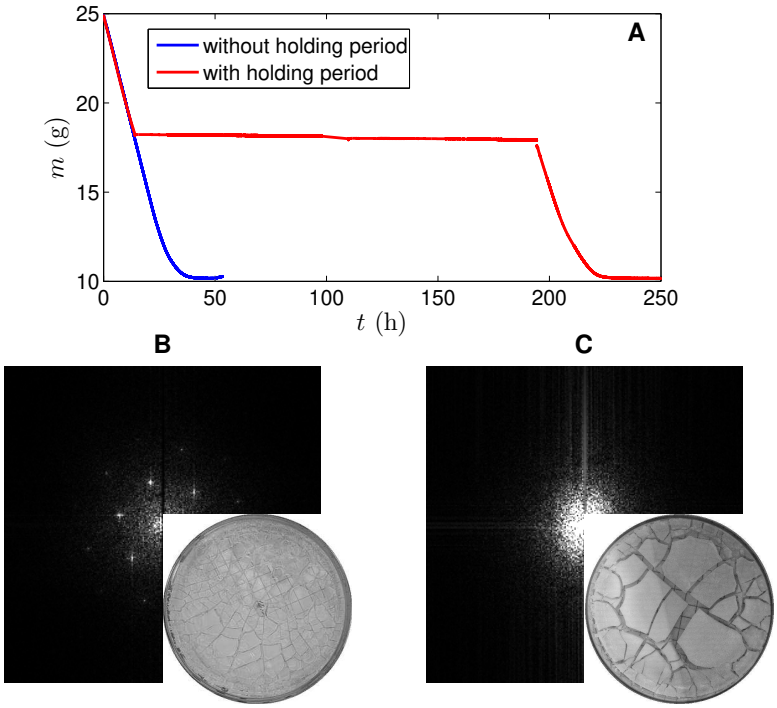

FIGURE 3.6: Influence of a holding period on the structure of the resulting dry layer. (A) Evolution of layer mass with time in a fast-drying experiment (RH = 10%), with (red) and without (blue) a holding period. The holding period lasts 180 h at a packing fraction $\phi = 0.335$ (corresponding layer mass $m = 18.2$ g). (B) Fourier spectrum of a typical topographical AFM image and crack pattern (insert) observed for a layer dried at RH = 10% without holding period. (C) Fourier spectrum of a typical topographical AFM image and crack pattern (insert) observed for a layer dried at RH = 10% with a 180 h holding period. In contrast to the layer with uninterrupted drying, the layer dried with a holding period shows an amorphous structure and larger morsels. Figure taken from Piroird et al., 2016.

This counterintuitive transition was explained by the formation of aggregates, as evidenced by holding period experiments. During a holding period experiment, a sample of suspension is dried at the highest evaporation rate, in order to make the suspension more concentrated. The drying is then interrupted for a prescribed time, while the suspension is still in a liquid state. Finally, the drying resumes at the original rate until completion. A fast-drying experiment yields a crystalline layer, yet a holding period experiment yields an amorphous one (see fig. 3.6). This suggests that the phenomenon responsible for the order-disorder transition is the formation of aggregates. When the suspension remains long enough in a concentrated liquid state, whether during a slow-drying experiment or during a holding period, aggregates form which preclude the crystallization of the silica beads.

In order to test this proposed mechanism for the transition, I performed a drying experiment with a holding period, using SAXS to determine the form factor P(q) of the suspension at the beginning and the end of the holding period. 25 g of HS-m suspension were dried at the highest evaporation rate ($\dot{E}_0 = 24.2\,\mathrm{nm/s}$, $RH_c = 10\%$) down to a mass $m = 19\,\mathrm{g}$. 1.5 g of this concentrated suspension were sampled, diluted, and imaged in SAXS, using the same dilution and measurement protocols as in chap. 2. The rest of the suspension was subjected to a holding period ($t = 168\,\mathrm{h}$); this aged suspension was then in turn diluted and imaged in SAXS. Figure 3.7 represents the form factor of the suspension, at the beginning of the holding period (solid blue line) and after the seven day holding period (red dashed line). The evolution of the diffracted intensity at low q is evidence of the apparition of larger particles in the suspension, that is, the formation of aggregates. This substantiates the scenario initially proposed in our first article.

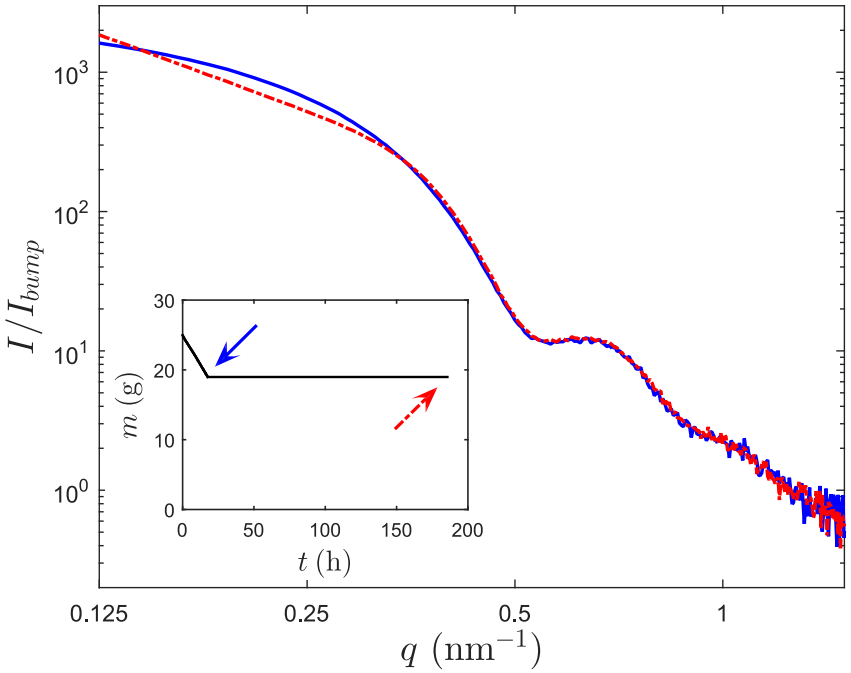

FIGURE 3.7: Evolution of SAXS signal with holding period. Insert: mass as a function of time during a holding period experiment. Samples of drying suspension were taken and diluted before (blue solid arrow) and after (red dashed arrow) a holding period. Main plot: diffracted intensities of the dilute suspensions, at the beginning of the holding period (blue solid line) and after the 7 days holding period (red dashed line). The evolution of the shape of the signal at low q (*i.e.* large scales in direct space) is evidence of the formation of aggregates.

2 Role of dispersity

The behavior of the suspensions in the absence of aggregation (*i.e.* at high drying rates) underlines the role of particle dispersity in the formation of a crystalline structure. At high drying rates ($\dot{E}_0 > 10\,nm/s$), TM and HS-m suspensions yield crystalline layers, as expected from their low polydispersity index (σ/R_m = 0.10 and 0.14 respectively) while SM and HS-p layers, with their higher polydispersity index (σ/R_m = 0.19 and 0.33), remain amorphous. Such a behavior is expected as sphere packings require low polydispersity ($\sigma/R_m < 0.15$) for crystallization to be possible.

3 Volume ordering

AFM measurements only image the surface of the layers, *i.e.* the top layer of particles. Thus, a natural question is how much the ordering of the surface extends into the bulk. A first possibility would be to probe bulk crystallinity by imaging the vertical fracture surfaces, either the natural ones (formed during the drying process) or artificial ones obtained by breaking the dry layers. Both approaches were tried, but the fracture surfaces proved to be too rough and no useful information could be obtained, neither via AFM nor via electron microscopy.

Porosity measurements, however, can yield some information about the volume ordering of the particles. For all Ludox batches, compacity increases with the drying rate. This observation also suggests that slow-drying favors aggregate formation in the liquid phase: as aggregates cannot be packed as densely as individual particles, slowly-dried suspensions yield more porous layers. The influence of drying rate on the compacity of the resulting layer is dependent on the suspension type. For both HS-m and HS-p suspensions, ϕ significantly increases with increasing $\dot{E}_0$. For TM suspensions, ϕ is relatively high ($\phi > 0.63$) at all drying rates whereas for SM suspensions, ϕ is low ($\phi < 0.58$) at all drying rates. This suggests than the suspension type, and especially the particle size, has a strong influence on suspension stability and gelling behavior: suspensions with smaller particles aggregate more easily and gel earlier (*i.e.* at higher ϕ) during the drying process. This can be related to the analysis of the drying process presented in chap. 5, which shows that the volume fraction of silica when the first cracks appear is larger with TM suspensions than with SM suspensions, with HS-m and HS-p layers cracking at intermediate volume fractions.

Finally, compacity measurements can shed light on bulk crystallization. Fast-dried layers from monodisperse and polydisperse HS have very different surface properties, as they are respectively crystalline and amorphous, but their compacity

is the same ($\phi = 0.66 \pm 0.01$). Thus, such a compacity does not prove that surface ordering extends into the bulk, despite being above the compacity of a random close packing ($\phi_{RCP} = 0.64$). The fact that $\phi > \phi_{RCP}$ even for an amorphous packing can be explained by measurement uncertainties or by the polydispersity of the suspensions, as a polydisperse sphere packing can have $\phi > 0.64$ even in the absence of crystallinity.

IV Conclusion

The effect of the drying rate on particle arrangement in the dry layers, which was shown in Piroird et al., 2016 to be mediated by the formation of aggregates, is dependent on particle size and polydispersity. In the volume of the layers, compacity is controlled by the formation of aggregates. This depends on the drying rate but also on the stability of the suspension, which increases with increasing particle size. At the surface of the layers, the formation of a crystalline arrangement is also controlled by the formation of aggregates, but it requires a relatively low polydispersity.

These results may be of interest in the design of processes requiring the autoassembly of colloidal particles into large-scale crystalline structures, for example for photonics and biotechnology applications. The effect of a holding period, and of the subsequent particle aggregation, on the mechanical (*e.g.* fracture) properties of the resulting layers could also be studied, as controlling crack formation during colloidal drying is an industrially relevant problem.

Chapter 4

Elastic properties

Porous media obtained by colloidal drying are ubiquitous in nature as well as industry. Modeling and controlling the mechanical properties of these media is critical to many technological applications. This chapter first reproduces an article (Lesaine et al., 2018) of which I am the first author, published in *Soft Matter* in 2018. It is concerned with the characterization of the elastic properties of the dry layers, using HS-m as the initial suspension. The measured elastic properties (bulk and shear moduli) are compared and contrasted with the predictions of several homogenization schemes (Mori-Tanaka and self-consistent) for porous media, as well as with Kendall's model for the Young's modulus of sphere packings with surface adhesion. An addendum to the original article then presents the data collected on layers prepared from the other Ludox suspensions.

I Abstract

Layers obtained by drying a colloidal dispersion of silica spheres are found to be a good benchmark to test the elastic behaviour of porous media, in the challenging case of high porosities and nano-sized microstructures. Classically used for these systems, Kendall's approach explicitly considers the effect of surface adhesive forces onto the contact area between the particles. This approach provides the Young's modulus using a single adjustable parameter (the adhesion energy) but provides no further information on the tensorial nature and possible anisotropy of elasticity. On the other hand, homogenization approaches (*e.g.* rule of mixtures, and Eshelby, Mori–Tanaka and self-consistent schemes), based on continuum mechanics and asymptotic analysis, provide the stiffness tensor from the knowledge of the porosity and the elastic constants of the beads. Herein, the self-consistent scheme accurately predicts both bulk and shear moduli, with no adjustable parameter, provided the porosity is less than 35%, for layers

composed of particles as small as 15 nm in diameter. Conversely, Kendall's approach is found to predict the Young's modulus over the full porosity range. Moreover, the adhesion energy in Kendall's model has to be adjusted to a value of the order of the fracture energy of the particle material. This suggests that sintering during drying leads to the formation of covalent siloxane bonds between the particles.

II Introduction

Porous materials formed by cohesive beads are commonly found in nature (sandstones, sedimentary rocks, opals, soils...) and in industry (ceramics, pharmaceutical pills, filter cakes, photonic materials, paintings...). Sintering between beads, whether resulting from evaporation, heat or compression, confers an overall cohesion and solid behavior to the material. For engineering purposes, it is of utmost importance to relate the mechanical properties at the macroscale to microscale behavior, whatever the constitutive relations of the components (elastic, plastic, viscoplastic...). This constitutes a broad field (Willis, 1987; Ponte Castaneda, 2004; Dormieux et al., 2006); this paper only addresses the linear elastic part.

When looking for the equivalent elasticity of a packing of cohesive particles, a first possibility is to exploit the analogy between scalar elasticity and scalar electricity (Jernot et al., 1982) and sketch the material as a network of resistances. Effective medium theory (Bruggeman, 1935; Landauer, 1952; Kirkpatrick, 1971) then permits, from the particle coordination number and the density probability function of contact resistance, to compute the effective resistance and subsequently the elastic modulus of the packed system. However, these two parameters are difficult to assess, and this approach fails to take into account the inherent tensorial nature of elasticity. Even in the simple case of an isotropic solid, two parameters (*e.g.* bulk and shear moduli) are necessary to fully describe the elastic behavior of the material. Therefore, it is more appropriate to use homogenization methods rigorously derived within the framework of continuum mechanics and multi-scale asymptotic analysis (Willis, 1987; Ponte Castaneda, 2004; Dormieux et al., 2006). Finally, when the particle size becomes submicrometric, adhesive surface forces are expected to become relevant. Kendall's approach explicitly takes these forces into account. Herein, it proves to be a relevant framework to cast the problem into. To

the best of our knowledge, only a few papers report quantitative comparisons between these theoretical approaches and experimental ones (see *e.g.* Kendall et al., 1987a; Ashkin et al., 1990; Shahidzadeh-Bonn et al., 2005 for past attempts).

The study herein proposes nanoporous materials obtained by drying a monodisperse aqueous colloidal suspension of nanometer-sized silica spheres (Ludox HS-40) as a benchmark medium to test models against. During drying, water evaporation brings the particles into contact and transforms the initially liquid dispersion into a hard, non-friable solid layer constituted of self-organized sintered particles (sec. III). Controlling the drying rate provides a simple way to modulate the porosity of the dried material (Piroird et al., 2016; Noirjean et al., 2017). Both bulk and shear elastic constants are measured by ultrasound methods. Since the goal of this paper is to bridge the continuum mechanics and soft matter communities (Goehring et al., 2015; Sibrant and Pauchard, 2016; Birk-Braun et al., 2017), we review the basic ingredients involved in classical homogenization schemes: the rule of mixtures and the Eshelby, Mori-Tanaka and self-consistent schemes (sec. IV), and in Kendall's approach (sec. V). Section VI compares the theoretical predictions with the experimental data and sec. VII discusses the results.

The self-consistent approach accurately predicts both the bulk and shear moduli with no adjustable parameters, as long as the porosity is sufficiently small (less than 35%). Conversely, Kendall's approach predicts the variations of the Young's modulus with porosity over the full range, provided that the adhesion energy is properly adjusted. The fitted value is found to be surprisingly high when compared to the values usually considered in this kind of problem (Goehring et al., 2013; Birk-Braun et al., 2017): It falls very close to the fracture energy, *i.e.* the energy required to break the covalent siloxane bonds, showing that drying colloidal suspensions enables the formation of strong covalent siloxane bonds between particles. This apparent discrepancy with the literature is discussed.

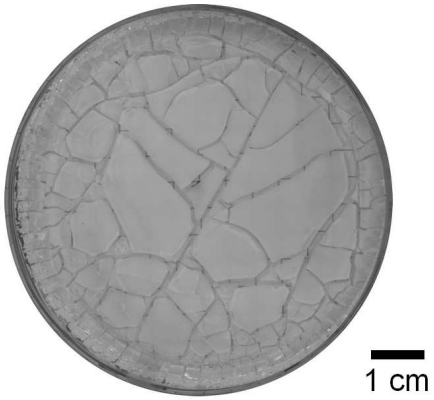

A

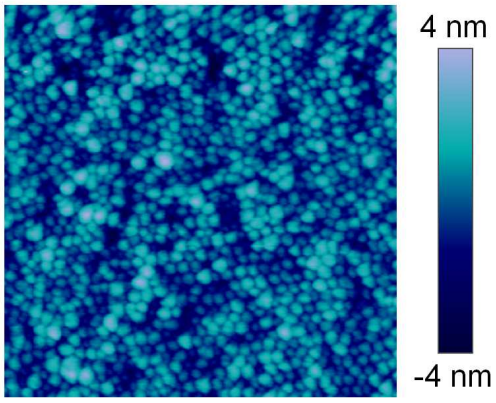

B

FIGURE 4.1: (A) Crack patterns of a dried colloidal layer. (B) Topographical AFM image of the top surface of the layer (scan size $500 \times 500\,\mathrm{nm}^2$). The sample pictured here was dried at RH = 50%.

III Experimental methods

1 Sample preparation

The study herein is a follow-up of a previous study (Piroird et al., 2016). It uses Ludox HS-40, an aqueous dispersion (initial mass concentration $\phi_m \sim 40\%$) of silica spheres, commonly used as a model colloidal suspension (Giuseppe et al., 2012; Boulogne et al., 2015; Cabane et al., 2016; Sibrant and Pauchard, 2016; Birk-Braun et al., 2017). According to SAXS measurements of the form factor, silica beads have an average diameter $a = 16.2\,\mathrm{nm}$ with a relative polydispersity $\sigma = 14\%$. In all the study the

same batch (number STBF8427V) of Ludox was used. The porous material is obtained from 25 g of suspension poured into a Petri dish (3.5 cm radius), which corresponds to an initial liquid height of 5 mm. The system is then left to dry at room temperature (T = 25 ± 2 °C) in an enclosure with constant relative humidity (RH) until evaporation ceases. This process typically lasts between 2 and 14 days depending on the RH value. As water evaporates, the beads come in contact, sinter and form a porous solid material of final thickness $h \sim 2$ mm. These layers are hard and not friable.

Some desiccation cracks (Goehring et al., 2015) appear during this drying process (fig. 4.1A). These fractures are due to the shrinkage of the layer induced by evaporation and impeded by the substrate (*i.e.* bottom of the Petri dish) (Chekchaki and Lazarus, 2013). These cracks divide the layer into smaller morsels (Lazarus and Pauchard, 2011; Lazarus, 2017). The size of the morsels increases with higher RH, that is slower drying.

2 Ultrasonic techniques

Ultrasound velocity measurements provide the elastic moduli and Poisson's ratio of the dried colloidal layers. As the morsels are thin (~ 2 mm), this requires special signal processing techniques (Barlet et al., 2015) in calculating longitudinal (c_L) and transverse (c_T) wave speeds.

A single transducer is coupled to one face of the sample, with honey as the viscous couplant for pulse transmission. The transducer coupled with a pulse generator (Panametrics 5800) either provides a compression (Olympus Panametrics-NDT M116) or shear (Olympus Panametrics-NDT V222) pulse to the sample, the frequency of the pulse is 20 MHz in both cases. The ultrasonic system provides a controlled short pulse so as to control the wave introduced into the sample: ~ 0.4 μs for both compressional and shear pulses.

The emitted pulse travels across the specimen, bouncing back and forth between the two opposite faces. Its successive passings at the specimen-transducer interface are detected at 500 MHz using a Tektronix TDS3054B oscilloscope. Figure 4.2 displays the tension captured by the oscilloscope as a function of time. The thickness of the specimen is measured using a digital caliper with an accuracy of 0.01 mm.

In our experiment, the samples are thin (~ 2 mm): the typical time between two successive echoes is ~ 1 μs (resp. ~ 1.6 μs) for compressional (resp. shear) pulses. In general, associating a single discrete time to the

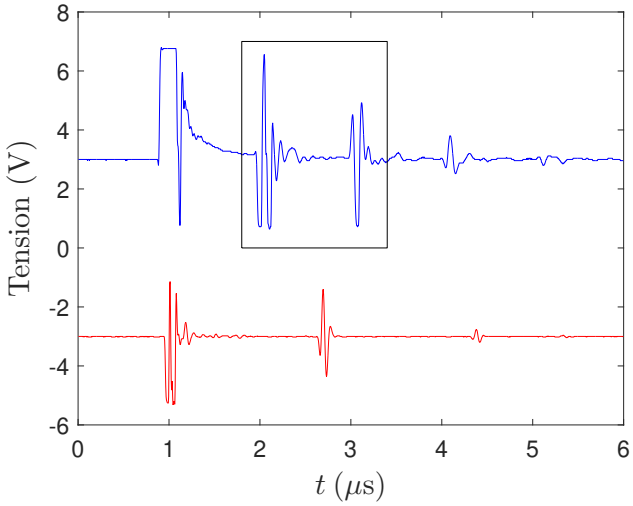

FIGURE 4.2: Time evolution of the signal received at the transducer for compression waves (blue) and shear waves (bottom). The material probed here is a sample dried at RH = 50% and the specimen thickness is 2.07 ± 0.03 mm. For the sake of clarity, the signals are shifted by 3 V and -3 V respectively. The black box delimits the signal represented on fig. 4.3.

pulse arrival on the transducer proved difficult. This difficulty was overcome by the following processing scheme:

- For each pulse, the arrival times of three successive extrema of the signal are determined.
- For each series of matching extrema (*i.e.* extrema of the same color on fig. 4.3), the time delay between two matching extrema gives an estimate of the propagation time of the pulse through the sample.
- These estimates are evaluated between each pulse for each series of matching extrema, and subsequently averaged (fig. 4.4).

Bulk modulus (k) and shear modulus (μ) of the macroscopic sample can then be expressed as a function of ρ, c_T and c_L:

$$\mu = \rho c_\mathrm{T}^2 \quad \text{and} \quad k = \rho c_\mathrm{L}^2 - \frac{4}{3}\mu \tag{4.1}$$

In order to validate this measurement procedure, we applied it to a block (5x5x25 mm^3) of pure silica glass (Corning 7980 standard grade). Measurements of the sound velocities were repeated on the two sets of opposite faces. The density $\rho_{s,Corning} = 2.20 \pm 0.02\,\mathrm{g/cm^3}$ provided by the

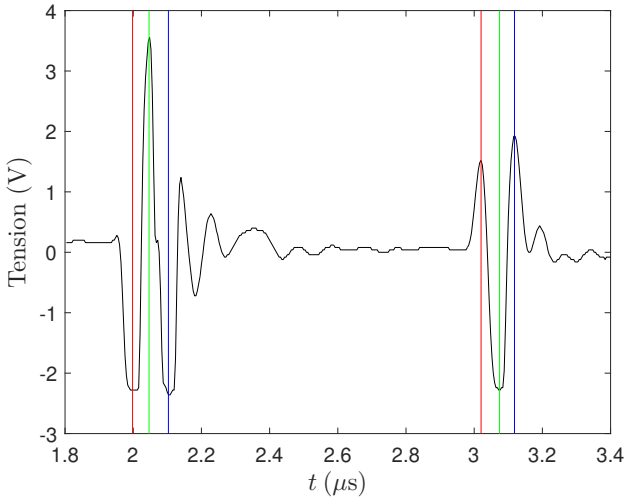

FIGURE 4.3: Two successive reflected pulses for the compression wave represented on fig. 4.2. Arrival times of matching extrema are indicated by vertical lines of identical color.

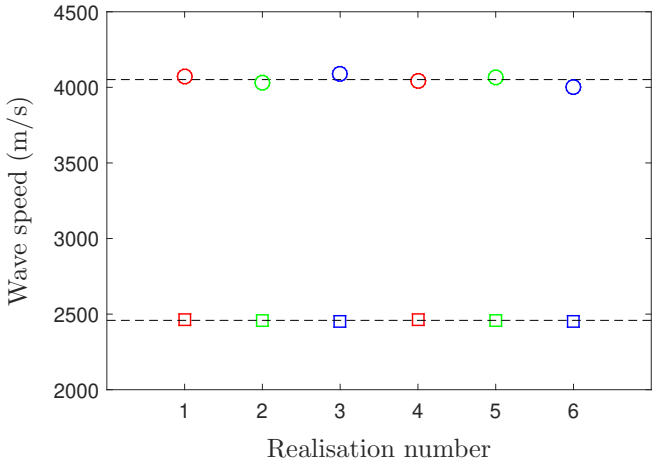

FIGURE 4.4: Time delay over traveled distance for each pair of matching extrema, between pulses 1 and 2 and pulses 2 and 3, for compression waves (circles) and shear waves (squares). The black dotted lines represents the average of all estimated speeds for a given type of waves.

	k_s (GPa)	μ_s (GPa)
Spec.	35.4	31.4
Meas. 1	36.1±0.3	31.0±0.1
Meas. 2	33.9±0.3	31.4±0.1

TABLE 4.1: Elastic constants measured by ultrasounds on fused silica standard grade, Corning code 7980 (± provide the error bars for one standard deviation)

supplier was used. The corresponding values of k_s and μ_s are presented in tab. 4.1 together with the values provided by the supplier (Corning, 2003). They are in good agreement with each other. This validates our characterization methods.

3 Porosity measurements

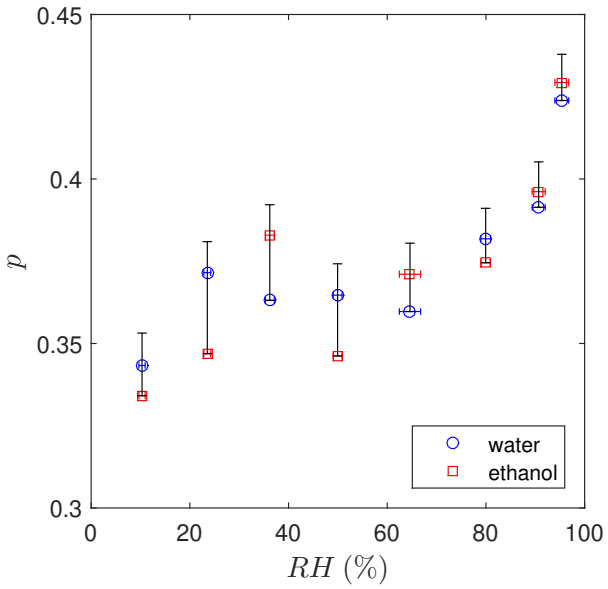

FIGURE 4.5: Porosity (p) as a function of relative humidity (RH), measured by hydrostatic weighing in water (blue circles) and in ethanol (red squares). In the rest of the article, p is taken as the average of these two values. The vertical error bars account for the possible presence of water trapped in the dry samples (tab. 4.2) (Iler, 1979; Piroird et al., 2016). The horizontal error bars represent the standard deviation on RH during the drying experiments.

The porosity (p) of a material is defined as the ratio of pore volume over total volume: $p = V_p/V_T = 1 - V_s/V_T$, where V_p is the pore volume, V_s the volume of the solid phase, and $V_T = V_s + V_p$ is the total volume of the

sample. The porosity of a material can be expressed from its density (ρ) and the density of the solid phase (ρ_s) as follows: $p = 1 - \rho/\rho_s$. Notice that the procedure described below has several advantages: it is non-destructive and provides the total porosity (sum of open and closed porosity).

The density of the silica particles is estimated ($\rho_s = 2.26 \pm 0.02\,\mathrm{g/cm^3}$) through the dilution method presented in Piroird et al., 2016, by measuring the densities of several suspensions of particles with varying concentrations.

The density of the porous layer is obtained from its dry mass (m_{dry}) and its total volume ($\mathrm{V_T}$, sum of the volume of the solid phase and the volume of both open and closed pores). First, the sample is heated to 200 °C for 3 hours in order to remove all water at the surface of the nanoparticles, and its dry mass (m_{dry}) is measured. The sample is then soaked in a solvent (water or ethanol) in order to fill the open pores. The wet sample is weighted in air (mass (m_{wet})) and in the fluid (apparent mass ($\widetilde{m}_{wet}$)) and the total volume ($\mathrm{V_T}$) of the sample is inferred using Archimedes' principle: $\mathrm{V_T} = (m_{wet} - \widetilde{m}_{wet})/\rho_f$, where ρ_f is the fluid density.

4 Properties at the bead scale

Due to the nanometric size of the beads, their density (ρ_s) and bulk (k_s) and shear (μ_s) elastic moduli (or equivalently Young's modulus (E_s) and Poisson's ratio (ν_s)) cannot be directly measured. Thus, the bead properties are assumed to be equivalent to the bulk properties of pure silica. Specifically, the bulk and shear moduli measured on pure silica glass (see sec. 2) were used to describe the bead properties: $k_s = 35\,\mathrm{GPa}$, $\mu_s = 31.2\,\mathrm{GPa}$. In order to scale up the properties of the beads at the macroscale, some knowledge of the particle arrangement at the microscale is necessary. Imaging the top of the morsels via an Atomic Force Microscope (AFM) provides the structure of the particle packing. Figure 4.1B gives an example of the particle arrangement for RH = 50%. This image shows that the arrangement is on average homogeneous and isotropic along the surface, at larger scales. Henceforth, it is assumed that it remains true along the third direction. The agreement between the experiments and the models (sec. VI) will validate this hypothesis, *a posteriori*.

5 Sample properties at the macroscopic scale

In the experiments herein, the prescribed constant relative humidity RH in the enclosure is varied between 10% and 95%, monitored within 3%. As was evidenced in our previous study (Piroird et al., 2016), particle aggregation occurs in slowly-dried samples and precludes the formation of a ordered, compact dry layer. Thus, drying the suspension with RH between 10% and 95% provides dried solid layers with increasing porosity, p, ranging between 0.34 and 0.45, respectively. A larger range of porosities cannot be obtained without additional expensive heat treatments (Moro, 2013). Moreover, heat treatments may change the physical properties of the system (*e.g.* by inducing grain growth). Figure 4.5 depicts the porosity as a function of RH, and tab. 4.2 presents the corresponding values.

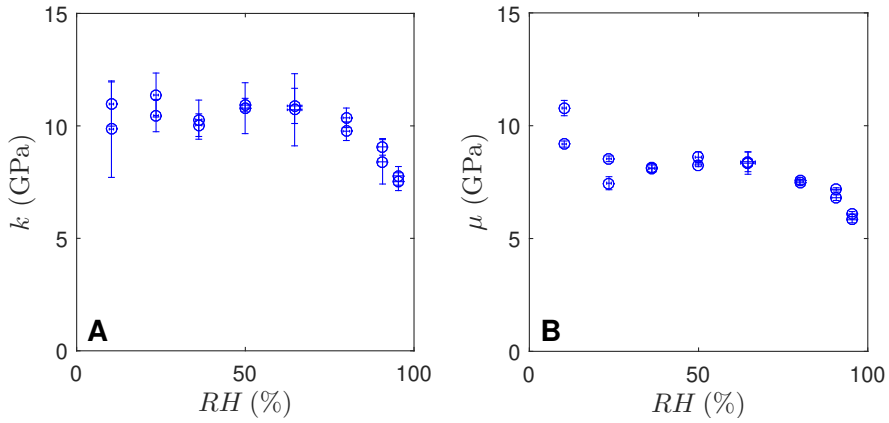

FIGURE 4.6: Bulk modulus (k) and shear modulus (μ) as a function of relative humidity (RH). Error bars correspond to standard deviation. For each drying rate, the measurements were repeated on two morsels.

Using the ultrasonic techniques described in sec. 2, the elastic constants of the dried layers were obtained by averaging the values measured with the transducers applied once at the top and once at the bottom of the sample Also, as the resulting dried layers contain multiple fractured pieces (fig. 4.1A), the measurements were conducted on two different morsels for each drying RH.

Figures 4.6A and 4.6B present k and μ as a function of the RH value for two morsels, and tab. 4.3 numerates the mean values. For humidities greater than $\sim$ 30%, k and μ are nearly the same in the two morsels; this highlights the homogeneity of layers dried under high humidity. At low humidities (*i.e.* RH $<$ 30%, high evaporation rates), inhomogeneities arise,

and thus, k and μ differ somewhat in the two morsels. The observation of a drying front crossing the layer during drying for RH = 15 and 20% suggests these low RH samples undergo directional horizontal drying. This leads to variations in the mechanical properties of these samples.

IV Homogenization in linear elasticity

Since the diameter, a, of the colloidal particles is several decades smaller than the thickness, h, of the layer ($a/h \sim 10^{-8}/10^{-3} \sim 10^{-5}$), one can define a Representative Elementary Volume (REV) of typical size ℓ such that $a \ll \ell \ll h$ (*i.e.* separation of length scales hypothesis). The scaling up of the elastic properties from the scale of the beads to the one of the layer is thus achievable by homogenization approaches (Willis, 1987; Ponte Castaneda, 2004; Dormieux et al., 2006) derived in the framework of continuum mechanics, in line with the seminal works of Eshelby (Eshelby, 1957), Hill (Hill, 1965), Budinsky (Budiansky, 1965) and Mori-Tanaka (Mori and Tanaka, 1973). This section summarizes the underlying hypotheses and the main results of these approaches.

This paper approaches the problem as follows: the elastic behavior is first defined at the scale of the particles (sec. 1). Then, the Representative Elementary Volume (sec. 2) is introduced to provide a gateway between the micro- and macro- scales. The scaling up involves the resolution of the linear elasticity problem on the REV (sec. 3). This problem is too complex to be solved analytically, and approximate results are instead invoked. Section 4 summarizes the most commonly used rule of mixtures. As will be seen in sec. VI, this simple rule does not provide an accurate estimate of the elastic properties of the porous material.

The end of the section reviews Eshelby's (sec. 5.1) and Mori-Tanaka's approximations (sec. 5.2) as they are prerequisites for the self-consistent scheme (sec. 6). A summary of the different models is given in sec. 7.

1 Microscale

For any linear elastic material, the relation between the local strain $\boldsymbol{\varepsilon}$ and stress $\boldsymbol{\sigma}$ tensors can be written as:

$$\boldsymbol{\sigma}(\boldsymbol{x}) = \mathbb{C}_s : \boldsymbol{\varepsilon}(\boldsymbol{x}) \tag{4.2}$$

where $\mathbb{C}_s$ is a proportionality constant expressing the elastic properties of the solid.

In the case of an isotropic material, $\mathbb{C}_s$ reduces to:

$$\mathbb{C}_s = 3k_s\mathbb{J} + 2\mu_s\mathbb{K} \tag{4.3}$$

with $\mathbb{J}$ and $\mathbb{K}$ respectively the spherical and deviatoric parts of the fourth-order symmetric identity tensor $\mathbb{I}$, given by:

$$\mathbb{J} = \frac{1}{3}\,\mathrm{Id} \otimes \mathrm{Id} \quad \text{and} \quad \mathbb{K} = \mathbb{I} - \mathbb{J} \tag{4.4}$$

with Id the second-order identity tensor. This formulation presents the advantage of being compact, and it decouples the elastic properties into bulk k_s and shear μ_s contributions.

Notice combining the previous three equations equates to the more commonly used relation:

$$\boldsymbol{\sigma} = k_s(\mathrm{tr}\,\boldsymbol{\varepsilon})\,\mathrm{Id} + 2\mu_s\boldsymbol{e}$$

where $\boldsymbol{e} \equiv \boldsymbol{\varepsilon} - \frac{1}{3}(\mathrm{tr}\,\boldsymbol{\varepsilon})\,\mathrm{Id}$ is the deviatoric part of $\boldsymbol{\varepsilon}$. The above equations can be inverted, such that the local strain ($\boldsymbol{\varepsilon}$) is a function of the stress ($\boldsymbol{\sigma}$), and is written as follows:

$$\boldsymbol{\varepsilon} = \frac{1+\nu_s}{\mathrm{E}_s}\boldsymbol{\sigma} - \frac{\nu_s}{\mathrm{E}_s}(\mathrm{tr}\,\boldsymbol{\sigma})\,\mathrm{Id}$$

where the following relations between k_s, μ_s, the Young's modulus (E_s), and the Poisson' ratio (ν_s) are invoked:

$$k_s = \frac{\mathrm{E}_s}{3(1-2\nu_s)} \quad \text{and} \quad \mu_s = \frac{\mathrm{E}_s}{2(1+\nu_s)} \tag{4.5}$$

At the microscale, the system can be described as a composite material made of silica (stiffness $\mathbb{C}_s$) and empty pores (stiffness $\mathbb{C}_p$). In this instance, describing the elastic properties at the microscale requires a local fourth-order stiffness tensor: $\mathbb{C}^{\mathrm{loc}}(\boldsymbol{x})$ where $\mathbb{C}^{\mathrm{loc}}(\boldsymbol{x}) = \mathbb{C}_s$ corresponds to the beads and $\mathbb{C}^{\mathrm{loc}}(\boldsymbol{x}) = \mathbb{C}_p$ corresponds to the pores, such that:

$$\sigma(\boldsymbol{x}) = \mathbb{C}^{\mathrm{loc}}(\boldsymbol{x}) : \boldsymbol{\varepsilon}(\boldsymbol{x}), \quad \forall \boldsymbol{x} \in \mathrm{REV} \tag{4.6}$$

Note, the stiffness of the empty pores is ideally zero. Yet in order to complete the calculations, it is necessary to assume a finite elasticity tensor for the pores. The final solution to the problem then corresponds to the limits $k_p/k_s \to 0$ and $\mu_p/\mu_s \to 0$, where k_p and μ_p denote the bulk and shear modulus of the pores (Dormieux et al., 2006). Henceforth, the results are presented in this limit.

2 The Representative Elementary Volume as a gateway between the micro- and macro- scales

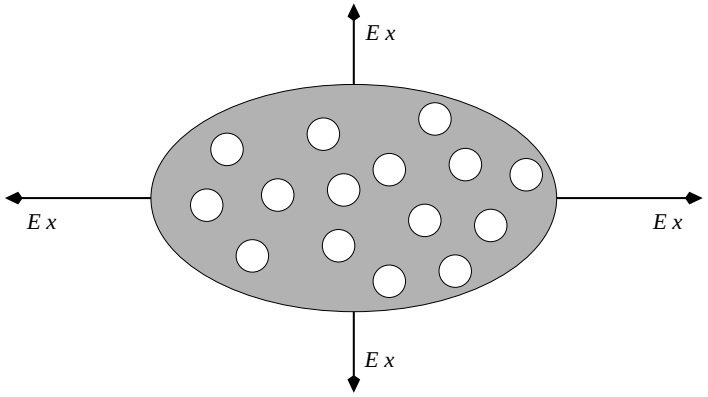

FIGURE 4.7: Representative Elementary Volume (REV) corresponding to a homogeneous matrix with spherical pores submitted to displacement $\mathbf{E}\boldsymbol{x}$ along its boundary, with $\mathbf{E}$ the strain tensor and $\boldsymbol{x}$ the position vector.

A classical way to proceed (Ponte Castaneda, 2004; Dormieux et al., 2006) is to isolate a Representative Elementary Volume (REV) and to prescribe some given displacement $\boldsymbol{u}$ at its boundary: $\boldsymbol{u} = \mathbf{E}.\boldsymbol{x}$, where $\boldsymbol{x}$ corresponds to the position vector (fig. 4.7). The second-order strain tensor $\mathbf{E}$ corresponds to the macroscopic given strain tensor, which is assumed to be constant along the boundary. Using Gauss's divergence theorem, one can demonstrate that:

$$\mathbf{E} = \langle \boldsymbol{\varepsilon}(\boldsymbol{x}) \rangle \tag{4.7}$$

where $\langle . \rangle \equiv \frac{1}{V} \int_{REV} . \, dV$ denotes the spatial average over the REV. The macroscopic stress $\boldsymbol{\Sigma}$ is then defined by its mean value:

$$\boldsymbol{\Sigma} \equiv \langle \boldsymbol{\sigma}(\boldsymbol{x}) \rangle \tag{4.8}$$

in coherence with the Hill-Mandel's lemma (Hill, 1967; Mandel, 1972).

At the macroscale, the porous material behaves as a linear elastic solid: thus, there is an effective stiffness tensor $\mathbb{C}$ such that

$$\boldsymbol{\Sigma} = \mathbb{C} : \mathbf{E} \tag{4.9}$$

If the microstructure arrangement is isotropic (*i.e.* there is no preferential orientation in the way the beads are packed), equivalent bulk (k) and shear (μ) moduli can be defined by:

$$\mathbb{C} = 3k\mathbb{J} + 2\mu\mathbb{K} \tag{4.10}$$

The aim of homogenization is to derive the effective tensor $\mathbb{C}$ knowing $\mathbb{C}_s$ and the microstructure arrangement. If isotropy is valid at all scales (the material components and their arrangement are isotropic), this is equivalent to look for the relations between (k, μ) and (k_s, μ_s).

3 The strain concentration tensor, $\mathbb{A}$

The local strain in the material $\boldsymbol{\varepsilon}(\boldsymbol{x})$ represents a solution of the problem of linear elasticity defined on the REV, hence it linearly depends on the macroscopic strain ($\mathbf{E}$) prescribed at the boundary of the REV. In other words, there exists a fourth-order local tensor $\mathbb{A}$, called the localisation or strain concentration tensor, such that:

$$\boldsymbol{\varepsilon}(\boldsymbol{x}) = \mathbb{A}(\boldsymbol{x}) : \mathbf{E}, \quad \forall \boldsymbol{x} \in \text{REV} \tag{4.11}$$

Plugging this last relation into eq. 4.6, taking its mean value, implementing the definition of $\boldsymbol{\Sigma}$ (*i.e.* eq. 4.8), and linking the result with the macroscopic constitutive relation (eq. 4.9) leads to:

$$\mathbb{C} = \langle \mathbb{C}^{\text{loc}}(\boldsymbol{x}) : \mathbb{A}(\boldsymbol{x}) \rangle \tag{4.12}$$

Thus to obtain $\mathbb{C}$, it is necessary to determine $\mathbb{A}$, which requires solving the elasticity problem for a REV composed of a beads assembly. This could, *a priori*, be done using computationally expensive numerical schemes. Alternatively, approximate solutions may be used. In what follows, three different estimations of $\mathbb{C}$ are provided: the upper Voigt bound and the Eshelby and Mori-Tanaka estimations as prerequisites for the self-consistent approximation.

4 Voigt's upper bound (Voigt, 1889): the rule of mixtures

A first possible approximation is to take $\mathbb{A}(x) = \mathbb{I}$ that is $\boldsymbol{\varepsilon}(x) = \mathbf{E}$ in all the REV, even in the pores. Then,

$$\mathbb{C} = (1-p)\mathbb{C}_s \tag{4.13}$$

This approximation neglects the effect of the pores on the strain distribution. It corresponds to a material behavior in which the pores deform as if they were made of the same homogeneous material as the solid phase, hence this estimation overestimates stiffness. One can rigorously demonstrate that it is an upper bound for the stiffness - the Voigt bound (Voigt, 1889).

For an isotropic material, eq. 4.13 is equivalent to:

$$\begin{aligned} k/k_s &= 1-p \\ \mu/\mu_s &= 1-p \end{aligned} \tag{4.14}$$

5 Pores embedded in a matrix

Another possible approach is to consider that the packing of beads is equivalent to an homogeneous solid matrix of elasticity $\mathbb{C}_s$, containing a repartition of spherical pores with the same porosity p (fig. 4.7).

5.1 Weak porosity: Eshelby's approximation (Eshelby, 1957)

When the porosity is weak ($p \ll 1$), the interactions between the pores can be neglected. Then $\mathbb{A}$ can be obtained from the analytical solution of the classical problem of Eshelby: an infinite elastic matrix of stiffness $\mathbb{C}_s$ containing a single spherical inclusion of stiffness $\mathbb{C}_p$. It is then possible to show that:

$$\begin{aligned} k/k_s &= 1 - \frac{p}{1-\alpha_s} \\ \mu/\mu_s &= 1 - \frac{p}{1-\beta_s} \end{aligned} \tag{4.15}$$

where the expressions of α_s and β_s as a function of k_s and μ_s are given by:

$$\alpha_s = \frac{1}{1+\frac{4\mu_s}{3k_s}} \quad \text{and} \quad \beta_s = \frac{6(1+2\frac{\mu_s}{k_s})}{5(3+4\frac{\mu_s}{k_s})} \tag{4.16}$$

It is noteworthy that α_s and β_s depend on k_s and μ_s only through

$$\mu_s/k_s = \frac{3(1-2\nu_s)}{2(1+\nu_s)} \tag{4.17}$$

(see eq. 4.5), hence only on the dimensionless Poisson's ratio ν_s.

5.2 High porosity: Mori-Tanaka's scheme (Mori and Tanaka, 1973)

For interacting pores, the Eshelby approach is not sufficient: a higher-order approximation is necessary. In this case, the Mori-Tanaka scheme is relevant. In this scheme, a single pore is isolated as an Eshelby problem, and a new boundary condition, $\boldsymbol{u} = \mathbf{E}_0.\boldsymbol{x}$, is adopted at infinity by choosing an auxiliary strain tensor $\mathbf{E}_0$ which takes into account the interactions between the pores.

The detailed calculations are quite complex (Dormieux et al., 2006) and eventually lead to the following equations for k and μ:

$$\begin{aligned} \frac{k}{k_s} &= \frac{1-p}{(1-p)+\frac{p}{1-\alpha_s}} \\ \frac{\mu}{\mu_s} &= \frac{1-p}{(1-p)+\frac{p}{1-\beta_s}} \end{aligned} \tag{4.18}$$

with α_s and β_s given by eq. 4.16, so that the equations explicitly yield $\frac{k}{k_s}$ and $\frac{\mu}{\mu_s}$ as a function of p, knowing k_s/μ_s, or equivalently, ν_s.

Notice that Eshelby's approximation (eq. 4.15) corresponds to the first order asymptotic expansion of the Mori-Tanaka scheme (eq. 4.18) with respect to $p \ll 1$.

6 Self-consistent approximation (Hill, 1965)

The Eshelby and Mori-Tanaka schemes assume a particular material geometry, in which individual, separate pores are surrounded by a solid matrix. But in the case of a sphere packing, pores are interconnected and percolate through the medium; thus, no surrounding matrix can be identified. Using a self-consistent scheme, which considers an Eshelby inclusion (solid or pore) in an equivalent homogenized medium of stiffness $\mathbb{C}$, seems preferable. The approach used in solving this problem then invokes the one used for the Mori-Tanaka scheme, applied on the equivalent material instead of

the solid phase. Again the derivations are quite complex (Dormieux et al., 2006) and only the final result is presented:

$$\begin{aligned} \frac{k}{k_s} &= \frac{1-p}{1+\left(\frac{k_s}{k}-1\right)\alpha} \\ \frac{\mu}{\mu_s} &= \frac{1-p}{1+\left(\frac{\mu_s}{\mu}-1\right)\beta} \end{aligned} \tag{4.19}$$

with $\alpha = 1/(1+\frac{4\mu}{3k})$ and $\beta = 6(1+2\frac{\mu}{k})/5(3+4\frac{\mu}{k})$ as in eq. 4.16. Equation 4.19 corresponds to two nonlinear and coupled implicit equations on k and μ, which can be solved numerically, for instance using Matlab.

7 Summary

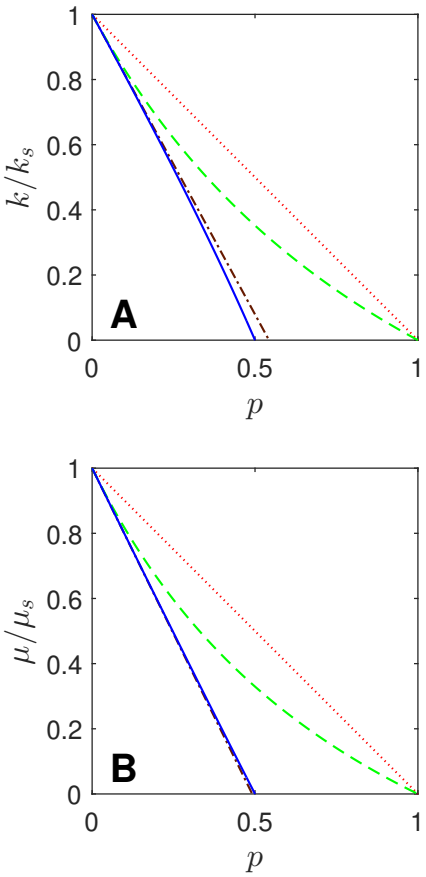

FIGURE 4.8: Predictions of the different schemes for $\nu_s = 0.16$ (pure silica): rule of mixtures (red dotted line), Eshelby's approximation (brown dash-dot line), Mori-Tanaka scheme (green dashed line) and self-consistent scheme (blue solid line).

Figure 4.8 compares the predictions of the above models for a solid phase made of silica ($\nu_s = 0.16$). As was expected, the rule of mixtures gives an upper bound, and is thus larger than the other predictions. All models predict a decrease in the effective stiffness with increasing porosity. Moreover, for a solid with negligible porosity ($p \sim 0$), all models predict moduli equivalent to the bulk parameters (*i.e.* $k = k_s$ and $\mu = \mu_s$).

One striking feature is that Eshelby's approximation and the self-consistent scheme yield nearly the same values. This is linked to the specific value of ν_s used here. In the general case, the Eshelby's approximation and the self-consistent scheme give different predictions. Moreover, the Eshelby's approximation assumes non-interacting pores and thus should not be used on materials with porosities greater than a few percent. Thus the Eshelby's model will not be further considered in this paper.

The Mori-Tanaka scheme corresponds to a solid matrix containing non-connected pores. Such a system retains some stiffness even in the vicinity of $p \to 1$, so that the Mori-Tanaka scheme predicts positive values of the moduli for $0 \leqslant p < 1$. On the contrary, the self-consistent scheme predicts that the stiffness vanishes for $p \sim 0.5$. Mathematically, it is linked to the fact that the phases invert their roles at $p = 0.5$. Physically, this level of porosity is generally considered to correspond to the percolation threshold of pores (Brisard et al., 2010a).

V Kendall's type models

The above homogenization schemes do not capture the effects of possible surface forces; these are expected to become significant for sub-micrometer particles, as is the case here. It then becomes interesting to make use of Kendall's approach (Kendall et al., 1987b; Kendall, 2001). This approach is based on the idea that the beads (of diameter a) are pressed together due to attractive surface forces, characterized by an interfacial energy, W. This energy induces a compressive force between two beads in contact (Johnson et al., 1971):

$$\mathrm{F}_{adh} = \frac{3\pi}{2}\mathrm{W}a \tag{4.20}$$

Using Hertz's theory on the contact of elastic spheres, Kendall relates the

shrinkage displacement (δ_{adh}) between the centers of the beads to the adhesion force (F_{adh}):

$$\delta_{adh} = \left(\frac{3}{32} \frac{1-\nu_s^2}{E_s} \frac{F_{adh}}{a^{1/2}} \right)^{2/3} \tag{4.21}$$

Now, adding a perturbing force $f \ll F_{adh}$ to the adhesion force gives $F = F_{adh} + f$. To the first order, the perturbing force induces an additional displacement δ:

$$f = k_n \delta \quad \text{with} \quad k_n = \left(\frac{9}{16} \frac{\pi W E_s^2 a^2}{(1-\nu_s^2)^2} \right)^{1/3} \tag{4.22}$$

The next step is to infer, from the stiffness of a single contact, the Young's modulus of the overall packing. Kendall first considers a simple cubic (sc) packing such that:

$$E_{sc} = \frac{f/a^2}{\delta/a} = \frac{k_n}{a} \tag{4.23}$$

and the porosity of this packing is $p = 1 - \pi/6 \simeq 0.4764$. Along the same lines, he then computes both the Young's modulus and the porosity for a variety of packing geometries (cubic-tetrahedral, tetragonal-sphenoidal and hexagonal) and E as a function of p fits well a $(1-p)^4$ dependence on p:

$$E = A(1-\nu_s^2)^{-2/3}(1-p)^4 \left(\frac{WE_s^2}{a} \right)^{1/3} \tag{4.24}$$

where $A \simeq 16.1$ is a fitting parameter (Kendall et al., 1987b). Later, Thornton (Thornton, 1993) provided some modifications of this approach: he used the theory from Johnson, Kendall and Roberts (Johnson et al., 1971) (rather than Hertz theory) to estimate contact stiffness, and he considered a body centered orthorombic array (rather than simple cubic) as a reference packing. These two modifications reduce A by a factor of two. In a nutshell, A varies from 8 to 16.1, depending on the model and its assumptions.

VI Experimental results versus theoretical predictions

1 Comparison with homogenization approaches

Figures 4.9A and 4.9B respectively report k/k_s and μ/μ_s as a function of p, where the data points corresponds to those of fig. 4.5. These figures also present the predictions of the different models discussed in sec. IV. As anticipated in sec. IV, the rule of mixtures (eq. 4.14) significantly overestimates the experimental data whereas the self-consistent model (eq. 4.19) accurately predicts them. The Mori-Tanaka scheme (eq. 4.18) is observed to fall in between.

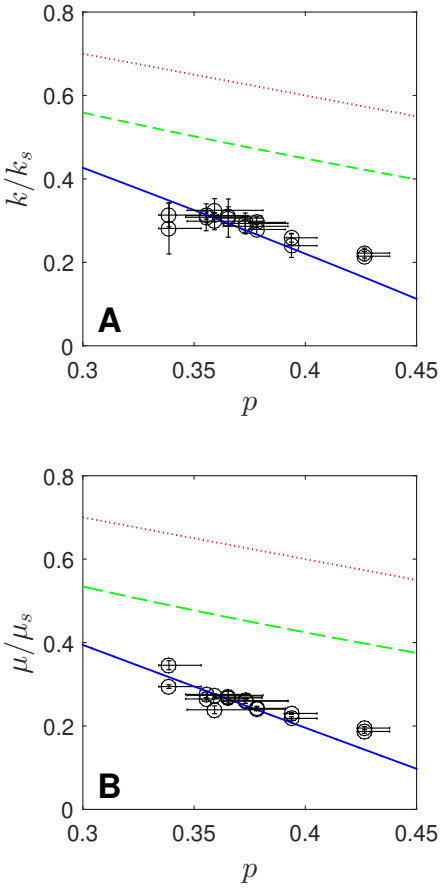

FIGURE 4.9: Normalized bulk modulus (k/k_s) and shear modulus (μ/μ_s) as a function of porosity (p). Normalization procedure uses bulk fused silica glass parameters (spec values from tab. 4.1). Lines correspond to theoretical schemes: rule of mixtures (red dotted line), Mori-Tanaka scheme (green dashed line) and self-consistent scheme (blue solid line).

The agreement between theory and experiment for both bulk and shear constants supports the hypothesis of isotropy made in the paper. If significant anisotropy existed in the packing, it would have resulted in the invalidation of eq. 4.10 and subsequent results. *De facto*, this gives some indication of the 3D packing structure which is difficult to access otherwise.

For the sake of completeness, fig. 4.10A and 4.10B present the Young's modulus (E) and Poisson's ratio (ν) as a function of p using the following equations (Landau and Lifshitz, 1970):

$$\mathrm{E} = \frac{9k\mu}{3k+\mu} \quad \text{and} \quad \nu = \frac{3k-2\mu}{2(3k+\mu)} \tag{4.25}$$

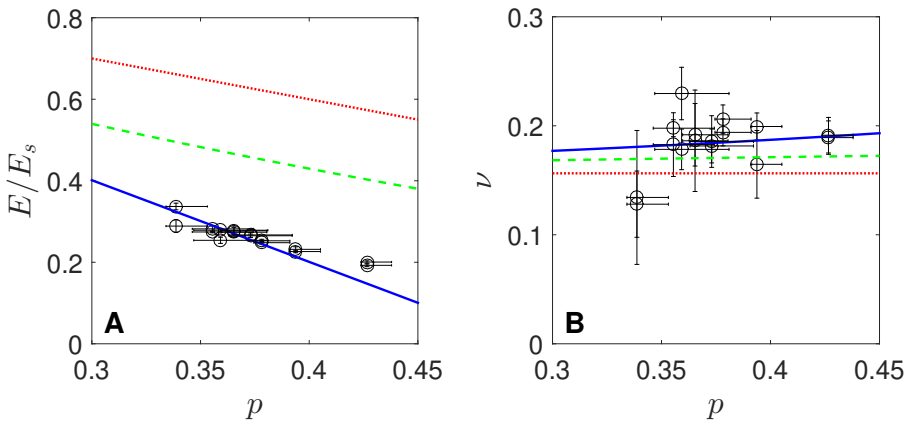

FIGURE 4.10: Normalized Young modulus (E) and Poisson's ratio (ν) as a function of porosity (p). The experimental values for E were normalized by the spec value of bulk fused silica glass (E_s). Lines correspond to theoretical schemes: rule of mixtures (red dotted line), Mori-Tanaka scheme (green dashed line) and self-consistent scheme (blue solid line).

Porosity is observed to affect only E, while ν remains constant within the error bars. The latter can be interpreted in conjunction with recent works (Rouxel, 2007; Greaves et al., 2011) correlating ν with the short-to-medium range connectivity of the network at the microscale, which, hence, likely remains almost constant for the considered porosity range.

2 Comparison with Kendall's type approach

Figure 4.11 compares the experimentally measured Young's modulus with the prediction of the self-consistent scheme (eq. 4.19 and 4.25) and that of Kendall (eq. 4.24). The latter better describes the dependency on p for

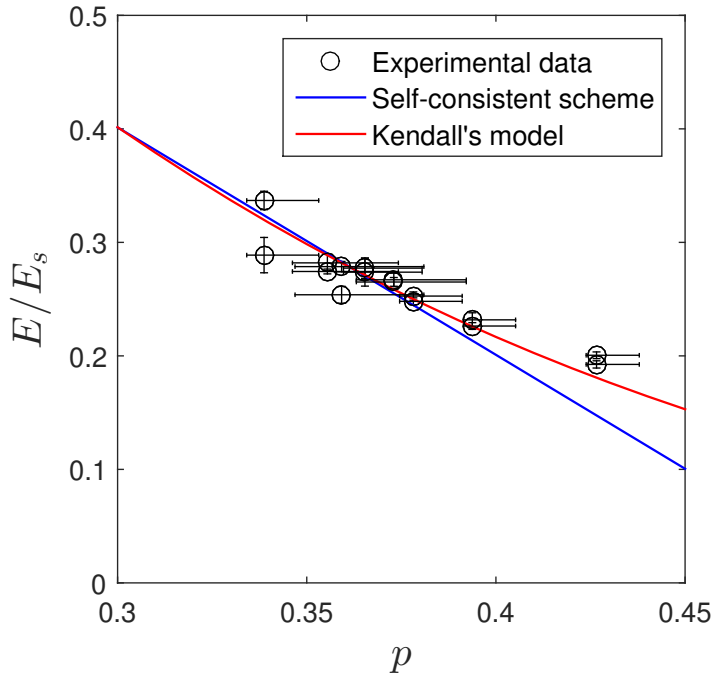

FIGURE 4.11: Normalized Young's modulus as a function of porosity. The numeric values used in Kendall's expression (eq. 4.24) were $E_s = 72.7\,\text{GPa}$, $a = 16.2\,\text{nm}$ (measured values) and $W = 5\,\text{J/m}^2$ (fitted value for A = 10.3, as used in Goehring et al., 2013; Birk-Braun et al., 2017; Goehring et al., 2015).

$p > 0.35$, at the price of an additional fitting parameter: the adhesion energy W. Taking, as before, $E_s = 72.7\,\text{GPa}$ and $a = 16.2\,\text{nm}$, the fit of the experimental data with Kendall's equation gives $W = 1.1\,\text{J/m}^2$ and $W = 10.7\,\text{J/m}^2$ for A = 16.1 and A = 8 respectively. Now, two types of surface energies are potentially relevant in the problem, as the interfacial energy could be attributed either to the breaking of covalent bonds (here siloxane) or to a surface tension (here silica/air or silica/water) as in fluids (Goehring et al., 2013; Birk-Braun et al., 2017). The macroscopic fracture energy for silica $G_c \simeq 8.2\,\text{J/m}^2$ (Rountree and Bonamy, 2014) relates to the breaking of silica bonds, as does Griffith's energy (Griffith, 1921) $2\gamma_s \sim 3.8\,\text{J/m}^2$. This energy represents the work applied to break the bonds on a unit surface: this is inferred from the energy needed to break a single bond (Luo, 2007), $7.5\,10^{-19}\,\text{J/bond}$ (450 kJ/mol), assuming 5 bonds per nm^2 (Iler, 1979) and no subsequent dissipation mechanisms such as plasticity or damage. The energies relating to the surface tension are considerably weaker: $\gamma_{SV} \sim 0.3 - 0.5\,\text{J/m}^2$ for silica/vacuum interfaces (Sarlat et al., 2006) and about six times less for silica/water interfaces (Goehring

et al., 2013).

The fitted value for W is several orders of magnitude larger than the ones associated with surface tension, but in line with the fracture energy of silica. This demonstrates that sintering during drying has probably led to the formation of covalent siloxane bonds between the particles.

VII Discussion

1 Competing models

The main outcomes from sec. VI are recalled and discussed:

- The self-consistent scheme provides the complete (tensorial) description of the elasticity, with no adjustable parameter. This for instance provides information on the isotropy of the material.
- The self-consistent scheme predicts an almost linear dependence of elastic constants with porosity. This is in agreement with the experiments for $p < 0.35$. At higher porosities, a small discrepancy with the experimental data appears, which suggests a missing physical ingredient.
- Kendall's model succeeds in reproducing the behavior of the Young's modulus over the whole porosity range studied herein. Thus, the discrepancy between the self-consistent scheme and the experimental data is likely due to surface effects, which are accounted for in Kendall's model.
- The increased accuracy of Kendall's model comes at the cost of an additional adjustable parameter, the adhesion energy. Moreover, the value of the prefactor involved in the model (A in eq. 4.24) depends on the precise assumptions made in the model (Thornton, 1993) and has a tremendous effect (A^3 dependence) on the determination of the adhesion energy.
- Kendall's model only predicts the Young's modulus and cannot provide any information on the isotropy of the material.

It should be stressed that looking for elasticity around ponctual contacts would result at the macroscopic scale in a non-linear stress-strain relationship (hertzian theory). As a consequence eq. 4.11 (and thus eq. 4.9) and eq. 4.24 remain valid provided that only small perturbations around an

unloaded reference configuration with a *finite* contact area are considered. Finally, as the two approaches are not mutually exclusive, it may be possible to refine the self-consistent scheme to take into account the adhesive surface forces (Brisard et al., 2010a; Brisard et al., 2010b) as in Kendall's approach.

2 The physics of colloidal drying

This study involves particles with 15 nm diameter. It is expected that surface effects decrease with increasing particle size, hence the self-consistent scheme is expected to be more accurate (over a larger porosity range) as the particle size increases (and vice versa). Additional experiments with particles of different diameters should verify this hypothesis.

The occurrence of cracks during drying reveals the cohesive nature of the packing. These cracks are due to the combination of three effects: the adhesion between the particles and the substrate, the overall retraction induced by water evaporation, and the transmission of tensile stresses from the substrate throughout the whole layer via the adhesion between the particles. Interpreting the present data in light of Kendall's model provides an estimate of the adhesion energy.

- The value inferred here for the adhesion energy ($W \simeq 1 - 10\,J/m^2$) is on the order of the fracture energy commonly reported for silica (Rouxel, 2007). Hence covalent siloxane bonds were probably formed between the particles during the drying.
- This value is several orders of magnitude larger than the one used in Goehring et al., 2013 and Birk-Braun et al., 2017 ($W = \gamma \simeq 0.01\,J/m^2$) to describe the same system (dried Ludox HS-40). However their study concerns the onset of cracking, while our measurements concern dried samples. This suggests an significant evolution of W with time during the drying process.
- The value of the adhesion energy can be recast into a fracture toughness using Irwin's relation (Irwin, 1957):

$$K_c = \sqrt{EW} \simeq 0.15 - 0.5\ \text{MPa.m}^{1/2}. \tag{4.26}$$

  This value measured at the end of drying is in line with the one estimated in Gauthier et al., 2010 at the onset of cracking.

A challenge is to measure *in situ* and independently, from the onset of cracking to the end of drying, the evolution of both the elastic properties and the fracture energy. This would provide important information on how and when the covalent bonds are formed.

VIII Conclusion

To summarize, this paper uses a highly porous material formed by the drying of a colloidal suspension as a benchmark for homogenization schemes of mechanical behavior. Using ultrasound measurements, it investigates the elastic properties of a dried layer of silica nanospheres. By modulating the drying rate, the influence of the porosity has been studied. It has been demonstrated that the self-consistent scheme accurately predicts both elasticity constants, with no adjustable parameters, as long as the porosity is small enough (less than 35% for 15 nm beads). For higher porosities, surface effects become visible; Kendall approach succeeds in taking them into account for a single elastic constant (Young's modulus), at the price of an additional adjustable parameter (adhesion energy). This adhesion energy is found to be on the order of the fracture energy in silica, implying that at the end of the drying the beads are probably linked by covalent bonds.

A surface energy equal to the fracture energy of the pure silica leads to a fracture toughness in line with that reported in Gauthier et al., 2010 for this kind of system. A step forward in these works would consist of measuring the elastic properties during drying. This would provide information on the formation of covalent bonds. Further steps are (i) to test self-consistent and Kendall's predictions by varying the particle size as this is expected to change the contribution of the surface effects and (ii) to use Kendall's approach to interpret, in physical terms, recent mathematical refinements of self-consistent schemes (Brisard et al., 2010a; Brisard et al., 2010b).

TABLE 4.2: Measured values for the porosity in each sample, using hydrostatic weighting in water and in ethanol. Due to water retention in the pores, actual values may be up to 1.5% larger (Piroird et al., 2016).

RH	p_w	p_{eth}
11	0.343	0.334
23	0.372	0.347
36	0.363	0.383
50	0.365	0.346
65	0.36	0.371
80	0.382	0.375
90	0.391	0.396
95	0.424	0.429

TABLE 4.3: Measured values for the elastic constants in each sample. Measurements for each sample were repeated on two morsels.

RH	k (GPa)	μ (GPa)	E (GPa)	ν
11	10.97 ± 0.99	10.78 ± 0.34	24.31 ± 0.59	0.13 ± 0.04
11	9.85 ± 2.15	9.19 ± 0.14	20.84 ± 1.13	0.13 ± 0.07
23	11.37 ± 0.98	7.45 ± 0.29	18.32 ± 0.54	0.23 ± 0.03
23	10.46 ± 0.72	8.53 ± 0.13	20.11 ± 0.34	0.18 ± 0.02
36	10.28 ± 0.87	8.13 ± 0.2	19.27 ± 0.43	0.19 ± 0.03
36	10.03 ± 0.51	8.1 ± 0.17	19.13 ± 0.29	0.18 ± 0.02
50	10.79 ± 1.14	8.6 ± 0.24	20.34 ± 0.54	0.18 ± 0.03
50	10.92 ± 0.3	8.26 ± 0.08	19.8 ± 0.16	0.2 ± 0.01
65	10.72 ± 1.61	8.34 ± 0.5	19.75 ± 0.89	0.19 ± 0.05
65	10.89 ± 0.79	8.4 ± 0.45	20.01 ± 0.65	0.19 ± 0.03
80	10.36 ± 0.44	7.56 ± 0.16	18.23 ± 0.27	0.21 ± 0.02
80	9.76 ± 0.42	7.5 ± 0.12	17.9 ± 0.23	0.19 ± 0.02
90	8.4 ± 0.99	7.18 ± 0.08	16.72 ± 0.45	0.16 ± 0.04
90	9.07 ± 0.37	6.81 ± 0.13	16.33 ± 0.22	0.2 ± 0.02
95	7.78 ± 0.42	6.09 ± 0.11	14.47 ± 0.22	0.19 ± 0.02
95	7.52 ± 0.4	5.83 ± 0.14	13.89 ± 0.23	0.19 ± 0.02

IX Addendum: Elastic constants as a function of particle size

The results reproduced above hint at the importance of surface effects in the prediction of elastic properties: Kendall's model, which takes into account an adhesion energy between the particles, gives a better prediction of the Young's modulus than the self-consistent scheme for the most porous layers. The self-consistent scheme, however, predicts both elastic moduli and does not rely on any adjustable parameter. We thus repeated the studies reported in the Soft Matter paper (on HS-m) on layers obtained from the three other suspensions: SM, HS-p and TM .

Figures 4.12A and 4.12B show both the bulk and the shear moduli measured on the four suspensions, normalized by the moduli measured on fused silica. They depend not only on porosity but also on the suspension type; that is, the particle size of the initial suspension seems to affects the elastic properties of the dry layers.

A possible explanation is that the stiffness of the individual particles could vary from suspension to suspension. Figures 4.12C and 4.12D represent the bulk and the shear moduli measured on the four suspensions, fitting the normalization values k_s and μ_s in order to obtain the best agreement with the self-consistent scheme. Fitted values for the moduli of the solid phase for each suspension are presented in tab. 4.4. The self-consistent scheme, which only invoke porosity as a parameter, is thus able to describe the elasticity of dry colloidal silica, assuming that the different colloidal suspensions have different particle stiffness. This physical parameter is however not directly accessible. Moreover, such a large range of values seems implausible since the particles are expected to share the same composition: amorphous silica with small amounts of sodium ($0.5 - 2\%$ in mass).

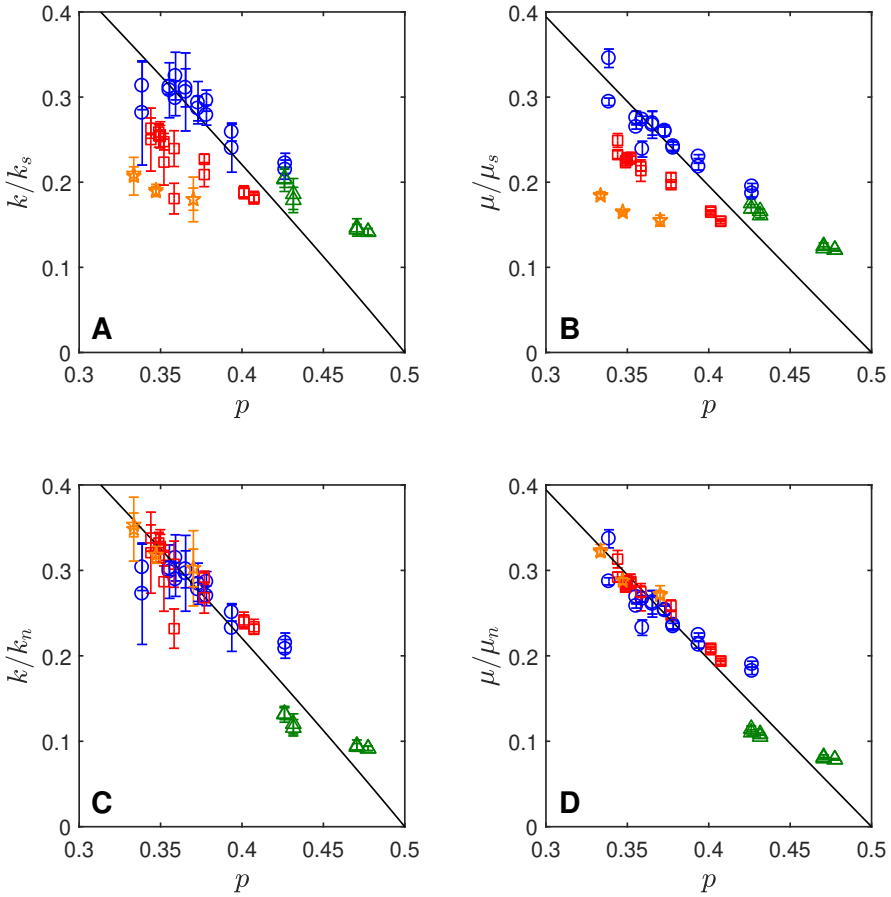

FIGURE 4.12: (A) Normalized bulk modulus (k/k_s) and (B) shear modulus (μ/μ_s) as a function of porosity, for each of the four Ludox suspensions. The normalization values k_s and μ_s were those measured on fused silica. The black line represents the prediction of the self-consistent scheme. (C) Normalized bulk modulus (k/k_n) and (D) shear modulus (μ/μ_n) as a function of porosity, for each of the four Ludox suspensions, fitting the normalization values k_n and μ_n in order to obtain the best fit with the self-consistent scheme. The fitted value for k_n and μ_n are given in tab. 4.4.

Suspension	k_n (GPa)	μ_n (GPa)
SM	54.2	47.7
HS-m	36.1	32
HS-p	27.3	24.8
TM	20.8	17.8

TABLE 4.4: Fitted bulk modulus and shear modulus for the solid material of the four suspensions.

Kendall's model may give a better prediction of the behavior of the dry layers, as it explicitly takes into account particle size and surface effects (through an adhesion

energy). Figure 4.13A represents the Young's modulus measured on all the layers, as well as the predictions of Kendall's model for each suspension, using the median particle size as measured in SAXS. The adhesion energy used was $W = 5\,J/m^2$ (obtained by fitting the experimental data on HS-m layers). Kendall's model overestimates the stiffness of HS-p, SM and TM layers. Figure 4.13B presents the same experimental data with Kendall's predictions; this time, the adhesion energy was individually fitted for each initial suspension, and the agreement is much better. The inferred adhesion energies range between 1.7 and $5\,J/m^2$; they are given in table 4.5. Such a range for the surface energy W is compatible with the macroscopic fracture energy $G_c \simeq 8.2\,J/m^2$ or Griffith's bond-breaking energy $2\gamma_s \sim 3.8\,J/m^2$, especially when taking into account the uncertainty on the prefactor A in eq. 4.24. However, there is no clear explanation of the dependence of W on the initial suspension . Differences in chemical composition may play on the adhesion energy, since sodium concentration varies from suspension to suspension. Moreover, sodium atoms are expected to be located at the surface of the particles, where their effect on the silica network could influence the adhesion energy.

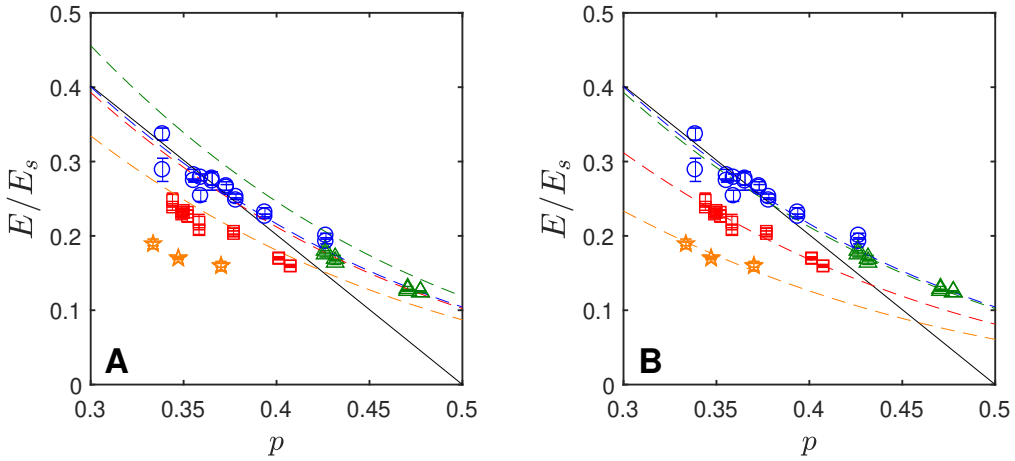

FIGURE 4.13: Normalized Young's modulus as a function of porosity for each of the four Ludox suspensions. Dashed lines represent the predictions of Kendall's model for each suspension, depending on its particles size: green for SM (radius 5.5 nm), blue for HS-m (radius 8.2 nm), red for HS-m (radius 8.6 nm), orange for TM (radius 14 nm). (A) The surface energy used in Kendall's model was constant, equal to $W = 5\,Jm^{-2}$. (B) The surface energy was fitted separately for each suspension; fitted values are given in tab. 4.5.

Suspension	r (nm)	σ/R_m	W (J/m^2)
SM	5.5	0.19	3.2
HS-m	8.1	0.14	5
HS-p	8.6	0.31	2.5
TM	14.0	0.10	1.7

TABLE 4.5: Particle radius, dispersity and surface energy (inferred from Kendall's model) for the four silica suspensions.

Conclusion

The self-consistent homogenization scheme and Kendall's model can predict the elasticity for the layers obtained from the four silica suspensions. However, fitting the physical parameters used in the models is necessary to obtain a good agreement with the experimental data. These physical parameters are the stiffness of the particles material (for the self-consistent scheme) and the adhesion energy (for Kendall's model); they are not directly accessible. A way to proceed further would be to produce the colloidal suspensions in-house in order to have better control over the properties of the particles.

Chapter 5

Fracture properties

Introduction

The previous chapter concerns the elastic properties of the dry colloidal layers and relates them to the porosity and the particle size. In addition to elasticity, dry colloidal systems also vary in their fracture properties. Many colloidal systems spontaneously crack during the desiccation process; however, in many industrial processes involving colloidal drying, such as the preparation of surface coatings, fracture is an undesired outcome during solvent evaporation as well as in the final dry material.

In this chapter, I first review the evolution of the colloidal silica layers during desiccation as well as the crack patterns observed. Using image segmentation, Vickers indentation, and mass-images correlation, I analyze the influence of our two control parameters (evaporation rate and suspension type) on the fracture properties of the colloidal layers. I find the drying rate to influence both the fracture patterns formed during drying, and the final mechanical properties of the layers: layers dried at higher evaporation rates show more in-situ cracking but a higher resistance to fracture in their dry, final state. In order to explain this contrary and counterintuitive evolution of crack spacing and fracture resistance with the evaporation rate, I discuss the physical and chemical consolidation processes which take place during colloidal drying, as well as their relative timescales.

I Desiccation cracks

1 Mass evolution

As a colloidal silica suspension dries, it first transitions from a liquid state to a rigid, saturated gel. Further evaporation of the liquid gradually makes the colloidal layer more compact. The pores then desaturate and complete drying yields a porous solid layer. Our experimental setup allows the acquisition of both layer mass and layer

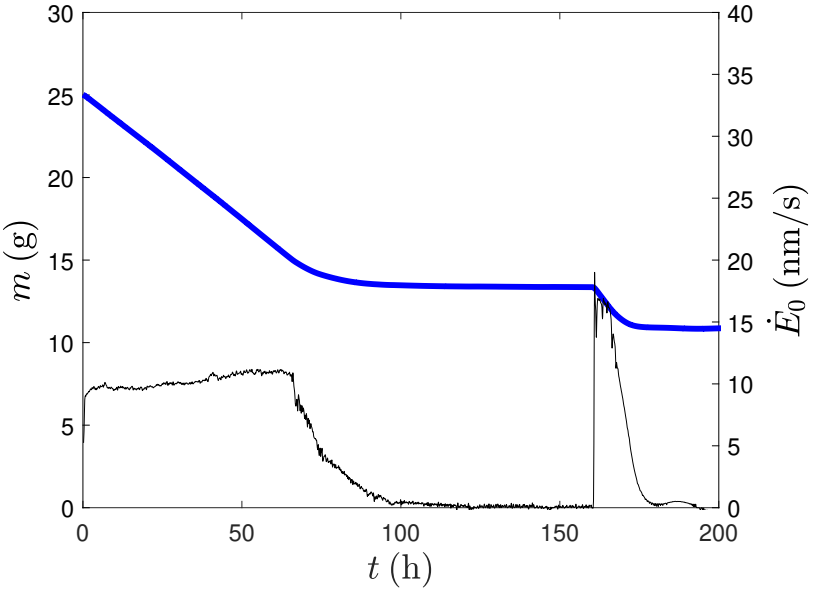

FIGURE 5.1: Drying experiment on a layer of HS-p suspension at RH = 80%: mass m (thick blue line, left y-axis) and evaporation rate $\dot{E}$ (thin black line, right y-axis) as a function of time t.

aspect during the drying process. Figure 5.1 represents the evolution of mass (m) with time (t) on a layer of HS-p suspension dried at RH = 80% (thick blue line) as well as the evaporation rate $\dot{E} \sim -\frac{dm}{dt}$ (thin black line). As outlined in chap. 2, the evaporation rate is first constant (during the constant rate period) and then decreases (during the falling rate period) to reach zero at the end of the drying. In the experiment pictured here, the falling rate period began at $t = 65 \pm 2$ h. Since the sample was dried in a high humidity atmosphere (RH = 80%), the evaporation stopped ($\dot{E} = 0$) while the pores of the layer still contained water. Thus a quenching process, beginning at $t_q = 160.8$ h, was necessary to obtain a completely dry sample.

2 Visual evolution

As the layers dry, they all undergo similar transformations. Figure 5.2 represents successive stages of the evolution of the same layer represented on fig. 5.1 dried from HS-p suspension at RH = 80%:

- During the first phase of the drying, the layer remains clear and continuous (fig. 5.2A). When dried at very high evaporation rates (RH $\leqslant$ 10%), layers tends to buckle as they gel. This is sometimes visible via the camera. Layers dried at other RH do not buckle and the gelling of the suspension is not visible

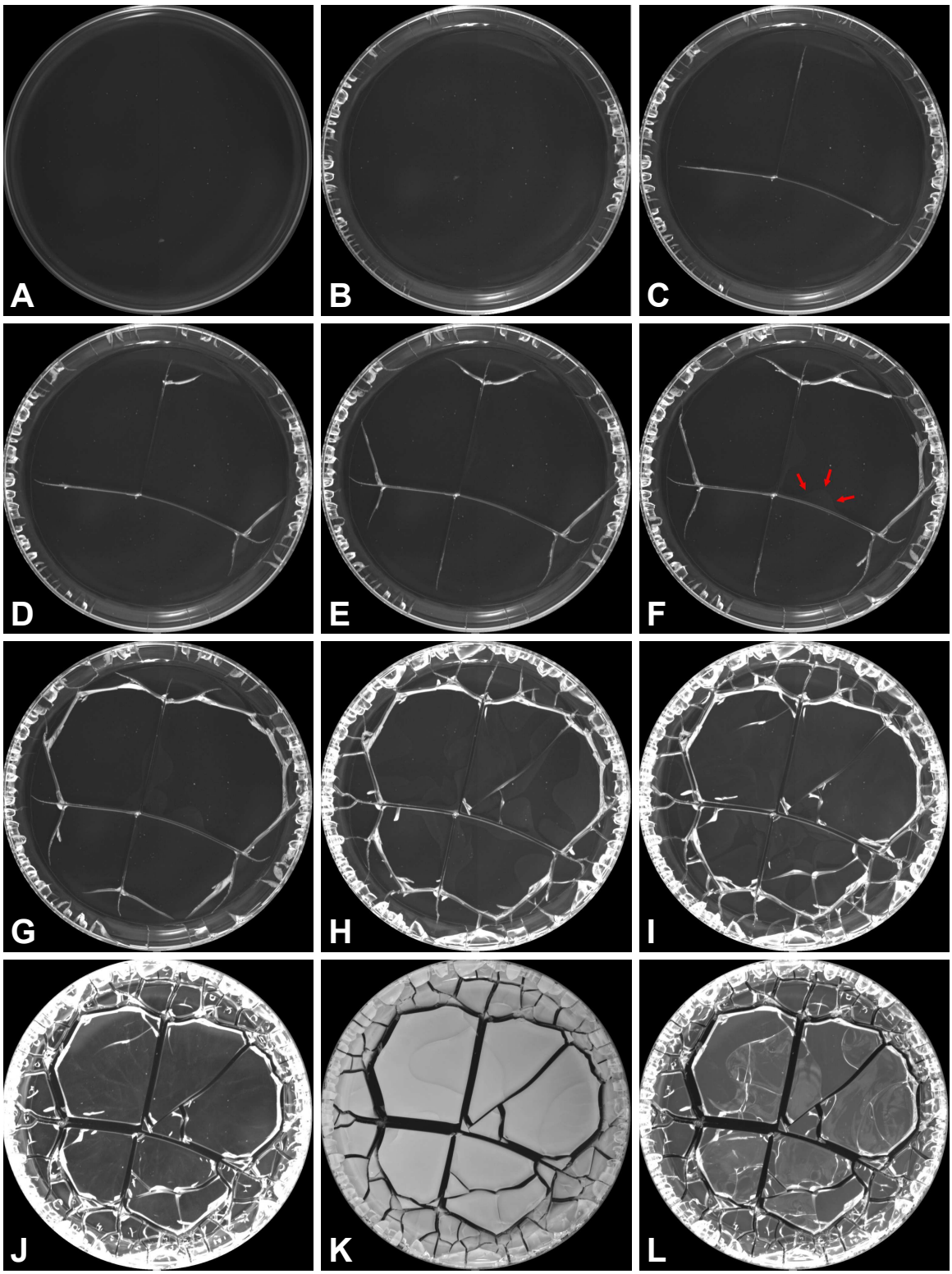

FIGURE 5.2: Sequence of images captured during the drying of a layer of HS-p suspension at RH = 80%. On this experiment, the constant rate period ended at $t = 65 \pm 2$ h and the quenching process (command RH switched from 80% to 10%) started at $t_q = 160.8$ h. Time elapsed since the beginning of drying: (A) 0 h, (B) 57.25 h, (C) 57.75 h, (D) 58.25 h, (E) 58.75 h, (F) 59.25 h, (G) 59.75 h, (H) 62.5 h, (I) 65.25 h, (J) 94.75 h, (K) 162.8 h, (L) 193.5 h. Images (B) to (G) are evenly spaced. Red arrows on (F) outline a delamination front.

via the camera, except for small cracks which can appear at the edge of a layer, where a meniscus is present (fig. 5.2B).

- At some point during the drying, close to the end of the linear period (*i.e.* when $\dot{m}(t) = \dot{m}_0$), a hierarchical network of cracks begins to form in the layer (fig. 5.2C - 5.2I).

- As soon as a crack is formed, it starts widening as the adjacent morsels shrink and delaminate (*i.e.* peel off the glass substrate), from their edge (where they touch the crack opening) to their center. This happens as other cracks are still opening. On fig. 5.2, crack widening is visible in panels (G) to (J). Panels (F) to (H) show partial delamination, and a delamination front is outlined[1] on panel (F).

- At some point, the layer becomes opaque (fig. 5.2K). This normally happens once the formation of the crack network is complete; however, layers dried at RH $= 10 - 23\%$ can have directional drying, with one side of the sample drying faster than the other does. For these layers, opacification can coexist with fracture formation.

- Finally, the layer becomes transparent again. Thin weakly opening cracks may form during the opaque phase and become visible at this stage. Some layers also undergo internal delamination, *i.e.* they develop cracks which run parallel to the substrate and separate the layers into top and bottom morsels. Internal delamination is visible on fig. 5.2L as light reflects on the irregular fracture surfaces.

Note that at high relative humidities (RH $\geqslant 80\%$), capillarity traps water in the pores of the layers. Opacification and de-opacification then only occur during the quenching phase, when RH_c is set to 10%.

The opacification and de-opacification of the layer can be attributed to the penetration of air in the porous medium. As the silica particles have a characteristic size $d \simeq 10 - 25\,\mathrm{nm}$ which is very small compared to the wavelength of light ($\lambda = 400 - 800\,\mathrm{nm}$ for visible light), the porous medium is homogeneous at the length scale of the light rays. Hence, very little scattering happens and the layer is transparent, despite the contrast in optical indices between silica ($n_{SiO_2} = 1.47$) and air ($n_{air} \simeq 1$) or water ($n_{\mathrm{H_2O}} = 1.33$). The evolution of the layer opacity during the drying can thus be understood as follows:

[1] The contrast between delaminated and non-delaminated areas is very weak and delamination fronts may not be visible on printed versions of this document.

- When the pores of the colloidal layer are saturated with water, very little scattering happens, as the layer is effectively homogeneous at the wavelength scale.

- When the air-liquid interface recedes into the layer and air enters the pores, the layer becomes opaque. This is due to the coexistence of drained regions (*i.e.* regions with air-filled pores) and saturated regions (*i.e.* regions with water-filled pores). Since the optical indices of air and water differ significantly, the drained regions and saturated regions have different effective indices. When these regions have a characteristic size comparable to the wavelength of visible light ($400 - 800\,\mathrm{nm}$), this index contrast enables strong light scattering, making the layer opaque.

- When the drying is complete, all the pores are empty. Hence, the layer is transparent as it is, once again, effectively homogeneous at the wavelength scale. The slight opalescence which can still be observed could be due to the contrast in indices between air and silica, which is larger than the contrast between water and silica, and which might cause some scattering despite the small length scale of the heterogeneities.

3 Fracture patterns

The final fracture patterns show considerable variation from experiment to experiment, depending on the drying rate and suspension used. Figure 5.3 shows crack patterns obtained in our drying experiments on the four suspensions, pictured during the opaque phase. They are sorted in order of increasing particle size (columns, from left to right: SM, HS-m, HS-p and TM suspensions) and increasing RH, *i.e.* decreasing drying rate (rows, from top to bottom: RH_c = 10%, 36%, 80% and 95%).

Comparing the fracture patterns obtained from the experiments reveals two important trends:

- Crack spacing increases and morsel count decreases when drying rate decreases (*i.e.* when RH is increased). Thus, layers dried at RH = 10% (fig. 5.3, top row) exhibit several tens of small morsels, whereas some layers dried at RH = 95% fracture into very few morsels.

- The relative contraction of the morsels decreases with increasing particle size. Compared to HS layers (particle radius $r \simeq 8\,\mathrm{nm}$), cracks in TM layers (radius $r \simeq 14\,\mathrm{nm}$) have small openings and the morsels cover a larger area of the Petri

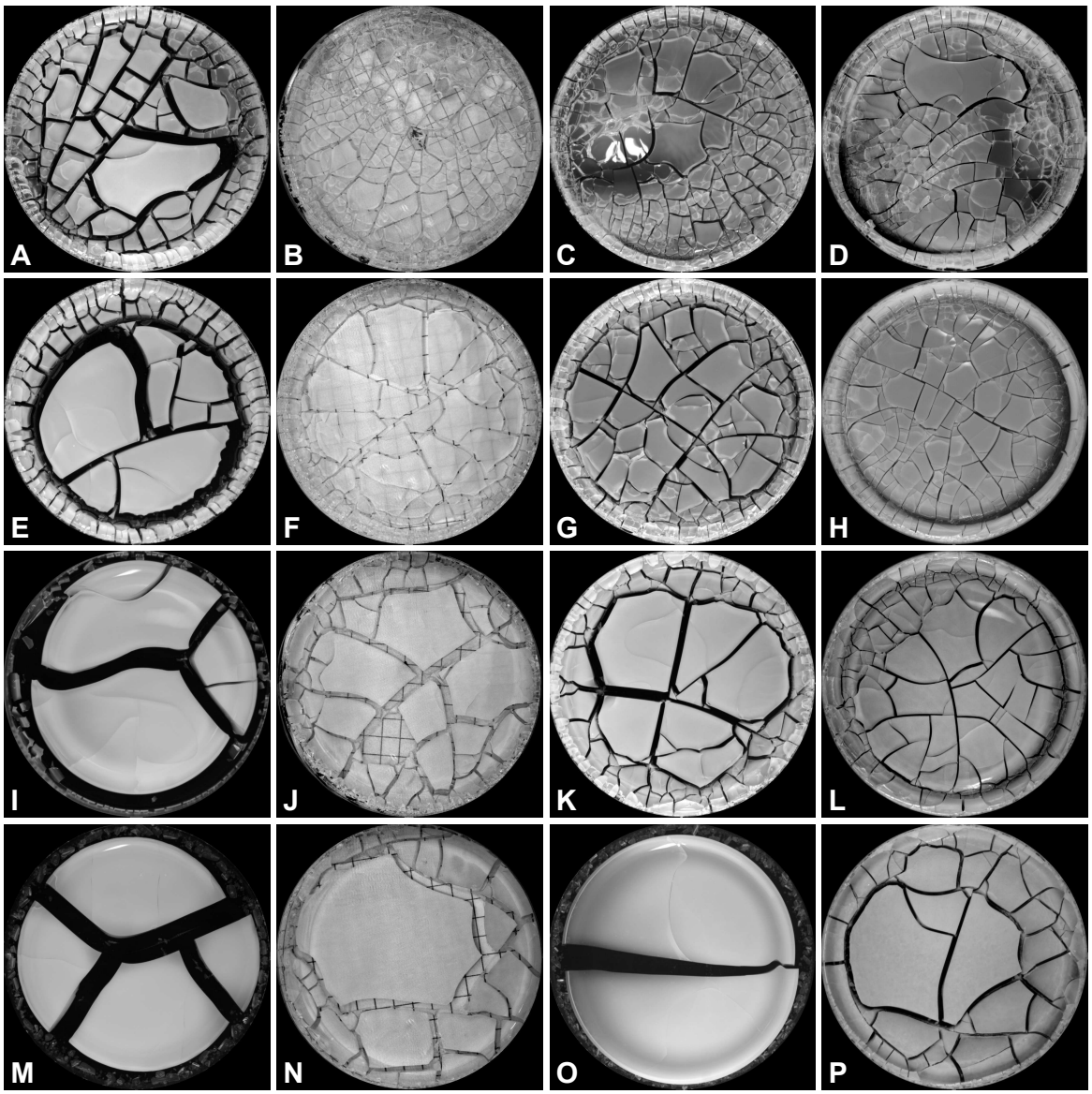

FIGURE 5.3: Drying colloidal silica layers, pictured during the opaque phase. First row: layers of (A) SM, (B) HS-m, (C) HS-p and (D) TM suspensions, dried at RH = 10%. Second row: layers of (E) SM, (F) HS-m, (G) HS-p and (H) TM suspensions, dried at RH_c = 36%. Third row: layers of (I) SM, (J) HS-m, (K) HS-p and (L) TM suspensions, dried at RH_c = 80%. Fourth row: layers of (M) SM, (N) HS-m, (O) HS-p and (P) TM suspensions, dried at RH_c = 95%.

dish once the drying is complete. Conversely, cracks in SM layers ($r \simeq 5.5\,\mathrm{nm}$) open wider and the morsels cover a smaller area.

In addition, note that directional drying affects many of the fast-dried layers. On the HS-m layer dried at $RH_c = 10\%$ (fig. 5.3B), opacification is not uniform but starts on one side of the sample and progresses to the other side, hence leading to the coexistence of opaque and transparent regions. Directional drying can also cause buckling, which is for example visible on HS-p dried at $RH_c = 10\%$ (fig. 5.3C), as the tilted surface produces reflections from the light source.

II Methods

1 Statistical analysis of final fracture patterns

In order to quantify the differences in morsel size and crack width observed on the dry layers, it is necessary to process the images to segment the morsels and perform statistics.

Several automatic segmentation methods were tested, but they proved inadequate on our system. Simple binarization methods failed because of uneven illumination; using the watershed algorithm resulted in strong over-segmentation. Thus, I wrote a Matlab routine implementing a semi-manual method. In a first step, the built-in Matlab function *activecontour* uses the Chan-Vese algorithm (Chan and Vese, 2001) to segment the image and separate the solid morsels from the background. Nonetheless, the segmentation obtained is often imperfect. Thus, a second step requires manually adding or removing image areas from the background. For each drying experiment, I segmented images in the opaque phase, when all desiccation cracks have opened and the white morsels strongly contrast with the black background. Layers dried from HS-m suspension were imaged on a white background (sheet of graph paper), making the *activecontour* function ineffective. Hence, I segmented these images entirely by hand.

Close to the edge of the Petri dish, the suspensions tend to break into smaller morsels, as the presence of a rigid wall introduces a meniscus and modifies the stress repartition. In order to avoid edge effects, morsels close to the Petri dish edge were omitted from the statistics. The threshold for inclusion into the statistics was that the distance between the center of the dish O and the center of gravity G of a morsel must be less than 0.75R, where R is the radius of the Petri dishes. Herein,

the radius of the Petri dishes was R = 3.5 cm; thus, a morsel was included in the statistics when

$$|\mathrm{OG}| \leqslant 0.75\mathrm{R} = 2.625\,\mathrm{cm} \tag{5.1}$$

Furthermore, morsels with a drying surface area less than 1 mm^2 were omitted. Figure 5.4A represents an image as captured by the camera (a black mask was applied to the area outside the Petri dish). Figure 5.4B depicts the segmented image: disregarded material appears in grey.

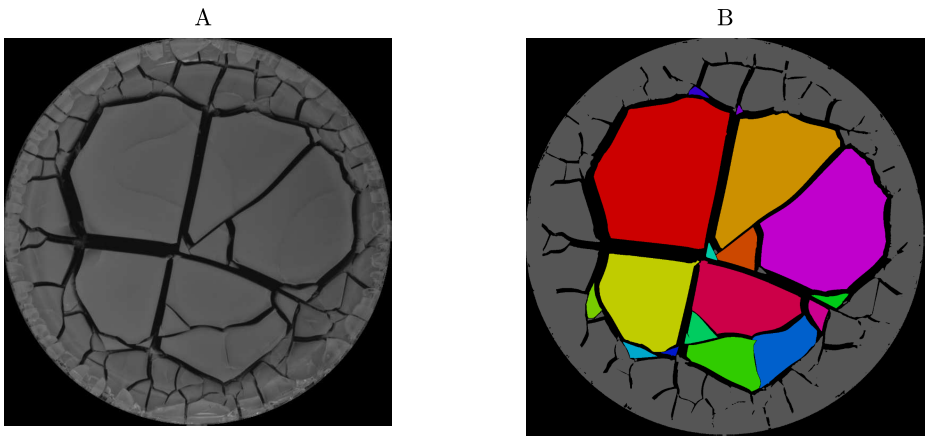

FIGURE 5.4: Result of segmentation for a layer of polydisperse RH dried at RH = 80%: (A) raw image and (B) segmented image. Statistical calculations only concern morsels which appear in color; grey ones were excluded.

2 Microindentation tests

Microindentation tests are a well-accepted and practical means for assessing the mechanical properties of thin layers. In a microindentation test, a hard tip with a defined geometry applies a specific load at the surface of a sample.

Herein, indentation tests use the Vickers indenter. This indenter has a pyramidal diamond tip, which is forced upon a surface with a specified load. Upon removing, a residual square imprint (an 'indent') remains. Figure 5.5 represents the successive stages of a Vickers indentation test, and fig. 5.6A depicts a typical indent obtained at low loads. From the size of the square indent (*i.e.* the half-diagonal length a) and the applied load P, one can define the Vickers hardness (Oliver and Pharr, 1992):

$$\mathrm{H}_v = 1.8544\frac{\mathrm{P}}{(2a)^2} \tag{5.2}$$

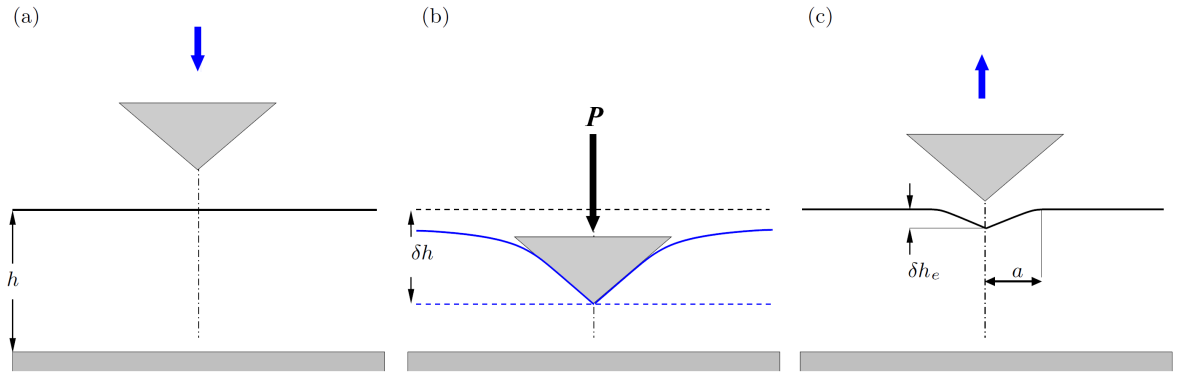

FIGURE 5.5: Principle of a Vickers indentation test. (a) Initial setup for a layer of thickness h. (b) The tip applies an increasing load up to a value P and penetrates to a maximum depth δh under the initial surface. (c) The load is progressively decreased and the tip removed, leaving at the surface of the material an indent of half-diagonal a and remanent depth δh_e.

In this manuscript, loads are expressed in N and hardness values in GPa. In the absence of material damage, H_v is independent of the load P and characterizes the resistance of the material to plastic deformation.

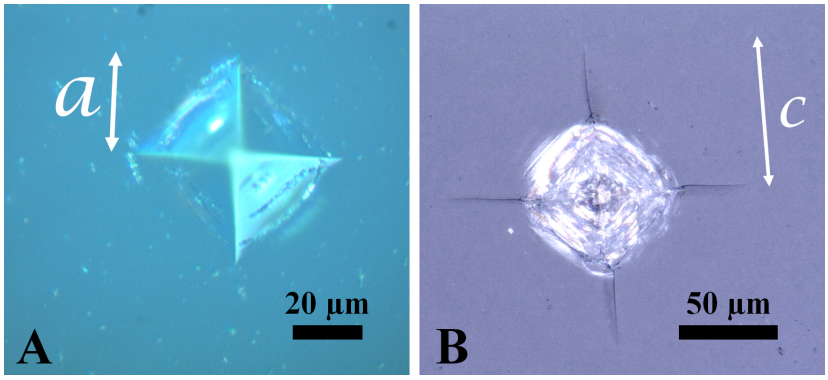

FIGURE 5.6: (A) Indent on the top surface of a HS-p layer dried at RH = 36%. Load was P = 1 N. (B) Indent on the top surface of the same sample. Load was P = 5 N. The higher load applied generates cracks at the corners of the indent. Indent size a and crack length c are represented.

Increasing the load will initiate cracks off the corners of the indent; fig. 5.6B presents an indent with four well-formed cracks. Equations derived from Vickers indentation fracture models then express the toughness of the material as a function of indent size and crack length (Ponton and Rawlings, 1989). The validity of a given

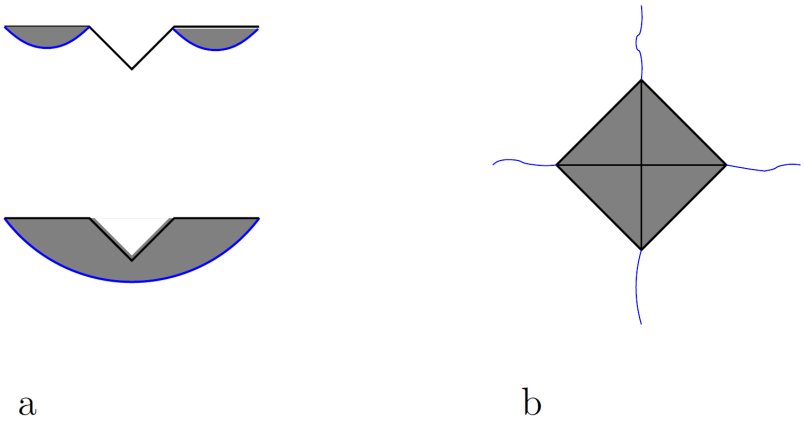

FIGURE 5.7: (a) Two morphologies of fracture generated during Vickers indentation: Palmqvist (top) and half-penny (bottom) cracks. The view is cut along a vertical plane containing an indent diagonal. The sample surface is represented in black, the crack fronts in blue, the crack surfaces in grey. (b) Top view of a Vickers indent.

equation is generally restricted to a specific class of materials, as different materials fracture in different ways during indentation, which plays on the stress repartition in the sample during loading and unloading (Cook and Pharr, 1990). Moreover, most models involve prefactors inferred by fitting experimental data. Thus, the equation used for the determination of K_c should have been developed on the same class of material as the one under study, and should be tested on a reference material of known K_c. In order to estimate the fracture toughness of the porous silica layers, I used a model developed by Lawn, Evans and Marshall (Lawn et al., 1980), valid for materials in which half-penny median-radial cracks develop (see fig. 5.7 for a representation of this crack morphology). Such cracks appear when the crack length c (measured from the center of the indent to the crack tip) verifies $c > 1.25a$, which is the case in our samples. Lawn, Evans and Marshall's equation is often used to estimate K_c in bulk silica-based glasses and expresses the fracture toughness K_c as

$$K_c^{vic} = 0.0134 \left(\frac{E}{H_v}\right)^{\frac{1}{2}} \frac{P}{c^{\frac{3}{2}}} \tag{5.3}$$

Microindentation tests were run in Université de Rennes, under the direction of Fabrice Célarié. As for the measurement of elastic moduli, the tests were performed several months after the preparation of the layers, when their mechanical properties are observed not to evolve anymore. For each drying experiment, a single morsel was used for the microindentation tests. Five indents were made on the top surface of each tested morsel. I wrote and used a Matlab routine to measure the cracktip to

cracktip distance ($2c$) and diagonal length ($2a$) on optical microscope images of the indents, yielding for each indent two values of a and c and thus two values of K_c^{vic}. Using this procedure, I tested Lawn's model on fused silica glass (Dow Corning 7980) with a load P = 5 N and found $K_c^{vic} = 0.7\,MPa.m^{1/2}$, in accordance with values found in the literature (*e.g.* $K_c = 0.77\,MPa.m^{1/2}$ in Rountree and Bonamy, 2014).

Indentation may cause damage to the tested material; in this case, H_v and K_c are not material constants but depend on the applied load P, an effect known as the indentation size effect (Li and Bradt, 1992). Thus, comparisons of K_c^{vic} values should ideally involve measurements conducted at constant load P. Our microindentation tests were first run on HS-m and HS-p layers with an applied load P = 5 N. However, SM samples were very resistant to fracture and many of them showed no cracking at P = 5 N. Conversely, TM samples were very brittle and indentation at P = 5 N sometimes resulted in very long cracks ($c > 5a$). Large indents with long cracks are impractical in TM samples, as TM layers exhibit a creasing pattern which divides the surface in polygonal cells (Boulogne et al., 2015), and cracks interact with the edges of the cells. Thus the load applied was P = 10 N for SM samples and P = 3 N for TM samples.

In order to estimate the influence of the indentation size effect on our experiments, I conducted measurements on two samples (dried from HS-p suspension at RH = 10% and 95%) with loads P = 3 N, 5 N and 10 N. Figure 5.8A gives the indent size a, and fig. 5.8B gives the crack length c for the two samples at the three loads applied. Figures 5.8C and 5.8D respectively show the Vickers hardness H_v and the fracture toughness K_c^{vic} inferred from the indentation tests on the two samples. H_v values slightly decrease with the applied load, which indicates some indentation size effect in our system. However, there is no effect of the applied load on K_c^{vic}.

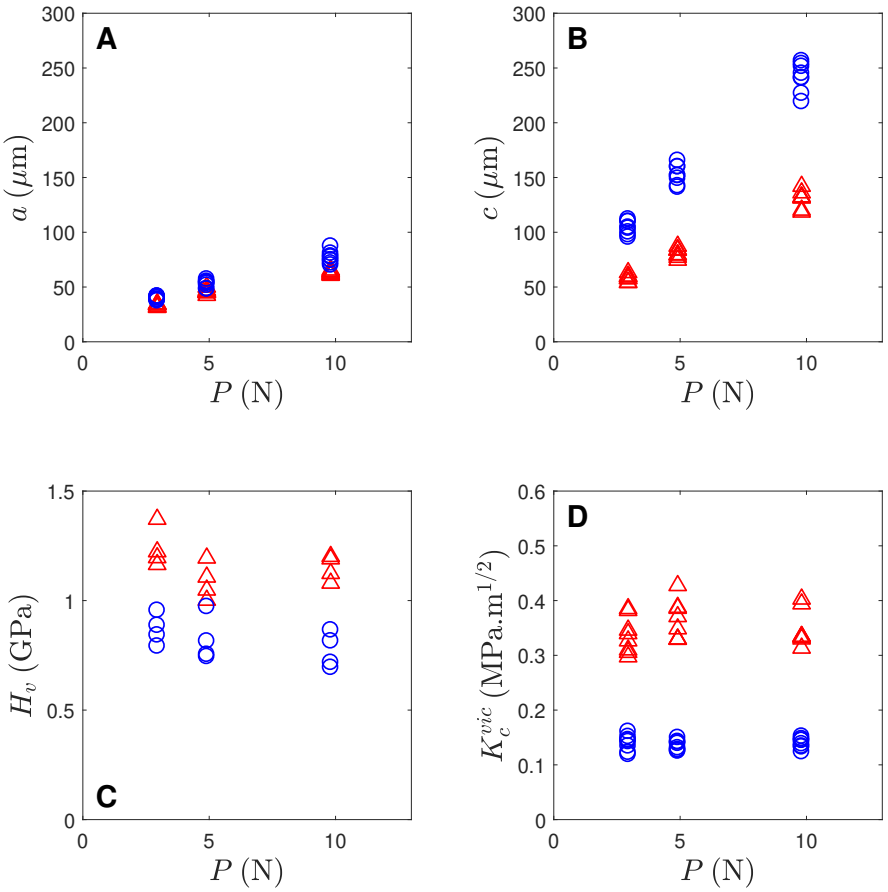

FIGURE 5.8: Influence of load P on inferred Vickers hardness H_v and fracture toughness K_c^{vic}. (A) Indent size (half-diagonal length a) as a function of load P on HS-p layers dried at RH = 10% (red triangles) and RH = 95% (blue circles). For each load and each morsel, four indents were made, yielding eight values for a. (B) Crack length c as a function of load P, measured on the same indents. (C) H_v values inferred from indent size. (D) K_c^{vic} values inferred from indent size and crack length. For both layers, H_v decreases with the applied load P, but there is no dependence of measured K_c^{vic} on P.

3 Mass-images correlation

When a dry layer is soaked in a solvent (such as water or ethanol) and left to dry under ambient conditions, it is initially transparent. Yet as soon as the solvent begins to evaporate, opacification commences. Thus, the apparition of opacity in a drying experiment corresponds to the precise moment when the water-air interface starts receding into the solid layer (*i.e.* air begins to enter the pores).

Correlating the mass curves with the images captured by the camera provides:

- m_{frac}: the mass at which the first crack opens (this excludes the meniscus close to the edges, which dry early on and displays cracks before the bulk of the sample);

- m_{desat}: the mass at which the layer starts opacifying, which marks the desaturation time (*i.e.* the time at which air enters the pores).

At both of these events (first fracture and opacification), the layer is saturated with water; the volume fraction ϕ of silica in the layer can thus be expressed, from the mass m of the layer, as:

$$\phi = \frac{V_{sil}}{V_{H_2O} + V_{sil}} = \frac{m_{sil}/\rho_{sil}}{(m - m_{sil})/\rho_{H_2O} + m_{sil}/\rho_{sil}} \tag{5.4}$$

where $V_{sil} = m_{sil}/\rho_{sil}$ is the volume of silica and $V_{H_2O} = m_{H_2O}/\rho_{H_2O}$ the volume of water ($\rho_{sil} = 2.26\,\mathrm{g/cm^3}$ and $\rho_{H_2O} = 1\,\mathrm{g/cm^3}$). Silica mass $m_{sil} = m_0\phi_m$ was estimated from the initial suspension mass m_0 (25 g for HS-p, HS-m and TM layers and 33.33 g for the SM layers) and the silica mass fraction ϕ_m measured on each of the four suspensions by weighing dry extracts.

III Results

1 Fracture patterns

Figure 5.9 gives mean sample size as a function of evaporation rate for all the layers. The following experiments were excluded from the statistics:

- HS-m, HS-p and TM layers dried at RH = 10% and the HS-p layer dried at RH = 23%, as they showed irregular thickness due to directional drying;

- SM, HS-m and HS-p layers dried at RH = 95% and SM dried at RH = 80% as they had large morsels touching the edge of the Petri dish (see fig. 5.3).

- On the HS-m layer dried at RH = 80%, a morsel was taken out of the drying box before the beginning of the opaque phase (see fig. 5.3J).

Mean sample size $\overline{A}$ decreases with the evaporation rate $\dot{E}_0$. Thus, drying slowly leads to less cracking and larger morsels.

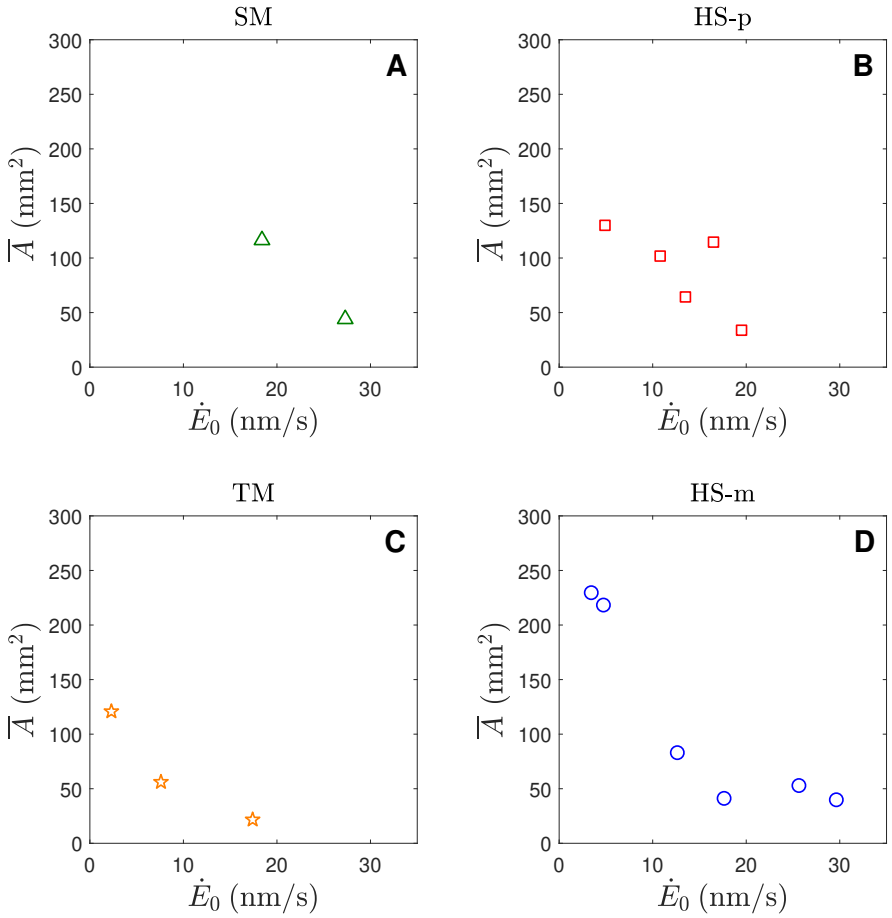

FIGURE 5.9: Mean morsel size $\overline{A}$ as a function of the evaporation rate $\dot{E}_0$ for the four initial suspensions: (A) SM, (B) HS-p, (C) TM and (D) HS-m. For each suspension, mean morsel size increases with decreasing drying rate. In other words, drying slowly leads to less cracking and larger morsels.

Figure 5.10 represents the retraction coefficient κ as a function of the evaporation rate on all layers. The retraction coefficient is defined as the ratio of the surface of the crack openings over the total surface (inside the disk defined by eq. 5.1). A higher retraction coefficient means that the cracks open wider and that the silica morsels formed by the fracture of the layer undergo more shrinkage during the rest of the drying process.

The retraction coefficient is lower for TM layers and higher for SM layers, compared to HS-m and HS-p layers; thus, κ decreases with increasing particle size. This may be related to the capillary pressure P_{cap}, which is the driving force for the compaction of the particles during the second phase of the drying (when the layer is a solid gel with saturated pores). As mentioned in chap. 1, P_{cap} scales as $1/r$ (with r

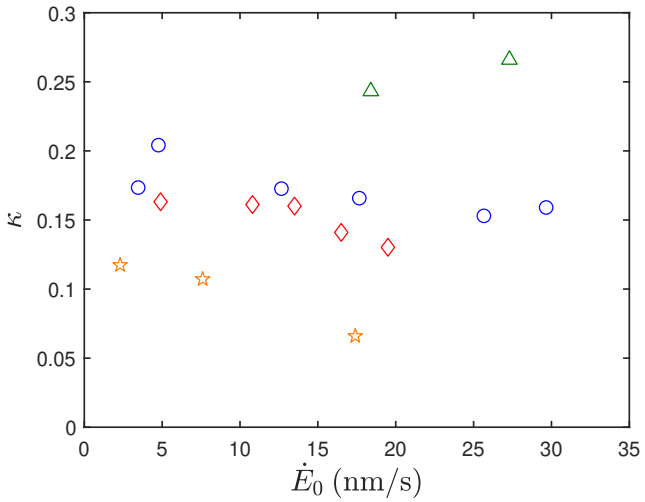

FIGURE 5.10: Retraction coefficient κ as a function of the evaporation rate $\dot{E}_0$ on all layers, dried from SM (green triangles), HS-m (blue circles), HS-p (red squares) and TM (orange stars) layers.

the particle radius); thus, the capillary pressure is stronger on layers of small particles, and these layers undergo more compaction in the second phase of the drying.

2 Final fracture toughness

The previous chapter related the elastic properties of the layers to their porosity p; in the same way, K_c can be related to p (or equivalently, $\phi = 1 - p$). Figure 5.11A presents the fracture toughness K_c^{vic} inferred from indentation tests as a function of packing fraction ϕ. For layers dried from the same initial suspension, fracture toughness increases with increasing packing fraction.

Kendall's model (Kendall, 1988), which was used in chap. 4 as a model for the elasticity of sphere packings, additionally gives the following prediction for the fracture toughness of particle agglomerates:

$$K_c = \frac{31\phi^4}{\sqrt{2r}} W^{1/6} G_c^{5/6} \tag{5.5}$$

with ϕ the packing fraction, r the particle radius, W the interfacial energy and G_c the fracture energy of the bulk material. G_c is expected to be larger than W because fracture typically involves energy loss through dissipative processes. Solid lines on fig. 5.11A represent the prediction of Kendall's model, adjusting G_c for each initial suspension in order to obtain the best fit with the experimental points. The values

for W were those found by fitting Kendall's model for E to the experimental data on Young's modulus.

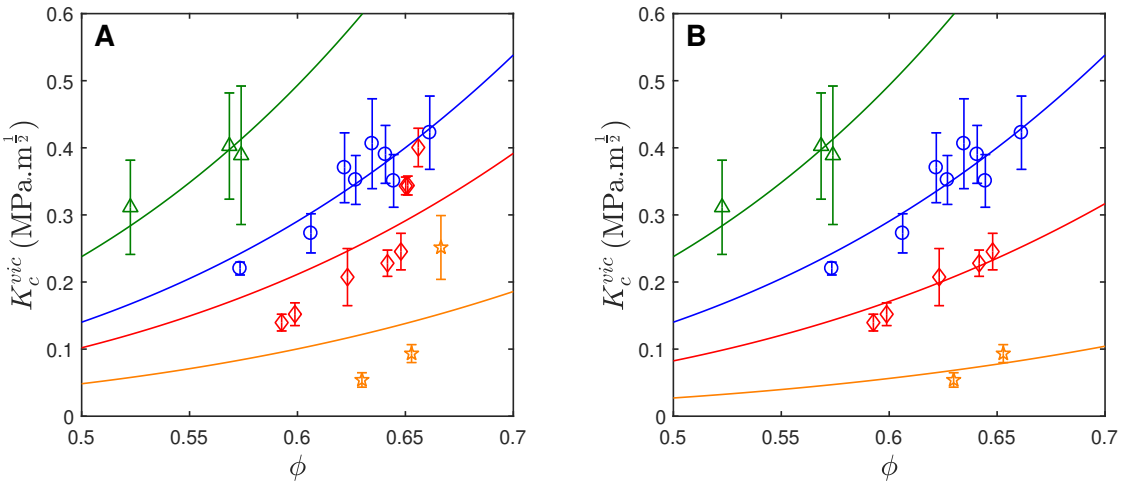

FIGURE 5.11: (A) Fracture toughness for the four suspensions (SM: green triangles, HS-m: blue circles, HS-p: red diamonds, TM: orange stars) as a function of packing fraction ϕ. Solid lines represent the prediction obtained from Kendall's model (eq. 5.5), adjusting G_c in order to obtain the best fit with the experimental data. (B) HS-p layers with $\phi > 0.65$ and TM layers with $\phi > 0.66$ were excluded from the experimental data and new fits were computed, leading to lower values G_c' for the fracture energy.

Layers dried from HS-p and TM suspensions at RH $\leqslant$ 36% (corresponding to $\phi \leqslant 0.65 - 0.66$ on fig. 5.11) show abnormally high fracture toughness, compared to the layers dried from the same suspensions at higher humidities. This might be due to a jamming effect caused by the comparatively high packing fraction of the faster-dried layers: $\phi > 0.65$ for the HS-p layers dried at RH $\leqslant$ 36% and $\phi > 0.66$ for the TM layers dried at the same humidities. This jamming effect would then lead to lower tip penetration during the indentation test. I thus excluded these layers from the experimental data and recomputed Kendall's model, adjusting the fracture energy to obtain the best fit with the restricted data; fig. 5.11B presents the new fitted predictions.

Table 5.1 recalls median particle radius r, polydispersity σ/r and surface energy W and gives the fitted fracture energies G_c (fig. 5.11A) and G_c' (fig. 5.11B) for all Ludox suspensions. As expected, G_c and G_c' are larger than W by a factor 1.5 to 6. The dependence of K_c^{vic} on ϕ is well described by Kendall's model; however, the expected dependence in r is not strong enough to account for the variation in K_c^{vic} between the layers dried from different suspensions, and thus the fitted G_c is strongly dependent on the suspension.

The dependence of fracture energy on the suspension suggests that the chemistry of the suspensions influences the mechanical properties of the layers. Suspensions vary in the amount of sodium they contain, which could play on the behavior of the contacts between the particles.

Suspension	r (nm)	σ/r	W (J/m^2)	G_c (J/m^2)	G_c' (J/m^2)
SM	5.5	0.19	3.2	17.1	17.1
HS-m	8.1	0.14	5	10.4	10.4
HS-p	8.6	0.31	2.5	8	6.2
TM	14.0	0.10	1.7	5	2.5

TABLE 5.1: Particle radius, dispersity, surface energy (inferred from Kendall's model for E), and fracture energy (inferred from Kendall's model for K_c) for the four silica suspensions.

Figures 5.12 and 5.13 respectively present the fracture toughness K_c^{vic} and the Vickers hardness H_v estimated by indentation tests as a function of the evaporation rate for layers dried from each of the four initial suspensions. Fracture toughness increases with increasing drying rate: although fast-dried layers undergo more cracking during the drying process, they are more resistant to fracture once the final, dry state is reached. Thus, the cracking behavior of the layers cannot be explained from their final mechanical properties.

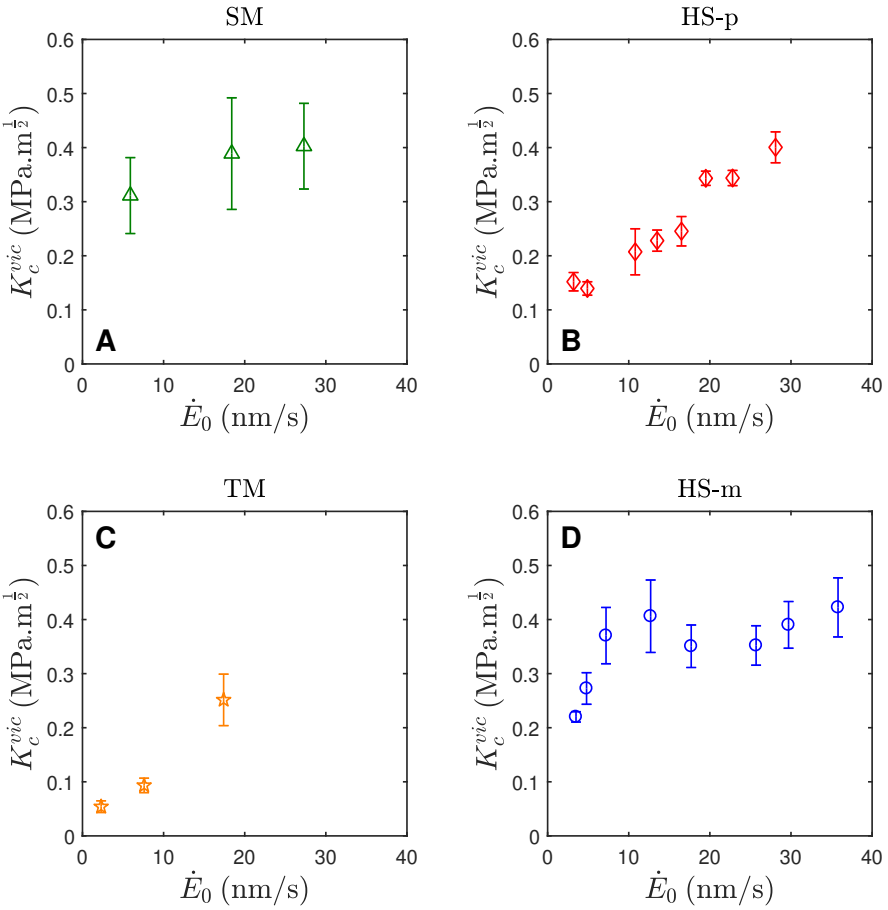

FIGURE 5.12: Fracture toughness as a function of drying rate for (A) SM layers, (B) HS-p layers, (C) TM layers, (D) HS-m layers.

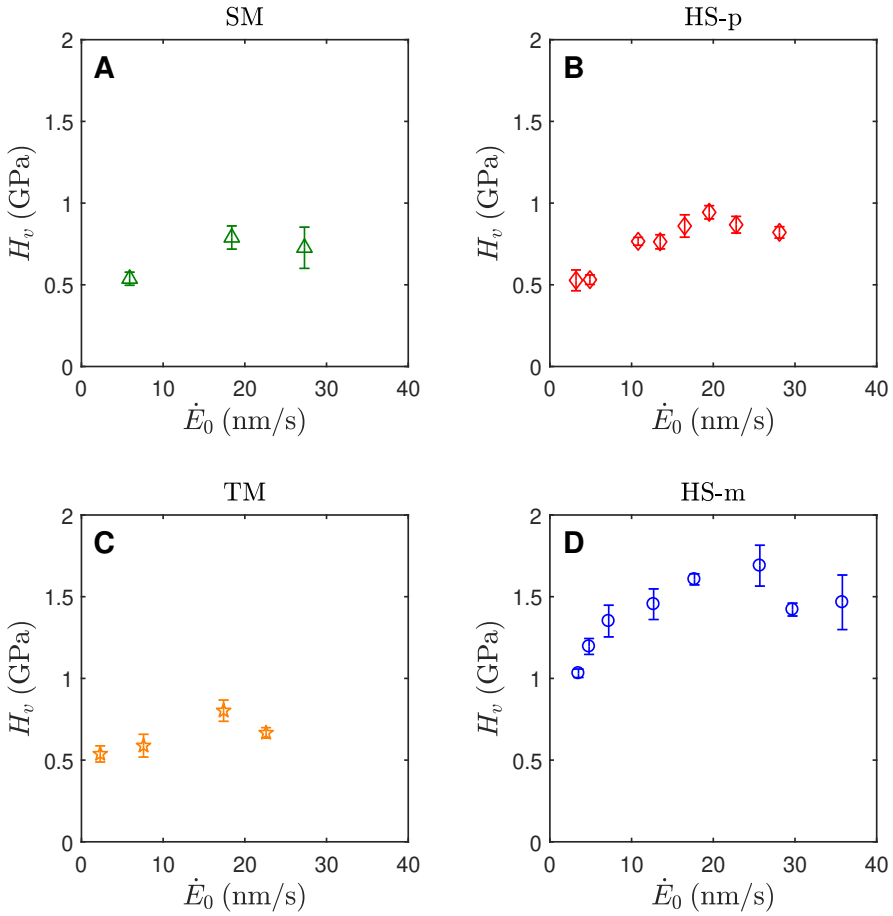

FIGURE 5.13: Vickers hardness as a function of drying rate for (A) SM layers, (B) HS-p layers, (C) TM layers, (D) HS-m layers.

3 Packing fraction at the onset of fracture and desaturation

The analysis of images during drying together with eq. 5.4 allow inferring mass and silica volume fraction at fracture and desaturation. Their values for all layers are given in tables 5.2 (for HS-m experiments), 5.3 (for HS-p experiments), 5.4 (for SM experiments) and 5.5 (for TM experiments). Layers which underwent directional drying (see sec. 3.1) are excluded from the following data, as eq. 5.4 assumes uniform drying of the layer. Moreover, there are no values for the fracture of the HS-p layer dried at RH = 90% as this layer did not crack before the opaque phase.

TABLE 5.2: Mass m and volume fraction of silica ϕ at fracture and desaturation for HS-m layers.

RH_c (%)	m_{frac} (g)	m_{desat} (g)	ϕ_{frac}	ϕ_{desat}
23	14.03	11.87	0.508	0.679
36	14.48	12.03	0.482	0.663
50	14.92	12.05	0.46	0.661
65	15.73	12.62	0.423	0.608
90	16.24	12.55	0.403	0.614
95	16.17	12.77	0.406	0.595

TABLE 5.3: Mass m and volume fraction of silica ϕ at fracture and desaturation for HS-p layers.

RH_c (%)	m_{frac} (g)	m_{desat} (g)	ϕ_{frac}	ϕ_{desat}
36	16.06	13.16	0.422	0.584
50	15.43	13.04	0.449	0.593
65	15.9	12.89	0.429	0.605
80	16.35	13.19	0.411	0.581
90	-	13.64	-	0.550
95	16.99	13.64	0.388	0.549

TABLE 5.4: Mass m and volume fraction of silica ϕ at fracture and desaturation for SM layers.

RH_c (%)	m_{frac} (g)	m_{desat} (g)	ϕ_{frac}	ϕ_{desat}
10	21.5	14.2	0.279	0.512
36	21.5	14.3	0.277	0.505
80	20.8	15.1	0.29	0.467
95	23.4	14.8	0.249	0.478

TABLE 5.5: Mass m and volume fraction of silica ϕ at fracture and desaturation for TM layers.

RH_c (%)	m_{frac} (g)	m_{desat} (g)	ϕ_{frac}	ϕ_{desat}
36	14.5	13	0.496	0.599
80	14.6	13	0.49	0.592
95	15.3	13.4	0.454	0.567

Figure 5.14 presents, for the layers dried from each of the four Ludox suspensions, ϕ_{frac} (diamonds), ϕ_{desat} (circles) and ϕ_{dry} (the final packing fraction measured by hydrostatic weighing; stars). Several observations can be made:

- Layers prepared from the same suspensions tend to fracture and desaturate at lower packing fractions when dried at a lower evaporation rate.
- ϕ_{desat} and ϕ_{dry} are close for all drying experiments, indicating that no significant compaction takes place after the beginning of the opaque phase, *i.e.* once the layer has desaturated.
- The difference $\phi_{desat} - \phi_{frac}$ is larger for SM layers and lower for TM layers, compared to HS layers. Thus, the smaller the particle size, the more compaction takes place between fracture and desaturation. This corroborates the results given in sec. 3.1, which show that compared to HS layers, SM layers have a higher retraction coefficient κ and TM layers a smaller one.

Also notable is the influence of particle size on ϕ_{frac}. Compared to HS layers, the silica volume fraction at first fracture ϕ_{frac} is much lower for SM layers and slightly higher for TM layers. This underlines the difference in stability between the suspensions: suspensions of smaller particles are less stable because of their higher surface energy (see chap. 1). Thus, SM layers (particle radius $r \simeq 5.5\,\text{nm}$) gel at lower concentration and crack earlier during the drying process, as compared to HS ($r \simeq 8\,\text{nm}$) and TM layers ($r \simeq 14\,\text{nm}$).

Finally, ϕ_{frac} and ϕ_{dry} are both increasing functions of $\dot{E}_0$. The previous section underlined that the final fracture toughness, which increases with $\dot{E}_0$ and ϕ_{dry}, cannot explain the crack patterns observed on the layers, as crack density increases with $\dot{E}_0$. In the same way, the crack patterns cannot be explained from a fracture toughness which would only depend on ϕ_{frac}: as ϕ_{frac} increases with $\dot{E}_0$ and $K_c(\phi_{frac})$ would be expected to increase with ϕ_{frac}, $K_c(\phi_{frac})$ would increase with $\dot{E}_0$. Thus the higher crack density of fast-dried layers cannot be explained by a fracture toughness at first fracture $K_c(\phi_{frac})$ only dependent on ϕ_{frac}, and an additional parameter is necessary to understand the cracking behavior of the layers during desiccation.

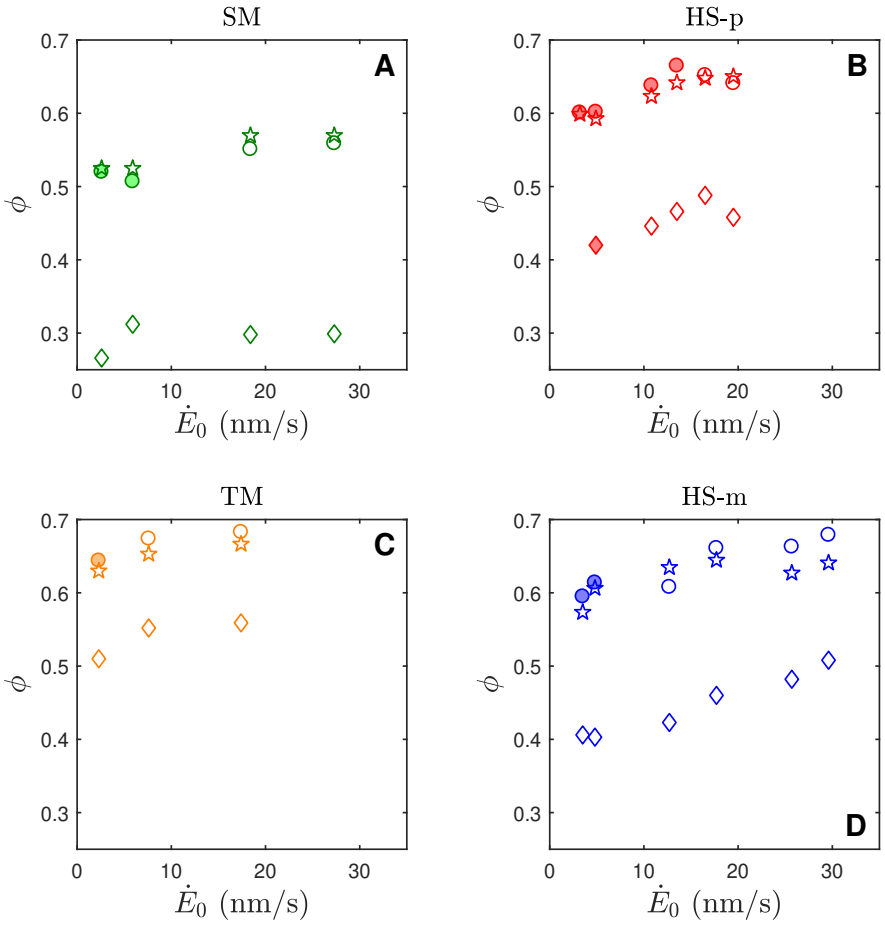

FIGURE 5.14: Packing fraction at the apparition of the first fracture (diamonds), at desaturation (circles) and in the dry final state (stars), as a function of evaporation rate. (A) SM layers; (B) HS-p layers; (C) TM layers; (D) HS-m layers. In some experiments run at high RH, fracture and/or desaturation happened during the quenching period, when RH was set to 10%. The corresponding symbols are represented with solid color.

IV Discussion

Our main control parameter, the evaporation rate $\dot{E}_0$, influences the fracture properties of the layers in different ways:

- decreasing $\dot{E}_0$ increases crack spacing, *i.e.* slowly-dried layers yields less cracking and thus larger morsels;
- decreasing $\dot{E}_0$ decreases the packing fraction at fracture ϕ_{frac}, at desaturation ϕ_{desat} and in the final state ϕ_{dry};

- decreasing $\dot{E}_0$ decreases final fracture toughness K_c^{vic}, *i.e.* slowly-dried layers are less resistant to fracture (despite developing fewer cracks during drying).

Most notably, the evolution of crack spacing with the evaporation rate cannot be explained neither by the final fracture toughness of the layers nor by their packing fraction at fracture ϕ_{frac}: faster-dried layers have lower crack spacing, despite a higher ϕ_{frac}. In the following section, I discuss the influence of $\dot{E}_0$ on the processes of geometrical and chemical consolidation in order to explain the evolution of fracture properties with the evaporation rate.

1 Two time scales for consolidation

As the suspension dries, two different processes drive the evolution of the mechanical properties of the saturated layer:

- Geometrical consolidation: evaporation removes water from of the system, compacting the particles. The characteristic time for the drying process is inversely proportional to the evaporation rate $\dot{E}_0$.
- Chemical consolidation: through condensation reactions, siloxane bonds form between silica particles in contact, making contacts stiffer (Vigil et al., 1994). The characteristic time for the formation of chemical bonds is related to the chemistry of the system and is independent of the evaporation rate.

All layers dried from a given Ludox suspension have the same initial thickness h_0 ($h_0 \simeq 5$ mm for TM, HS-m and HS-p layers and $h_0 \simeq 7$ mm for SM layers). A rescaled, dimensionless time can thus be defined:

$$t^* = \frac{\dot{E}_0}{h_0} \frac{\rho_w}{\rho_{ludox}} t \tag{5.6}$$

For a given Ludox suspension, t^* is a linear function of t and $\dot{E}_0$ only. Figure 5.15 represents the evolution of (A) mass and (B) packing fraction as a function of this rescaled time, for three layers dried from HS-m suspension, at RH = 23% (solid red line), RH = 65% (green dash-dot line), and RH = 95% (blue dotted line). Vertical bars denote the apparition of the first crack and circular dots denote the opacification (and thus desaturation) of the layers.

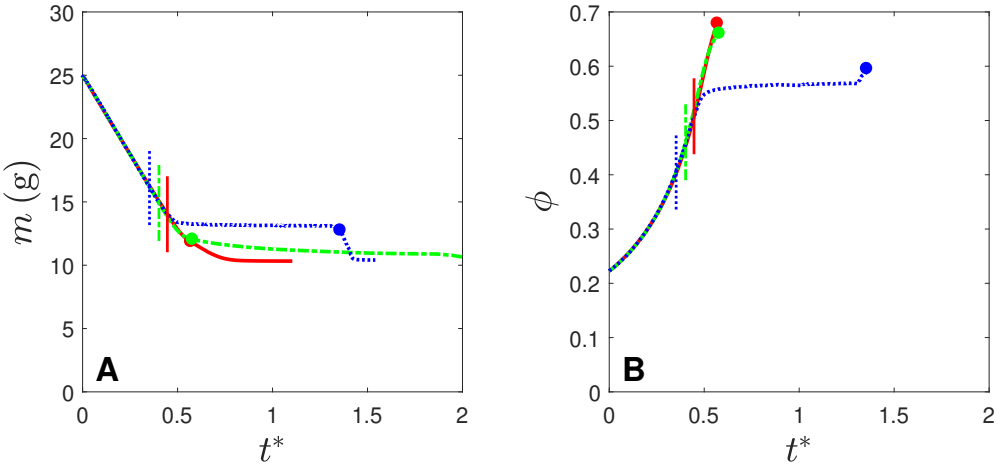

FIGURE 5.15: Evolution of (A) mass and (B) packing fraction as a function of rescaled time t^* for HS-m layers dried at RH = 23% (solid red line), RH = 65% (green dash-dot line), and RH = 95% (blue dotted line). Vertical bars denote the apparition of the first crack, which happens towards the end of the constant rate period, when the mass loss $m - m_0$ is still proportional to t^*. Circular dots denote the opacification (and thus desaturation) of the layers. Once the layers are opaque, packing fraction cannot be computed from the mass curves anymore as eq. 5.4 is only valid for saturated layers.

During the first stage of the drying (constant rate period, $\dot{E}(t) = \dot{E}_0$), all layers from a given suspension dry at the same rate with respect to t^*, since their mass can be expressed as

$$m(t^*) = (1 - t^*)m_0 \tag{5.7}$$

with no dependence on $\dot{E}_0$ nor RH. Moreover, eq. 5.4 gives an expression of the volume concentration ϕ as a function of sample mass m in saturated layers; thus ϕ is also a simple function of t^* during the constant rate period:

$$\phi = \frac{m_{sil}/\rho_{sil}}{((1 - t^*)m_0 - m_{sil})/\rho_{H_2O} + m_{sil}/\rho_{sil}} \tag{5.8}$$

During the falling rate period, m and ϕ still increase with t^*, but they also depend on RH, as layers dried at higher humidity retain more water in their pores.

2 Crack spacing

The influence of $\dot{E}_0$ on the relative rates of stress build-up and chemical consolidation explains why crack spacing is larger in slowly dried layers. During the drying

process, the mean pre-stress σ_0 in the layer scales proportionally with time, according to Chekchaki and Lazarus, 2013:

$$\frac{\mathrm{d}\sigma_0}{\mathrm{d}t} = \alpha\frac{\dot{\mathrm{E}}}{\mathrm{S}h} \quad \text{and thus} \quad \frac{\mathrm{d}\sigma_0}{\mathrm{d}t^*} = \frac{\alpha h_0 \rho_{ludox}}{\mathrm{S}h\rho_w} \tag{5.9}$$

with h the layer thickness, α the Biot-Willis coefficient and S the storage coefficient. Assuming the poroelastic coefficients only depend on the layer structure (*i.e.* its compacity ϕ), the increase in pre-stress only depends on the reduced time t^*, for all layers dried from the same suspension. Thus, at a given reduced time t^*, all layers dried from the same suspension are under the same pre-stress σ_0. Layers dried at higher humidities, however, will be older in actual time t and the formation of covalent interparticle bonds through condensation reactions will have further progressed. These layers will thus be more resistant to fracture and break into larger morsels.

Note that the same argument explains why layers dried with a holding period (Piroird et al., 2016) also exhibit a larger crack spacing, compared to continuously dried layers (see fig. 3.6 in chap. 3). During the holding period, the build-up of stresses is interrupted, while chemical bonds keep forming between aggregated particles, and the resultant layers are more resistant to the stresses arising during the drying process.

3 Packing fraction at desaturation and in the final state

The interplay of two timescales, one related to the formation of chemical bonds between the particles, and the other governing the build-up of stresses, explains why ϕ_{desat} and ϕ_{dry} decrease with decreasing drying rate. As the suspension gels, menisci form and deepen between the particles at the interface. The corresponding capillary pressure P_{cap} exerts an increasing stress on the solid particle network, which reacts by an increase in ϕ through plastic deformation. The yield strength of a layer depends on both the structure of the particle network (*i.e.* its packing fraction ϕ) and the degree of chemical sintering between the particles (itself a function of time t), and consolidation will proceed as long as $\sigma_\mathrm{Y}(\phi, t) \leqslant \mathrm{P}_{cap}$. However, the menisci at the surface can only sustain a limited pressure differential before the air-water interface depins from the surface particles and recedes through the layer; this sets a maximal capillary pressure $\mathrm{P}_{cap,max}$. Once $\sigma_\mathrm{Y}(\phi, t)$ reaches $\mathrm{P}_{cap,max}$, desaturation will begin.

As the drying proceeds, σ_Y increases from both structural consolidation (increase in ϕ) as well as chemical consolidation (formation of siloxane bonds). Thus, $\sigma_\mathrm{Y}(\phi, t)$

is an increasing function of both ϕ and t. Drying layers desaturate when σ_Y reaches the critical value P_{cap}, independently of the drying rate $\dot{E}_0$. However, slowly-dried layers will desaturate at a higher time t and thus at a lower packing fraction ϕ. Hence ϕ_{desat} decreases with decreasing $\dot{E}_0$.

4 Fracture toughness in the final state

Once desaturation has begun, $P_{cap,max} \leqslant \sigma_Y(\phi, t)$: the capillary pressure cannot cause plastic deformation of the packing anymore and the driving force for the compaction of the particles has disappeared. Thus ϕ stops increasing, and $\phi_{dry} = \phi_{desat}$, as shown on fig. 5.14.

Even in the absence of geometrical consolidation, mechanical properties such as the Young's modulus, the yield strength, or the fracture toughness keep increasing as chemical consolidation is still in progress. At long timescales, however, chemical consolidation also stops as the formation of siloxane bonds between the particles reaches equilibrium. The mechanical properties of the dry layers then only depend on their packing fraction ϕ_{dry}. Thus fast-dried layers, which are more compact at desaturation and in their final state, also have a higher fracture toughness K_c, despite undergoing more cracking during the desiccation process.

Conclusion

As a colloidal layer dries, the liquid suspension turns into a gel which gradually consolidates. The evaporation rate $\dot{E}_0$ has a direct influence on the rate of stress build-up, as well as on the rate of geometrical consolidation (*i.e.* the increase in packing fraction as a response to the drying stresses). However, the mechanical properties of the layer also evolve through chemical consolidation (*i.e.* the formation of covalent bonds between the particles), at a rate which is independent of $\dot{E}_0$. Thus decreasing $\dot{E}_0$ allows chemical consolidation to progress faster relatively to geometrical consolidation and to the build-up of stresses. This explains why slowly-dried layers undergo less cracking during the drying process, but yield a more porous solid which is less resistant to fracture.

Another way to play on the relative rates of geometrical and chemical consolidation would be to introduce a holding period during the drying process, once the layer has gelled. Longer holding periods would allow higher chemical consolidation, while geometrical consolidation and stress evolution would be interrupted. The corresponding experiments should yield layers with higher crack spacings. The

rate of chemical consolidation could also be inferred from the in-situ measurement of mechanical properties during the holding period, and these mechanical properties could be correlated to the fracture patterns.

Conclusion

Summary

In this work, I prepared dry colloidal layers from colloidal silica suspensions and I used a variety of experimental methods (AFM, SAXS, ultrasound propagation and Vickers indentation) to characterize their structural and mechanical properties, as well as the dependence of these properties on the evaporation rate. The experiments were reproduced using four suspensions with different particle sizes and dispersities.

The evaporation rate plays on the structure of the layers through particle aggregation. In slower-dried layers, particles have more time to aggregate, and the drying process yields a more porous solid. Sufficiently monodisperse suspensions exhibit surface ordering at high evaporation rates. At lower rates, particle aggregation can preclude the formation of a crystalline surface arrangement. SAXS measurements on a suspension undergoing a holding period confirm aggregate formation in concentrated liquid suspensions. SAXS measurements on the dry colloidal layers reveal that their structure keeps evolving well after the end of the drying.

Using ultrasound measurements, I determined the elastic properties of the colloidal silica layers. The experimentally measured bulk and shear moduli were in agreement with the self-consistent homogenization scheme; in addition, the measured Young's moduli agreed with Kendall's model on the elasticity of sphere packings. However, both models required fitting with a physical parameter: respectively the stiffness of the particles themselves, or their surface energy. These physical parameters are not directly accessible and vary for the four different suspensions. The chemical composition of the suspensions probably plays on the elasticity of the resulting dry layers. Moreover, the suspensions contain varying amounts of sodium, which modifies the structure of the silica network. As the sodium is concentrated at the surface of the particles, it could have a strong influence on the particles contact properties.

The evaporation rate plays on the crack patterns formed during the desiccation process, as well as on the fracture properties of the final dry material. Fast-dried

layers develop more desiccation cracks, but yield a solid material that is more resistant to fracture. This happens because the rate of stress build-up in the layer and the associated geometrical consolidation depend on the evaporation rate, whereas chemical consolidation, which also influences the mechanical properties of the drying layer, is independent of the evaporation rate. Finally, this interplay between the rates of chemical and geometrical consolidation explain the effect of a holding period on crack patterns: during the holding period, evaporation is interrupted while chemical consolidation continues and makes the drying layer more resistant to fracture.

Perspectives

Additional SAXS studies could provide a better understanding of the structural properties of the layers. Holding period experiments combined with SAXS measurements on the form factor of the aggregates would allow a quantitative description of the aggregation dynamics of the suspension.

Another avenue for further research would be to prepare colloidal layers by the same protocol, but using suspensions with controlled chemistry. Counter-ion concentration may be tuned by washing and filtrating commercial suspensions, or by preparing the suspensions *in-house*. In addition, preparing the suspensions *in-house* would allow better control of particle dispersity, which impacts the structural properties of the layers. Finally, the study may be repeated on systems such as hard latex suspensions, whose chemistry is easier to control.

Future work concerning fracture in colloidal silica layers could also investigate the dynamics of chemical consolidation. The rate of chemical consolidation (*i.e.* the rate of siloxane bond formation between the particles) concerns the evolution of the mechanical properties of the layers. Following the evolution of these mechanical properties during the desiccation process, or during holding periods introduced at varying concentrations, may thus shed light on the chemical consolidation process. The ultrasound techniques used in chap. 3 are poorly adapted to in-situ measurement of the elastic moduli, as the drying layers tend to delaminate from the substrate, preventing the propagation of the sound waves. Indentation may thus prove a more convenient method to estimate the Young's modulus of the layers. Additionally, it can also yield their indentation fracture toughness. The mechanical properties measured at the instant of crack opening may then be correlated to the mechanical loadings measured by beam deflection. This would provide a means to evaluate theoretical models on crack spacing in drying layers.

Appendix A

SAXS measurements

This appendix outlines the workings of a small-angle X-ray scattering (SAXS) experiment and presents the detailed methods used for our measurements.

I Methods

SAXS experiments use a monochromatic, collimated X-ray beam to measure the material inhomogeneities at the particle scale. As the beam goes through the sample, most photons remain undeflected, but some of them are scattered as a result of differences in electron density. A detector placed behind the sample measures the scattered intensity I as a function of the scattering vector, defined as $\vec{q} = \vec{k} - \vec{k}_0$, with $\vec{k}_0$ the wavevector of the incident beam and $\vec{k}$ the wavevector of the scattered beam (see fig. A.1). For an isotropic sample, such as an amorphous or polycrystalline solid, the scattered intensity is rotationally invariant, and only depends on $q = |\vec{q}|$, which can be expressed as

$$q = \frac{4\pi sin(\theta)}{\lambda} \tag{A.1}$$

with 2θ the scattering angle and λ the wavelength of the beam.

The intensity $I(q_0)$ diffracted at a given q_0 gives information on the material structure at a scale $d_0 = \frac{2\pi}{q_0}$. Small-angle X-ray scattering probes low q values (corresponding to $\theta < 0.1$) and provides information concerning comparatively larger structures ($d_0 \gg \lambda \sim 1$ Å). It is thus particularly useful in probing colloidal systems with particle sizes ranging between 1 and 100 nm in diameter. On the beamline used in this study, I could measure q ranging $q = 0.1 - 1.6\,\mathrm{nm}^{-1}$, corresponding to length scales $d = 4 - 60$ nm.

The intensity I scattered by an assembly of identical *monodisperse* particles can be written as

$$I(q) \sim P(q)S(q) \tag{A.2}$$

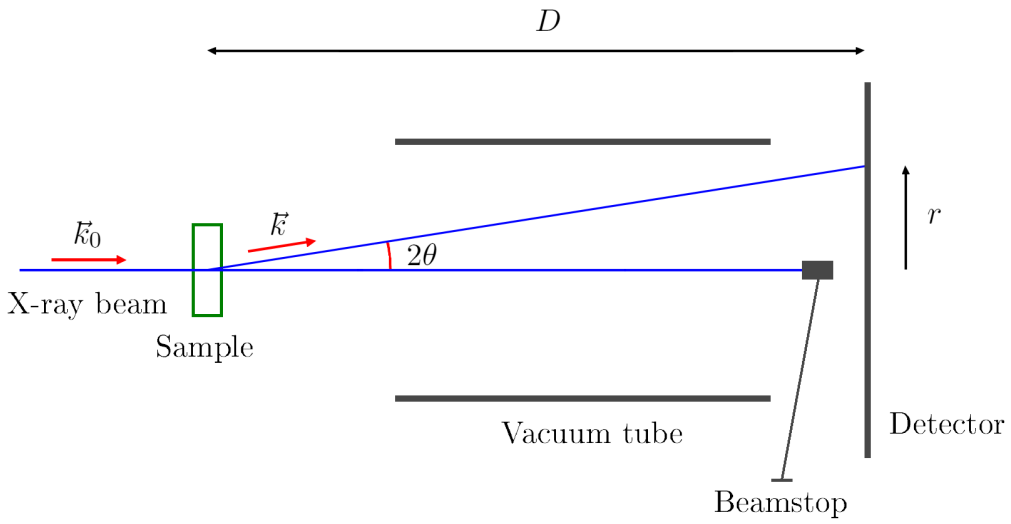

FIGURE A.1: Basic setup of a SAXS experiment

where the form factor $P(q)$ provides information about particle shape and size and the structure factor $S(q)$ provides information about correlations in particle positions.

For polydisperse systems, the previous expression still holds; however, $S(q)$ represents an effective structure factor. $P(q)$ then depends on particle size distribution. Measurements of form factors for monodisperse and polydisperse suspensions involve dilute suspensions. In dilute suspensions, particles are separated, reducing (if not eliminating) correlations in particle positioning. Thus, one can assume $S(q) \sim 1$ and therefore $I(q) \sim P(q)$.

For a polydisperse suspension of spherical particles, P is the weighted sum of individual form factors over the distribution of particle radii (Pedersen, 1997):

$$P(q) = \int_0^\infty P_S(q, r) D(r)\, dr \tag{A.3}$$

where $P_S(q, r)$ is the form factor for spheres of radius r and $D(r)$ is the proportion of particles with radius between r and $r + dr$.

II Experimental setup

An X-ray gun with a copper target provides X-rays with a wavelength $\lambda = 0.154\,\text{nm}$ for the experiment. Scattered intensity was measured using a Pilatus Dectris 200K

detector (pixel size l_{pix} = 172 μm). Raw data were obtained as two-dimensional images (photon counts per pixel). As the detector is made of two rectangular sensors separated by a blind horizontal band, two images were taken for each measurement with the detector vertically shifted by 40 pixels, and combined afterwards. A beamstop was placed before the detector to cut the transmitted (non scattered, $\vec{k} = \vec{k_0}$) beam and equipped with a photodiode to measure transmitted beam intensity.

1 Distance calibration

Figure A.2 depicts a typical diffraction pattern, here obtained on a microcrystalline calibration sample; darker areas correspond to stronger scattered intensity I(q). On the diffraction pattern recorded on the detector, the circle with the radius r corresponds to a scattering vector

$$q = \frac{4\pi}{\lambda} \sin(\frac{1}{2} \arctan(\frac{r}{\mathrm{D}})) \tag{A.4}$$

The diffraction pattern for a crystalline material with lattice parameter a will exhibit a narrow Bragg peak at $q = \frac{2\pi}{a}$. The distance D between the samples and the detector was thus determined for each sample holder using two calibration powders in capillary tubes: lead dithiolate (lattice parameter 5 nm) and LI34 (lattice parameters 4.94 nm, 5.7 nm and 9.87 nm).

We used the same setup with both solid and liquid samples, with D = 1.2 ± 0.1 m and $r < 6$ cm so that $\theta < 0.1$. We measured q in the range $q = 0.1 - 1.6$ nm^{-1}, corresponding to length scales $d = 4 - 60$ nm.

2 Liquid samples

In order to measure the form factor of the initial suspension, we prepared dilute Ludox suspensions (silica volume fraction ϕ_v = 0.45%) in millipore water. 40mN NaCl was added to reduce electrostatic interactions between the particles.

Glass capillary tubes (diameter 1 mm, wall thickness 0.1 mm) were filled with dilute suspension and measured with acquisition time t_{acq} = 7200 s. A background measured on a tube filled with 40 mM NaCl solution was subsequently substracted from other liquid measurements.

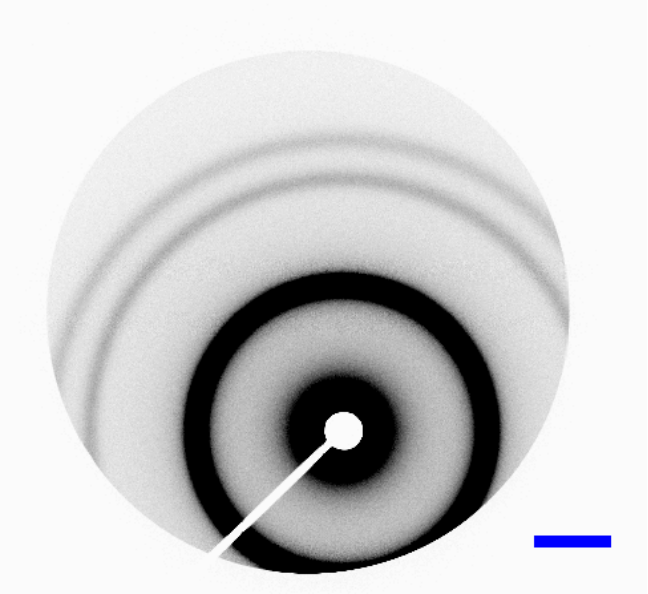

FIGURE A.2: Raw data on LI34 calibration sample (scale bar: 1 cm). The three rings, which represent maxima in the measured intensity I(q), correspond to the three lattice spacings (larger rings correspond to smaller spacings). As the scattered beam travels through a cylindrical vacuum tube, the imaged area is circular. The shadow of the beamstop and its supporting rod is clearly visible.

3 Solid samples

Solid samples were mounted on the sample holder using metallic tape. The sample to detector distance using this setup was found to be equal to the one using the capillary holder for liquid samples: D = 1.208 ± 0.002 m.

4 Data processing

The images taken on calibration powders (see fig. A.2 for a representative example) showed rings (corresponding to I(q) maxima) and were used to determine the center of the diffraction pattern. A mask was applied on shadowed areas and the mean intensity for each radius r was calculated on the unmasked areas, rounding r to integer pixel values. Measured values of r are thus discrete with step $\delta r = l_{pix}$; as q is proportional to r, that is

$$q \simeq \frac{2\pi}{\lambda} \frac{r}{\mathrm{D}} \tag{A.5}$$

with less than 0.5% error on our setup, values of q are evenly sampled with increment

$$\delta q = \frac{2\pi}{\lambda}\frac{l_{pix}}{\mathrm{D}} = 5.8 \cdot 10^{-3}\,\mathrm{nm}^{-1}. \tag{A.6}$$

An important source of loss of resolution is the finite width of the X-ray beam used to probe the samples, which introduces smearing of the diffraction pattern. The actual diffraction pattern $\mathrm{I}(\vec{r})$ measured at the detector can be written as a convolution product,

$$\mathrm{I}(\vec{r}) = \mathrm{I}_{beam}(\vec{r}) * \mathrm{I}_0(\vec{r}) \tag{A.7}$$

where $\mathrm{I}_{beam}(\vec{r})$ is the intensity profile of the incoming beam and $\mathrm{I}_0(\vec{r})$ is the *ideal* diffraction pattern that would be obtained using an incoming beam with zero width. The diffraction pattern measured on the LI34 calibration sample (see A.2) then allows estimating the width of the incoming beam. Since the grain size in the polycrystalline sample is much larger than the wavelength of the x-rays, the diffraction rings in $\mathrm{I}_0(\vec{r})$ have negligible width, and the width of the rings in the measured pattern $\mathrm{I}(\vec{r})$ equals the width of the beam. The scattered intensity as a function of radius $\mathrm{I}(r)$ was computed from the diffraction pattern measured on LI34, and a gaussian fit on the first intensity peak (corresponding to the first diffraction ring) yielded the full width at half maximum of the X-ray beam: $w_{beam} = 1.85\,\mathrm{mm}$.

III Results

1 Transmission measurements

The beamstop was equipped with a photodiode enabling the measurement of the transmitted beam $\mathrm{I_T}$ as well as the measurement of the incident intensity $\mathrm{I_{T,0}}$. The transmission $\mathrm{T} = \frac{\mathrm{I_T}}{\mathrm{I_{T,0}}}$ can thus be computed. However, solid samples (especially those of thickness 2 mm) were found to be strongly absorbent. Moreover, the X-ray source showed fluctuations in output intensity, possibly because of variations in temperature or vacuum quality.

Data on transmissions were thus very noisy and could not be exploited. Hence, data presented in this work were either normalized by maximal intensity or by intensity at a specific q_0.

2 Form factors

The form factor for a monodisperse assembly of spheres of radius R can be written (Feigin and Svergun, 1987) as

$$P_R(q) \sim \frac{(sin(qR) - qRcos(qR))^2}{(qR)^6} \tag{A.8}$$

For a polydisperse assembly, assuming the particle sizes follow a log-normal distribution, that is

$$D_{R_m,\sigma}(r) = \frac{1}{\sqrt{2\pi}r\sigma} \exp(-\frac{(\ln(r) - \ln(R_m))^2}{2\sigma^2}) \tag{A.9}$$

with R_m the mean sphere radius and σ the polydispersity (standard deviation of particle radius), the corresponding form factor can be written, using eq. A.3:

$$P_{R_m,\sigma}(q) = \int_0^\infty P_r(q) D_{R_m,\sigma}(r)\, dr \tag{A.10}$$

Intensity profiles I(q) acquired on dilute suspensions were fitted to a theoretical form factor $P_{R_m,\sigma,smeared}(q)$, defined as the convolution of a lognormal distribution $P_{R_m,\sigma}(q)$ with a gaussian distribution of full width at half maximum w_{beam}, in order to take into account the smearing of the measured intensity profile due to finite beam width. The parameters R_m and σ were adjusted in order to minimize $|\log(I(q)) - \log(P_{R_m,\sigma,smeared}(q))|^2$ on $q = 0.1 - 1.4$ nm^{-1}. Figure A.3 presents the measured and fitted form factors on the four Ludox suspensions studied in this work. Results for all Ludox batches are presented in table A.1.

Suspension	Batch number	R_m (nm)	σ/R_m
SM	MKBP6397V	5.5	0.19
HS-m	BCBK7778V	8.1	0.14
HS-p	STBF8427V	8.6	0.31
TM	05105EE	14.0	0.10

TABLE A.1: Median particle radius and relative polydispersity for the four Ludox batches used in this study, obtained by fitting the measured form factors to a lognormal distribution.

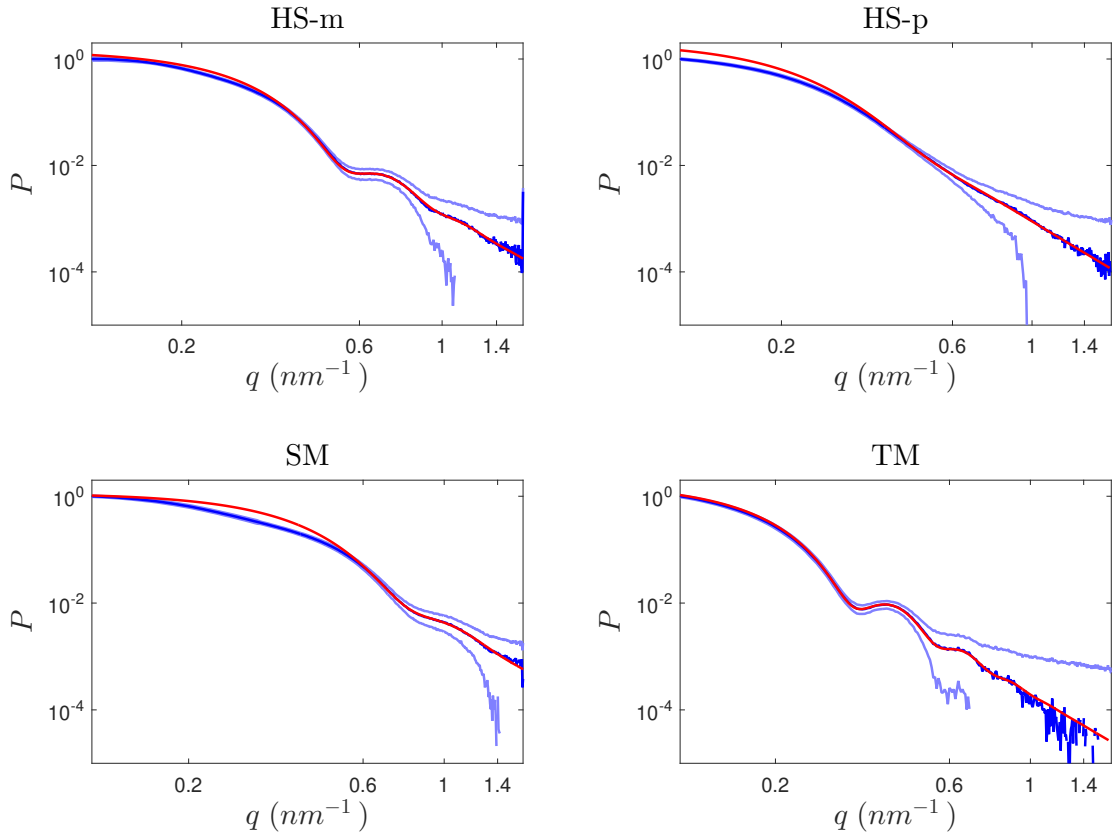

FIGURE A.3: Measured form factor (blue) and fitted form factor (red) on the four Ludox batches used in this thesis. Light blue lines correspond to the uncertainty (standard deviation) on the measured signal.

Bibliography

Alexander, G. B. (1954). "Process for producing sols of 5-8 millimicron silica particles, and product". Pat. US2750345A.

Allain, C. and Limat, L. (1995). "Regular patterns of cracks formed by directional drying of a colloidal suspension". In: *Physical Review Letters* 74, pp. 2981–2984.

Allen, L. H. and Matijevic, E. (1969). "Stability of colloidal silica: I. Effect of simple electrolytes". In: *Journal of Colloid and Interface Science* 31 (3), pp. 287–296.

— (1970). "Stability of colloidal silica: II. Ion exchange". In: *Journal of Colloid and Interface Science* 33 (3), pp. 420–429.

Ashkin, D., Haber, R. A., and Wachtman, J. B. (1990). "Elastic Properties of Porous Silica Derived from Colloidal Gels". In: *Journal of the American Ceramic Society* 73.11, pp. 3376–3381.

Barlet, M. et al. (2015). "Hardness and toughness of sodium borosilicate glasses via Vickers indentations". In: *Journal of Non-Crystalline Solids* 417-418, pp. 66–79.

Biot, M. A. (1941). "General theory of three-dimensional consolidation". In: *Journal of Applied Physics* 12, pp. 155–164.

— (1962). "Mechanics of Deformation and Acoustic Propagation in Porous Media". In: *Journal of Applied Physics* 33, pp. 1482–1498.

Birk-Braun, N. et al. (2017). "Generation of strength in a drying film: How fracture toughness depends on dispersion properties". In: *Physical Review E* 95 (2), p. 022610.

de Boer, J. H. (1936). "The influence of van der Waals' forces and primary bonds on binding energy, strength and orientation, with special reference to some artificial resins". In: *Transactions of the Faraday Society* 32, pp. 10–37.

Boulogne, F., Pauchard, L., and Giorgiutti-Dauphiné, F. (2012). "Effect of a non-volatile cosolvent on crack patterns induced by desiccation of a colloidal gel". In: *Soft Matter* 8 (32), pp. 8505–8510.

Boulogne, F., Giorgiutti-Dauphiné, F., and Pauchard, L. (2014). "How to Reduce the Crack Density in Drying Colloidal Material?" In: *Oil Gas Sci. Technol. – Rev. IFP Energies nouvelles* 69.3, pp. 397–404.

— (2015). "Surface patterns in drying films of silica colloidal dispersions". In: *Soft Matter* 11.1, pp. 102–108.

Brinker, C. and Scherer, G. (1990). *Sol-Gel Science*. Academic Press.

Brisard, S., Dormieux, L., and Kondo, D. (2010a). "Hashin–Shtrikman bounds on the bulk modulus of a nanocomposite with spherical inclusions and interface effects". In: *Computational Materials Science* 48.3, pp. 589–596.

— (2010b). "Hashin–Shtrikman bounds on the shear modulus of a nanocomposite with spherical inclusions and interface effects". In: *Computational Materials Science* 50.2, pp. 403–410.

Bruggeman, D. A. G. (1935). "Berechnung verschiedener physikalischer Konstanten von heterogenen Substanzen. I. Dielektrizitätskonstanten und Leitfähigkeiten der Mischkörper aus isotropen Substanzen". In: *Annalen der Physik* 416.7, pp. 636–664.

Budiansky, B. (1965). "On the elastic moduli of some heterogeneous materials". In: *Journal of the Mechanics and Physics of Solids* 13.4, pp. 223–227.

Cabane, B. et al. (2016). "Hiding in Plain View: Colloidal Self-Assembly from Polydisperse Populations". In: *Physical Review Letters* 116 (20), p. 208001.

Caddock, B. D. and Hull, D. (2002). "Influence of humidity on the cracking patterns formed during the drying of sol-gel drops". In: *Journal of Materials Science* 37.4, pp. 825–834.

Chan, T. F. and Vese, L. A. (2001). "Active contours without edges". In: *IEEE Transactions on Image Processing* 10.2, pp. 266–277.

Chekchaki, M. (2011). "Détermination théorique et expérimentale des contraintes mécaniques induisant les fractures lors du séchage de suspensions colloïdales". PhD thesis. Université Pierre et Marie Curie (Paris, France).

Chekchaki, M. and Lazarus, V. (2013). "Mechanical stresses induced by evaporation in consolidated colloidal suspensions of hard particles. Poroelasticity theory versus experiments". In: *Transport in Porous Media* 100.1, pp. 143–157.

Chekchaki, M., Frelat, J., and Lazarus, V. (2011). "Analytical and 3D finite element study of the deflection of an elastic cantilever bilayer plate". In: *Transactions of the ASME. Journal of Applied Mechanics* 78.1, p. 011008.

Chiu, R. C., Garino, T. J., and Cima, M. J. (1993). "Drying of Granular Ceramic Films: I, Effect of Processing Variables on Cracking Behavior". In: *Journal of the American Ceramic Society* 76 (9), pp. 2257–2264.

Cook, R. F. and Pharr, G. M. (1990). "Direct Observation and Analysis of Indentation Cracking in Glasses and Ceramics". In: *Journal of the American Ceramic Society* 73 (4), pp. 787–817.

Corning (2003). *HPFS Fused Silica Standard Grade*. URL: http://www.unitedlens.com/pdf/hpfs_fused_silica_standard_grade.pdf.

Coussot, P. (2000). "Scaling approach of the convective drying of a porous medium". In: *The European Physical Journal B* 15.3, pp. 557–566.

Cowin, S. C. (1999). "Bone poroelasticity". In: *Journal of Biomechanics* 32.3, pp. 217–238.

Deegan, R. D. et al. (1997). "Capillary flow as the cause of ring stains from dried liquid drops". In: *Nature* 389, pp. 827–829.

Depasse, J. and Watillon, A. (1970). "The stability of amorphous colloidal silica". In: *Journal of Colloid and Interface Science* 33 (3), pp. 430–438.

Derjaguin, B. and Landau, L. D. (1941). "Theory of the Stability of Strongly Charged Lyophobic Sols and of the Adhesion of Strongly Charged Particles in Solutions of Electrolytes". In: *Acta Physicochimica U.R.S.S.* 14, pp. 633–662.

Dormieux, L., Kondo, D., and Ulm, F.-J. (2006). *Microporomechanics*. Wiley.

Dutta, J. and Hofmann, H. (2004). "Self Organization of Colloidal Nanoparticles". In: *Encyclopedia of Nanoscience & Nanotechnology*. Vol. 9. American Scientific Publishers, pp. 617–640.

Eshelby, J. D. (1957). "The determination of the elastic field of an ellipsoidal inclusion, and related problems". In: *Proceedings of the Royal Society of London A: Mathematical, Physical and Engineering Sciences* 241, pp. 376–396.

Feigin, L. A. and Svergun, D. I. (1987). *Structure Analysis by Small-Angle X-Ray and Neutron Scattering*. Plenum Press.

Fennell Evans, D. and Wennerstrom, H. (1994). *The Colloidal Domain*. Wiley-VCH.

Gauthier, G., Lazarus, V., and Pauchard, L. (2007). "Alternating crack propagation during directional drying". In: *Langmuir* 23, pp. 4715–4718.

— (2010). "Shrinkage star-shaped cracks: Explaining the transition from 90 degrees to 120 degrees". In: *EPL (Europhysics Letters)* 89.2, p. 26002.

Giorgiutti-Dauphiné, F. and Pauchard, L. (2016). "Painting cracks: A way to investigate the pictorial matter". In: *Journal of Applied Physics* 120.6, p. 065107.

Giuseppe, E. et al. (2012). "Rheological and mechanical properties of silica colloids: from Newtonian liquid to brittle behaviour". In: *Rheologica Acta* 51.5, pp. 451–465.

Goehring, L. et al. (2015). *Desiccation cracks and their patterns: Formation and modelling in Science and Nature*. Wiley.

Goehring, L., Clegg, W. J., and Routh, A. F. (2013). "Plasticity and Fracture in Drying Colloidal Films". In: *Physical Review Letters* 110.2, p. 024301.

Greaves, G. N. et al. (2011). "Poisson's ratio and modern materials". In: *Nature Materials* 10.11, pp. 823–837.

Griffith, A. A. (1921). "VI. The phenomena of rupture and flow in solids". In: *Philosophical Transactions of the Royal Society of London A: Mathematical, Physical and Engineering Sciences* 221.582-593, pp. 163–198.

Groisman, A. and Kaplan, E. (1994). "An Experimental Study of Cracking Induced by Desiccation". In: *EPL (Europhysics Letters)* 25.6, p. 415.

Haines, W. B. (1930). "Studies in the physical properties of soil. V. The hysteresis effect in capillary properties, and the modes of moisture distribution associated therewith". In: *The Journal of Agricultural Science* 20.1, pp. 97–116.

Hamaker, H. C. (1937). "The London – van der Waals attraction between spherical particles". In: *Physica* 4.10, pp. 1058–1072.

Hill, R. (1965). "A self-consistent mechanics of composite materials". In: *Journal of the Mechanics and Physics of Solids* 13.4, pp. 213–222.

— (1967). "The essential structure of constitutive laws for metal composites and polycrystals". In: *Journal of the Mechanics and Physics of Solids* 15.2, pp. 79–95.

Hunter, R. J. (1989). *Foundations of Colloid Science*. Oxford University Press.

Iler, R. (1979). *The Chemistry of Silica*. Wiley.

Irwin, G. R. (1957). "Analysis of stresses and strains near the end of a crack traversing a plate". In: *Journal of Applied Mechanics* 24, pp. 361–364.

Israelachvili, J. N. (2011). *Intermolecular and Surface Forces*. 3rd ed. Elsevier.

Jernot, J. P., Coster, M., and Chermant, J. L. (1982). "Model to Describe the Elastic Modulus of Sintered Materials". In: *Physica Status Solidi (a)* 72.1, pp. 325–332.

Johnson, K. L., Kendall, K., and Roberts, A. D. (1971). "Surface energy and the contact of elastic solids". In: *Proceedings of the Royal Society A* 324, pp. 301–313.

Kendall, K. (1988). "Agglomerate strength". In: *Powder Metallurgy* 31 (1), pp. 28–31.

— (2001). *Molecular Adhesion and Its Applications*. Springer US.

Kendall, K., Alford, N. M., and Birchall, J. D. (1987a). "A new method for measuring the surface energy of solids". In: *Nature* 325.

— (1987b). "Elasticity of Particle Assemblies as a Measure of the Surface Energy of Solids". In: *Proceedings of the Royal Society of London. A. Mathematical and Physical Sciences* 412.1843, pp. 269–283.

Kirkpatrick, S. (1971). "Classical Transport in Disordered Media: Scaling and Effective-Medium Theories". In: *Physical Review Letters* 27.25, pp. 1722–1725.

Landau, L. D. and Lifshitz, E. M. (1970). *Theory of Elasticity*. Pergamon Press.

Landauer, R. (1952). "The Electrical Resistance of Binary Metallic Mixtures". In: *Journal of Applied Physics* 23.7, pp. 779–784.

Lawn, B. R., Evans, A. G., and Marshall, D. B. (1980). "Elastic/Plastic Indentation Damage in Ceramics: The Median/Radial Crack System". In: *Journal of the American Ceramic Society* 63.9-10, pp. 574–581.

Lawn, B. (1993). *Fracture of Brittle Solids*. 2nd ed. Cambridge University Press.

Lazarus, V. (2017). "Fracture spacing in tensile brittle layers adhering to a rigid substrate". In: *EPL (Europhysics Letters)* 117, p. 24002.

Lazarus, V. and Pauchard, L. (2011). "From craquelures to spiral crack patterns: influence of layer thickness on the crack patterns induced by desiccation". In: *Soft Matter* 7.6, pp. 2552–2559.

Lesaine, A. et al. (2018). "Highly porous layers of silica nanospheres sintered by drying: scaling up of the elastic properties of the beads to the macroscopic mechanical properties". In: *Soft Matter* 14, p. 3987.

Li, H. and Bradt, R. C. (1992). "The indentation load/size effect and the measurement of the hardness of vitreous silica". In: *Journal of Non-Crystalline Solids* 146, pp. 197–212.

Loftman, K. A. and Thereault, J. R. (1957). "Aqueous dispersions of pyrogenic silica". Pat. US2984629A.

Luo, Y. R. (2007). *Comprehensive Handbook of Chemical Bond Energies*. CRC Press.

Mandel, J. (1972). "Plasticité classique et viscoplasticité". In: *Courses and lectures (International Centre for Mechanical Sciences)* 97.

Maurini, C. et al. (2013). "Crack patterns obtained by unidirectional drying of a colloidal suspension in a capillary tube: experiments and numerical simulations using a two-dimensional variational approach". In: *International Journal of Fracture* 184, pp. 75–91.

Moeendarbary, E. et al. (2013). "The cytoplasm of living cells behaves as a poroelastic material". In: *Nature Materials* 12.3, pp. 253–261.

Mori, T. and Tanaka, K. (1973). "Average stress in matrix and average elastic energy of materials with misfitting inclusions". In: *Acta Metallurgica* 21.5, pp. 571–574.

Moro, S. (2013). "Elaboration de matériaux poreux par agrégation et consolidation de suspensions de silices hydrophobées". PhD thesis. Université Pierre et Marie Curie (Paris, France).

Noirjean, C. et al. (2017). "Dynamics and ordering of weakly Brownian particles in directional drying". In: *Phyical Review Materials* 1 (6), p. 065601.

Oliver, W. C. and Pharr, G. M. (1992). "An improved technique for determining hardness and elastic modulus using load and displacement sensing indentation experiments". In: *Journal of Materials Research* 7.6, pp. 1564–1583.

Pauchard, L., Parisse, F., and Allain, C. (1999). "Influence of salt content on crack patterns formed through colloidal suspension desiccation". In: *Physical Review E* 59.3, pp. 3737–3740.

Pedersen, J. S. (1997). "Analysis of small-angle scattering data from colloids and polymer solutions: modeling and least-squares fitting". In: *Advances in Colloid and Interface Science* 70, pp. 171–210.

Peng, L. et al. (2009). "Investigation of the states of water and OH groups on the surface of silica". In: *Colloids and Surfaces A* 334, pp. 112–115.

Piroird, K. et al. (2016). "Role of evaporation rate on the particle organization and crack patterns obtained by drying a colloidal layer". In: *EPL (Europhysics Letters)* 113.3, p. 38002.

Ponte Castaneda, P. (2004). *Heterogeneous materials*. Ecole Polytechnique (Palaiseau, France).

Ponton, C. B. and Rawlings, R. D. (1989). "Vickers indentation fracture toughness test, part 1: Review of literature and formulation of standardised indentation toughness equations". In: *Materials Science and Technology* 5, pp. 865–872.

Rountree, C. L. and Bonamy, D. (2014). "Method for measuring the tenacity of a material". Pat. WO2014023729A1.

Routh, A. F. (2013). "Drying of thin colloidal films". In: *Reports on Progress in Physics* 76.4, p. 046603.

Routh, A. F. and Russel, W. B. (2001). "Deformation Mechanisms during Latex Film Formation: Experimental Evidence". In: *Industrial & Engineering Chemistry Research* 40.20, pp. 4302–4308.

Rouxel, T. (2007). "Elastic Properties and Short-to Medium-Range Order in Glasses". In: *Journal of the American Ceramic Society* 90.10, pp. 3019–3039.

Sarlat, T. et al. (2006). "Frozen capillary waves on glass surfaces: an AFM study". In: *The European Physical Journal B - Condensed Matter and Complex Systems* 54.1, pp. 121–126.

Scherer, G. W. (1989). "Drying gels: VIII. Revision and review". In: *Journal of Non-Crystalline Solids* 109 (2-3), pp. 171–182.

— (1990). "Theory of Drying". In: *Journal of the American Ceramic Society* 73 (1), pp. 3–14.

— (1992). "Crack-tip stress in gels". In: *Journal of Non-Crystalline Solids* 144, pp. 210–216.

Shahidzadeh-Bonn, N. et al. (2005). "Delayed Fracture in Porous Media". In: *Physical Review Letters* 95.17, p. 175501.

Sherwood, T. K. (1929). "The Drying of solids—II". In: *Industrial and Engineering Chemistry* 21.10, pp. 976–980.

Sibrant, A. L. R. and Pauchard, L. (2016). "Effect of the particle interactions on the structuration and mechanical strength of particulate materials". In: *EPL (Europhysics Letters)* 116.4, p. 49002.

Stöber, W., Fink, A., and Bohn, E. (1968). "Controlled growth of monodisperse silica spheres in the micron size range". In: *Journal of Colloid and Interface Science* 26.1, pp. 62–69.

Stoney, G. G. (1909). "The Tension of Metallic Films Deposited by Electrolysis". In: *Proceedings of the Royal Society of London. Series A, Containing Papers of a Mathematical and Physical Character* 82.553, pp. 172–175.

Thiery, J. et al. (2015). "Water transfer and crack regimes in nanocolloidal gels". In: *Physical Review E* 91 (4), p. 042407.

Thornton, C. (1993). "On the relationship between the modulus of particulate media and the surface energy of the constituent particles". In: *Journal of Physics D: Applied Physics* 26.10, p. 1587.

Toei, R. and Okazaki, M. (1970). "Drying mechanism of capillary-porous bodies". In: *Journal of Engineering Physics* 19 (3), pp. 1123–1131.

Vannoni, M., Sordini, A., and Molesini, G. (2011). "Relaxation time and viscosity of fused silica glass at room temperature". In: *The European Physical Journal E* 34.9, p. 92.

Verwey, E. J. W. and Overbeek, J. T. G. (1949). *Theory of the Stability of Lyophobic Colloids*. Elsevier.

Vigil, G. et al. (1994). "Interactions of Silica Surfaces". In: *Journal of Colloid and Interface Science* 165 (2), pp. 367–385.

Voigt, W. (1889). "Ueber die Beziehung zwischen den beiden Elasticitätsconstanten isotroper Körper". In: *Annalen der Physik* 274.12, pp. 573–587.

Wang, H. F. (2000). *Theory of Linear Poroelasticity with Applications to Geomechanics and Hydrogeology*. Princeton University Press.

White, L. R. (1982). "Capillary rise in powders". In: *Journal of Colloid and Interface Science* 90 (2), pp. 536–538.

Willis, J. R. (1987). "Randomly inhomogeneous media". In: *Homogenization Techniques for Composite Media*. Ed. by E. Sanchez-Palencia and A. Zaoui. Spring-Verlag, Berlin.

Xia, Z. C. and Hutchinson, J. W. (2000). "Crack patterns in thin films". In: *Journal of the Mechanics and Physics of Solids* 48, pp. 1107–1131.

Xu, P., Mujumdar, A. S., and Yu, B. (2009). "Drying-Induced Cracks in Thin Film Fabricated from Colloidal Dispersions". In: *Drying Technology* 27.5, pp. 636–652.

Yow, H. N. et al. (2010). "Effect of film thickness and particle size on cracking stresses in drying latex films". In: *Journal of Colloid and Interface Science* 352.2, pp. 542–548.

Zhuravlev, L. T. (1993). "Surface characterization of amorphous silica - a review of work from the former USSR". In: *Colloids and Surfaces A* 74.1, pp. 71–90.

— (2000). "The surface chemistry of amorphous silica. Zhuravlev model". In: *Colloids and Surfaces A* 173, pp. 1–38.

université PARIS-SACLAY
ÉCOLE DOCTORALE
Sciences mécaniques et énergétiques, matériaux et géosciences (SMEMAG)

Titre : Propriétés mécaniques et de structure de films formés par évaporation de suspensions colloïdales

Mots clés : colloïdes ; séchage ; fracture

Résumé : Le séchage d'une suspension colloïdale produit une couche solide plus ou moins poreuse. Ce processus intervient dans de nombreuses applications, telles que le procédé sol-gel ou la fabrication de laques et de peintures. Durant le séchage, l'évaporation du solvant entraîne la rétraction du matériau ; des contraintes importantes peuvent alors apparaître dans les couches colloïdales, les rendant susceptibles de se fracturer. Il est ainsi crucial de comprendre l'influence de paramètres de contrôle tels que la vitesse de séchage, l'épaisseur de la couche ou la taille de particule sur les propriétés mécaniques et de structure du matériau final. Dans cette thèse, nous avons utilisé des suspensions de Ludox (silice colloïdale) comme système modèle afin d'étudier l'effet de la vitesse de séchage sur les propriétés du matériau solide obtenu.
Dans une première partie, nous avons mis en œuvre des mesures de porosité, ainsi que de microscopie à force atomique et de diffraction de rayons X, afin de caractériser l'effet de la vitesse de séchage sur les propriétés de structure des couches sèches. Nous avons mis en évidence l'importance de la polydispersité des suspensions initiales, ainsi que des phénomènes d'agrégation de particules, sur la structure et la compacité du matériau obtenu.
Dans une deuxième partie, des mesures de constantes élastiques par propagation d'ultrasons nous ont permis de déterminer l'élasticité tensorielle (i.e. le module de compressibilité et celui de cisaillement) des couches colloïdales. Ces modules élastiques dépendent de la porosité du matériau ainsi que de la taille des particules de silice. Les données expérimentales ont été comparées aux prédictions de deux schémas d'homogénéisation (Mori-Tanaka et auto-cohérent), ainsi qu'au modèle de Kendall pour le module d'Young, qui prend en considération une énergie d'adhésion entre les particules.
Enfin, nous avons déterminé la résistance à la fracture des couches colloïdales à l'aide de tests d'indentation Vickers. Cette résistance à la fracture, mesurée à la fin du séchage, est mise en relation avec la vitesse d'évaporation, la porosité du matériau, ainsi que la densité de fractures observées pendant le processus d'évaporation du solvant.

Title : Structural and mechanical properties of dried colloidal silica layers

Keywords : colloids ; drying ; fracture

Abstract : Drying a colloidal suspension results in the formation of a more or less porous solid layer. This procedure is central to many applications such as sol-gel processes, the design of paints and lacquers... As the solvent evaporation induces shrinkage of the material, large stresses can develop in these layers, making them prone to fracture. A crucial challenge is thus to understand the role of the control parameters, such as drying rate, film thickness and particle size, on the structural and mechanical properties of the final layer. In this thesis work, Ludox (colloidal silica) was used as a model system to study the effect of the drying rate on the structural and mechanical properties of the resultant solid.
The effect of the drying rate on the structural properties of the dry layers was studied using porosity measurements as well as atomic force microscopy and small-angle X-ray scattering. We could evidence the importance of initial suspension dispersity and particle aggregation on the structure of the dry layers.
Using ultrasound measurements, we determined the tensorial elasticity (bulk and shear moduli) of the dry layers. The elastic moduli can be related to the material porosity and the particle size. Thus, the experimental data was used to test several homogeneization schemes (Mori-Tanaka and self-consistent) as well as Kendall's model for the Young's modulus, which considers the effect of adhesive forces between particles.
Finally, hardness and fracture toughness of the materials were inferred from Vickers indentation tests. The fracture properties of the layers in their dry, final state were related to their packing fraction, the evaporation rate, and the density of the cracks formed during the desiccation process.

Université Paris-Saclay
Espace Technologique / Immeuble Discovery
Route de l'Orme aux Merisiers RD 128 / 91190 Saint-Aubin, France